3-2006

Cycle Performance of a Pulse Detonation Engine with Supercritical Fuel Injection

Timothy M. Helfrich

CYCLE PERFORMANCE OF A PULSE DETONTATION ENGINE WITH SUPERCRITICAL FUEL INJECTION

THESIS

Timothy M. Helfrich, First Lieutenant, USAF

AFIT/GAE/ENY/06-M14

DEPARTMENT OF THE AIR FORCE
AIR UNIVERSITY

AIR FORCE INSTITUTE OF TECHNOLOGY

Wright-Patterson Air Force Base, Ohio

AFIT/GAE/ENY/06-M14

CYCLE PERFORMANCE OF A PULSE DETONTATION ENGINE WITH SUPERCRITICAL FUEL INJECTION

THESIS

Presented to the Faculty

Department of Aeronautics and Astronautics

Graduate School of Engineering and Management

Air Force Institute of Technology

Air University

Air Education and Training Command

In Partial Fulfillment of the Requirements for the

Degree of Master of Science in Aeronautical Engineering

Timothy M. Helfrich, B.S.

First Lieutenant, USAF

March 2006

AFIT/GAE/ENY/06-M14

CYCLE PERFORMANCE OF A PULSE DETONTATION ENGINE WITH SUPERCRITICAL FUEL INJECTION

Timothy M. Helfrich, BS
First Lieutenant, USAF

Approved:

/Signed/	9 Mar 06
Paul I. King (Chairman)	date
/Signed/	9 Mar 06
Ralph A. Anthenien (Member)	date
/Signed/	9 Mar 06
Milton P. Franke (Member)	date

Abstract

Pulse detonation engines (PDE) rely on rapid ignition and formation of detonation waves. Because hydrocarbon fuels are composed typically of long carbon chains that must be reduced in the combustion process, it would be beneficial to create such reduction prior to injection of fuel into the engine. This study focused on PDE operation enhancements using dual detonation tube, concentric-counter-flow heat exchangers to elevate the fuel temperature up to supercritical temperatures. Variation of several operating parameters included fuel type (JP-8, JP-7, JP-10, RP-1, JP-900, and S-8), ignition delay, frequency, internal spiral length, and purge fraction. To quantify the performance, four key parameters examined were ignition time, deflagration to detonation transition time, detonation distance, and the percent of ignitions resulting in a detonation. In general, for all fuels except JP-10, increasing the fuel injection temperature decreased deflagration to detonation transition time and detonation distance, increased the percent of ignitions resulting in detonations (detonation percentage), and had no impact on ignition time. JP-10 was difficult to detonate, resulting in extremely poor performance. A minimum spiral length of 0.915 m (36 in) and a minimum purge fraction of 0.3 were determined. An increase in cycle frequency resulted in a decrease in deflagration to detonation transition time, but had little effect on ignition time and detonation distance. Analysis of ignition delay showed that 4 msec is the best ignition delay at high fuel injection temperatures, based on total time to detonation and detonation percentage.

Acknowledgements

I would like to thank my thesis advisor, Dr. Paul King, for the opportunity to perform this exciting work, and for his continuous support and countless hours of guidance. Thank you to my committee members, Dr. Ralph Anthenien and Dr. Milton Franke, for helping me to refine my work.

It was my great honor to work with Dr. Fred Schauer, without whom I would not have been afforded this opportunity. I am extremely thankful of your ongoing support of my work. This work was heavily influenced by the guidance of Dr. John Hoke, who was always available to critique my work. I would be remiss if I did not thank two of the most instrumental people in the success of this work, Royce Bradley and Curtis Rice. The guidance of Dr. Timothy Edwards was invaluable in the completion of this research. I would like to extend a special word of thanks to Dave Baker and Dwight Fox, both of whom excel in workmanship and dedication. Thanks are also in order for the workers of the ISSI machine shop.

My research would have never been completed without the help of two individuals who stayed late and came in early just to be my wingman during testing. Those people are Capt. Wesley Knick and 1Lt. David Slack. A special thanks to my predecessor, Capt. Chris Miser, whose exceptional work paved the way for this research.

Most of all I would like to thank my wife whose understanding and love kept my motivation up during this entire process. I would also like to thank her for my amazing son.

Table of Contents

Page

Page

Page

List of Figures

Page

Page

Page

Page

Page

Page

List of Tables

Page

List of Symbols

Acronyms

AFB – Air Force Base
AFIT – Air Force Institute of Technology
AFRL – Air Force Research Laboratory
AFRL/PR – Air Force Research Laboratory, Propulsion Directorate
AFRL/PRTC – Air Force Research Laboratory, Propulsion Directorate, Turbine Engine Division, Combustion Science Branch
AFRL/PRTG - Air Force Research Laboratory, Propulsion Directorate, Turbine Engine Division, Fuel Science Branch
AIAA – American Institute of Aeronautics and Astronautics
API – American Petroleum Insititute
ASEE – American Society of Electrical Engineers
ASME – American Society of Mechanical Engineers
ASTM – American Society for Testing and Materials
C-J – Chapman-Jougeut
CRC – Coordinating Research Council
DDT – Deflagration to Detonation Transition
FF – Fill Fraction
FN – Flow Number
JP – Jet Propellant
LOX – Liquid Oxygen
MMPDS – Metallic Material Properties Development and Standardization
NASA – National Air and Space Administration
NIST – National Institute for Standards and Technology
NPT – National Pipe Thread
PDE – Pulse Detonation Engine
PF – Purge Fraction
PID – Proportional, Integral, Derivative
PR – Propulsion Directorate
RP – Rocket Propellant
RR – Reaction Rate
S – Synthetic
SAE – Society of Automotive Engineers
SI – International Standard of Units
SR – Surveillance and Reconnaissance
UAV – Unmanned Aerial Vehicle
USAF – United States Air Force
ZDN – Zeldovich-Von Neumann-Doering

Symbols – All units shown [ ] are SI and units shows in { } are English

A – Arrehenius Constant
A – Cross-sectional Area [cm^2] {in^2}
a – Speed of Sound [m/sec] {ft/sec}
CI – Confidence Interval
c_p – constant pressure specific heat [J/(kg*K)] {Btu/(lbm*˚F)}
E – Energy [J] {Btu}
E – Modulus of Elasticity [MPa] {ksi}
E_a – Global Activation Energy [J] {Btu}
F– Force, Load [N] {lbf}
freq – Frequency [Hz]
h – Enthalpy [J/kg] {Btu/lbm}
L – Length [m] {in}
M – Mach Number
MW – Molecular Weight
$\dot{m}$ – mass flow rate [kg/sec] {lbm/sec}
n – Number of Data Points
P – Pressure [Pa or atm] {psi}
q – Heat Transfer Rate [kW] {Btu/sec}
q – Heat of Reaction [J/kg] {Btu/lbm}
R – Specific Gas Constant [J/(kg*K)] {Btu/(lbm*˚F)}
R_u – Universal Gas Constant [J/(kg*K)] {Btu/(lbm*˚F)}
r – Radius [cm] [in]
SG – Specific Gravity
T – Temperature [K] {˚F}
t – Wall Thickness [cm] {in}
$t_{\alpha/2}$ – "T" Distribution
u – Velocity [m/sec] {ft/sec}
V – Volume [L] {gal}
$\dot{V}$ – Volumetric Flow Rate [L/min] [gal/min]
W – Running Load [N/m] {lbf/in}
$\overline{X}$ – Experimental Mean
X_i – Individual Data Point
– Number of

Greek Symbols – All units shown [ ] are SI and units shows in { } are English

α – Coefficient of Thermal Expansion [m/(m*K)] {in/(in*ºF)}
γ – Ratio of Specific Heats
λ – Cell Size [mm] {in}
μ – Viscosity [Pa*sec] {psi*sec}
μ' – Bulk Viscosity [Pa*sec] {psi*sec}
ρ – Density [kg/m^3] {lbm/ft^3}
σ – Standard Deviation
σ – Stress [atm] {psi}
Φ – Equivalence Ratio

Subscripts

1 – State One, Reactants
2 – State Two, Products
actual – Actual
air – Air
b – Boiling
bendshear – Shear due to Bending
cond – Conduction
c – Critical
DID – Direct Initiation Detonation
fuel – Fuel
hoop – Hoop (stress)
long – Longitudinal
long_total – Total Sum in Longitudinal Direction
mix – Mixture
st – Stoichiometric
therm – Due to Thermal Gradient
tube – Tube
weld - Weld

CYCLE PERFORMANCE OF A PULSE DETONTATION ENGINE

WITH SUPERCRITICAL FUEL INJECTION

I. Introduction

With the late 1980's came a massive surge in pulse detonation engine (PDE) research. The potential for higher thermal efficiencies, high thrust, low weight, low cost, scalability, and a large operational envelope has driven the recent PDE research (Schauer, 2001:1). The potential for higher thermal efficiency is based on the understanding that the constant volume process that occurs in a pulse detonation engine is more efficient than the constant pressure process that occurs in most modern gas turbine engines (Eidelman, 1991:1).

Due to the pulse detonation engine's attractive qualities it has received attention by many facets of the aeronautical engineering community; spawning interest in several applications for the PDE including aircraft, spacecraft, cruise missiles, and hybrid functions with a gas turbine engine. The aircraft application of the PDE is focused in the arena of unmanned aerial vehicles (UAVs), but has potential for supersonic manned flight as well. Both the National Air and Space Administration (NASA) and the Air Force Research Laboratory (AFRL) are conducting research into the possibility of using pulse detonation rocket engines (Kailasanath, 2003:1). A large amount of interest is focused on the cruise missile application. The use of PDEs is estimated to reduce the cost of a cruise missile propulsion system by an order of magnitude (Tucker, 2005:1-2). Hybrid applications for the PDE include; use as the afterburner of a turbojet, as an

additional thrust source in the bypass duct of a turbofan, and in combination with a scramjet. When used in combination with a scramjet, the pulse detonation engine is used to accelerate the vehicle to a hypersonic velocity at which point the scramjet takes over (Kailasanath, 2003:1).

Motivation

While the pulse detonation engine has the potential to provide significant advantages over current aircraft propulsion systems, it is still in the early stages of development. Several technological barriers need to be overcome before the PDE can be considered a practical means of providing propulsion to operational aircraft. A large hurdle is the efficient use of low vapor pressure hydrocarbon fuels, such as JP-8, JP-5, JP-7, JP-10, JP-900, RP-1, and S-8.

The vast majority of research into pulse detonation engines has been performed with gaseous fuels, such as hydrogen and simple hydrocarbons. The lack of liquid hydrocarbon fuel research has left a large gap between research and the operational use of pulses detonation engines. While gaseous fuels are readily available for research, nearly all United States Air Force (USAF) aircraft and air-breathing missiles utilize liquid fuels, primarily JP-8 and JP-10. Therefore, the ability to utilize liquid hydrocarbon fuels efficiently in the PDE is necessary to bring pulse detonation engine technology out of the research phase and into operation.

Four key cycle parameters are adversely affected by using liquid hydrocarbon fuels in lieu of gaseous fuels. The parameters are the time it takes to create a deflagration wave within the fuel/air mixture (ignition time), the time it takes to transition the

deflagration wave into a detonation wave (DDT time), the length of detonation tube required for the mixture to transition to a detonation (detonation distance), and the consistency of the detonations (percent of ignitions that transition to detonations). Both the ignition time and the DDT time are nearly an order of magnitude larger for complex liquid hydrocarbon fuels than simpler gaseous fuels. For example, ignition time for a hydrogen/air mixture is on the order of one millisecond, where as the ignition time of a JP-8/air mixture is near seven milliseconds.

Based on global reaction theory, the reaction rate of a fuel-air mixture will increase with increasing mixture temperature and head pressure. The ignition time is inversely related to the reaction rate; hence, as the mixture temperature or head pressure increases the ignition time will decrease. However, for the small percentage that the fuel/air mixture temperature is increased, there is no noticeable ignition time decrease expected. Based on research with lighter hydrocarbons, DDT times in low vapor pressure fuels are expected to decrease with increasing fuel injection temperature and head pressure. With a decrease in DDT time comes a decrease in the detonation distance.

Problem Statement

The cycle performance of a liquid hydrocarbon fueled PDE with fuel injection temperatures above the flash vaporization point is unknown. Previous research has demonstrated that flash vaporization of liquid hydrocarbon fuels significantly improved the PDE performance, but no research has been conducted to determine the effect of operating with fuel injection temperatures beyond the point of flash vaporization. The focus of this research is to use a dual concentric counter-flow heat exchanger system to

determine the effect of fuel injection temperature on the ignition time, deflagration to detonation transition (DDT) time, detonation distance, and percent of ignitions resulting in detonation with varying operating parameters. The operating parameters examined include; fuel type (JP-8, JP-7, JP-10, JP-900, RP-1, and S-8), ignition delay, frequency, internal spiral length, and purge fraction. This work is a stepping-stone to the heating of low vapor pressure fuels to endothermic temperatures for use in a PDE; therefore, a significant amount of research was completed in preparation for endothermic testing. Endothermic fuels research is summarized in Appendix D.

Research Goals

The primary goal of this research is to determine the effect of fuel injection temperature on the ignition time, DDT time, detonation distance, and percent of ignitions resulting in detonations. A major focus of this work was to study the viability of six distinct low vapor pressure hydrocarbon fuels (JP-8, JP-7, JP-10, RP-1, JP-900, and S-8) for use in a pulse detonation engine with supercritical fuel injection. The effects of ignition delay, purge fraction, cycle frequency, and spiral length were also examined during this research. A portion of this research is dedicated to the development of a heat exchanger system used to heat the fuel to endothermic temperatures, for subsequent testing. The following is a list of the intermediate goals met in order to achieve the primary goals:

1. Design and construct a dual PDE tube mounted heat exchanger system
2. Complete safety approval process for using a liquid hydrocarbon cooled heat exchanger

3. Design and implement a constant fuel mass flow rate delivery system
4. Determine the effect of increasing fuel injection temperature (up to 755.4 K) on ignition time, DDT time, detonation distance, and percent of ignitions resulting in detonations for JP-8, JP-7, JP-10, RP-1, JP-900, and S-8
5. Determine the effect of increasing JP-8 injection temperature (up to 755 K) on ignition time, DDT time, detonation distance, and percent of ignitions resulting in detonations for varying ignition delay, purge fraction, cycle frequency, and spiral length
6. Research and develop an endothermic fuel heating system for use in later testing

Chapter Summary

Pulse detonation engines have a significant amount of potential over current propulsion systems. The next step in the advancement of pulse detonation engines is the transition from simple gaseous fuels to complex liquid hydrocarbons, specifically JP-8. A system has been developed to heat liquid hydrocarbon fuels to flash vaporization and supercritical temperatures using the waste heat from the PDE detonation tubes. The focus of this effort is to determine the effect that increasing the fuel injection temperature to supercritical levels has on the performance of the PDE with varying operating parameters.

Units

Unfortunately, the pulse detonation engine engineering community maintains little continuity concerning the choice of a single unit system. Many authors use the international standard of units (S.I.), while others use the English system as a standard. To satisfy the two groups, both systems are used wherever it is possible. When it is not possible, only the S.I. is presented.

Organization

Chapter I served as a brief introduction to pulse detonation engine technology. In addition, the motivation, problem statement, and the goals for this work are discussed. Chapter II provides the theoretical background for this research starting with a discussion on deflagration and detonation waves, pulse detonation engine theory, and the global reaction theory. Previous research, a brief overview of the fuels tested, and other pertinent details are presented. In Chapter III, the facility, pulse detonation engine, instrumentation, test configurations, and methodology are discussed. Chapter IV is a summary of the data reduction and error analysis techniques used during this research. Chapter V provides the results and analysis of experimental data. Chapter VI discusses the conclusions from the previous chapters and provides recommendations for further research.

II. Background

Deflagration and Detonation Waves

Two distinct types of flame fronts occur within a pulse detonation engine, deflagration and detonation. A deflagration wave is a subsonic flame front that propagates by heat transfer. A detonation wave is a supersonic flame front that consists of a shock wave coupled with a trailing reaction zone. The principle differences between a deflagration and detonation wave are the wavespeeds and pressure difference across the wave. Table 1 shows typical physical properties for deflagration and detonation waves, where subscripts one and two denote the conditions within zones one and two in Figure 1.

Table 1. Typical detonation and deflagration property ratios across waves (Kuo, 2005:357)

	Detonation	Deflagration
u_1/a_1	5 - 10	0.0001 - 0.03
u_2/u_1	0.4 - 0.7	4 - 6
P_2/P_1	13 - 55	~ 0.98
T_2/T_1	8 - 21	4 - 16
ρ_2/ρ_1	1.7 - 2.6	0.06 - 0.25

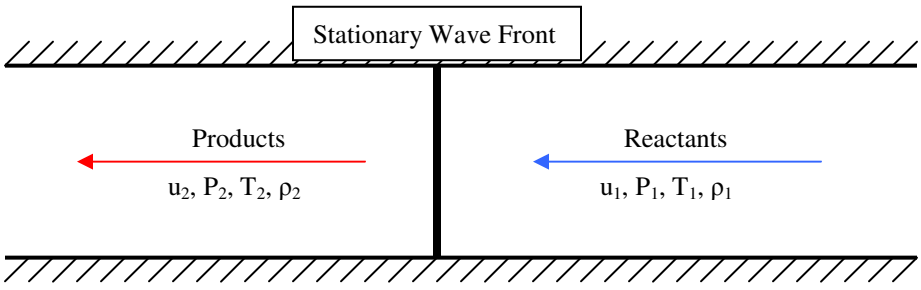

Figure 1. Generic diagram of stationary combustion wave with velocity relative to the wave

A detonation wave is complex in nature and formation. One prime example of the formation of a detonation wave is that of a tube that is closed at one end, opened at the other, and filled with a stoichiometric fuel-air mixture. If the mixture is ignited at the closed end of the tube, a deflagration wave will propagate through the flammable mixture. As shown in Table 1, the products behind the deflagration wave are higher in temperature and specific volume than the unburned mixture. The increase in specific volume creates a compression wave that travels at the speed of sound toward the deflagration wave front, causing the wave to accelerate. As the flame continues, more compression waves are formed due to the increased specific volume. The compression waves cause further static temperature increases that consequently increase the speed of sound, based on Equation (1):

$$a = \sqrt{\gamma RT} = \sqrt{\frac{\gamma P}{\rho}} \tag{1}$$

where a is the *speed of sound*, γ is the *ratio of specific heats*, R is the *specific gas constant*, P is the *static pressure*, ρ is the *static density*, and T is the *static temperature*. As the compression waves accelerate, due to the increase in the speed of sound, they begin to coalesce at the deflagration wave front, causing further acceleration of the wave. If the tube is sufficiently long, a shock wave will form due to the coalescence of the multiple compression waves. The newly formed shock wave is sufficiently strong enough to ignite the mixture ahead of the flame front. The continuing reaction behind the shock wave forms more compression waves that sustain the shock wave and prevent it

from decaying. The flame front that consists of a shock wave and following reaction is considered a detonation wave.

Combustion Wave Theory

A review of combustion wave theory is necessary to understand the physical principles that govern detonation and deflagration flames. To begin let us revisit Figure 1, where a one-dimensional flame front is traveling from left to right through a channel. All velocities in Figure 1 are relative to the flame front; therefore, the flame front is shown as stationary. The conservation of mass, momentum, and energy equations for one-dimensional flow with no body forces, no external heat addition, and negligible species inter-diffusion effects are shown in Equations (2), (3), and (4), respectively (Kuo, 2005:357):

$$\frac{d(\rho u)}{dx} = 0 \tag{2}$$

$$\rho u \frac{du}{dx} = -\frac{dP}{dx} + \frac{d}{dx}\left[\left(\frac{4}{3}\mu + \mu'\right)\frac{du}{dx}\right] \tag{3}$$

$$\rho u\left[\frac{d}{dx}\left(h + \frac{u^2}{2}\right)\right] = -\frac{d}{dx}q_{cond} + \frac{d}{dx}\left[u\left(\frac{4}{3}\mu + \mu'\right)\frac{du}{dx}\right] \tag{4}$$

where ρ is the *density*, u is the *velocity*, P is the *pressure*, μ is the *viscosity*, μ' is the *bulk viscosity*, h is the *enthalpy*, and q_{cond} is the *conducted heat transfer rate*. By assuming that $\mu >> \mu'$ and $\frac{dT}{dx} = \frac{du}{dx} = 0$ for the completely burned and unburned gases, the conservation equations are reduced to:

$$\rho_1 u_1 = \rho_2 u_2 \tag{5}$$

$$P_1 + \rho_1 u_1^2 = P_2 + \rho_2 u_2^2 \tag{6}$$

$$h_1 + \frac{u_1^2}{2} + q = h_2 + \frac{u_2^2}{2} \tag{7}$$

where $h = c_p T$ and q is the *heat of reaction* (Kuo, 2005:358). If the specific gas constant is assumed constant then the perfect gas law becomes:

$$P = \rho R T \tag{8}$$

for both unburned and burned gases. By combining Equations (1), (6), and (8) the Rayleigh-line relation is determined (Kuo, 2005:359), shown in Equation (9):

$$\gamma M_1^2 = \frac{P_2 / P_1 - 1}{1 - \rho_1 / \rho_2} \tag{9}$$

where M is the *Mach number*. The Mach number is defined as $M = u/a$. By combining Equations 6 and 7 the Rankine-Hugoniot relation can be found (Kuo, 2005:360), shown in Equation (10):

$$\frac{\gamma}{\gamma - 1}\left(\frac{P_2}{\rho_2} - \frac{P_1}{\rho_1}\right) - \frac{1}{2}(P_2 - P_1)\left(\frac{1}{\rho_1} + \frac{1}{\rho_2}\right) = q \tag{10}$$

where q is the *heat of reaction*. A Hugoniot curve is a plot of pressure (P) versus the inverse of density ($1/\rho$); and it is used to plot all possible values of P_2 and $1/\rho_2$ for given

values of P_1, $1/\rho_1$, and q. To create a Hugoniot curve, values for P_1, $1/\rho_1$, and q are assumed and P_2 is solved over a range of $1/\rho_2$'s. Figure 2 is a representative Hugoniot curve plotted with Rayleigh lines.

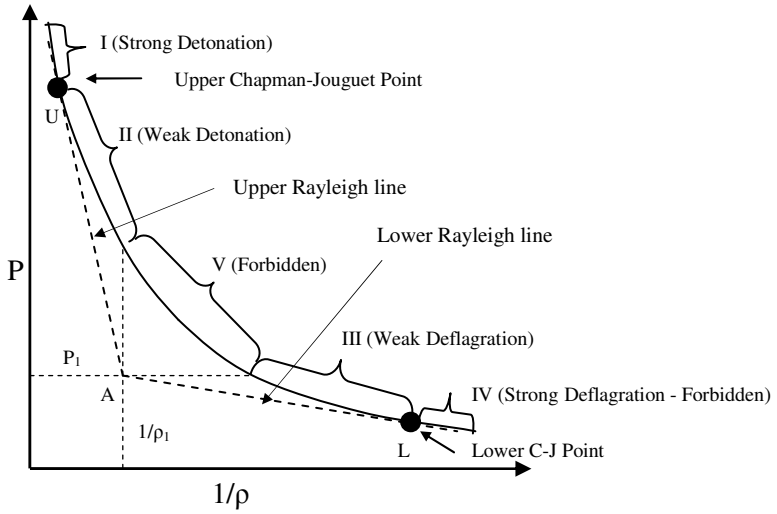

Figure 2. Representative Hugoniot curve with Rayleigh lines on P versus 1/ρ plane

The Hugoniot curve is divided into five regions with two critical points. The two points are the upper and lower Chapman-Jouguet (C-J) points, and are located at the tangent of the Hugoniot curve and the upper and lower Rayleigh lines, respectively. Of the five regions, only three regions are physically possible, regions I, II, and III. Region I is bounded by only the upper C-J point; and represents strong detonations. A strong detonation is a transient state that will always decay back to the upper C-J point. Region II represents weak detonations; within it, the pressure of the products is less than that of the pressure at the upper C-J point. Weak detonations can only occur when extremely fast chemical kinetics are present; this is not the case in liquid hydrocarbons and

consequently is not relevant to this research. Region III represents weak deflagrations, and is bounded by the pressure of the reactants and the lower C-J point. Region III is significant to this research only because detonations begin as deflagrations at ignition. (Kuo, 2005:361-365)

Within a liquid hydrocarbon fueled PDE, stable detonations occur only at the upper Chapman-Jouguet point. The gaseous wavespeed of the upper C-J point is the primary metric used in pulse detonation engine research to confirm the existence of a detonation wave. As will be demonstrated in Chapter IV, the upper C-J wavespeed is used to determine DDT time, detonation distance, and the percentage of ignitions resulting in detonations during this effort. The upper C-J wavespeed for liquid hydrocarbon/air mixtures with equivalence ratios near one is between 1,700 and 2,000 m/s (5,577.4 and 6,561.7 ft/s) (Glassman, 1996:247). Based on previous research, an upper C-J wavespeed of 1,800 m/s was assumed for all fuels during this research.

The Zel'dovich-Von Neumann-Döring Model

The previous section detailed a one-dimensional analysis of the physics governing all combustion waves. The focus now turns to detonation waves. Zeld'ovich, Von Neumann, and Döring simultaneously developed a model of a one dimensional detonation wave, now named the Zel'dovich-Von Neumann-Döring Model (ZDN). The ZDN model makes four key assumptions (Fickett, 1979:42):

- The flow is one-dimensional
- The shock is a jump discontinuity
- The reaction rate (defined later) is zero ahead of the shock and finite behind; also the reaction is irreversible

- All thermodynamic variables other than the chemical composition are in local thermodynamic equilibrium everywhere

The premise of the ZND model is that a detonation wave is comprised of three distinct elements; a thin shock layer followed by a much thicker induction zone that is followed by a thick reaction zone. The shock alone is unable to promote chemical reactions, due to its infinitesimal thickness. The thickness of the shock layer is approximately several mean free paths. A schematic of temperature, pressure and density variation through the three zones is shown in Figure 3.

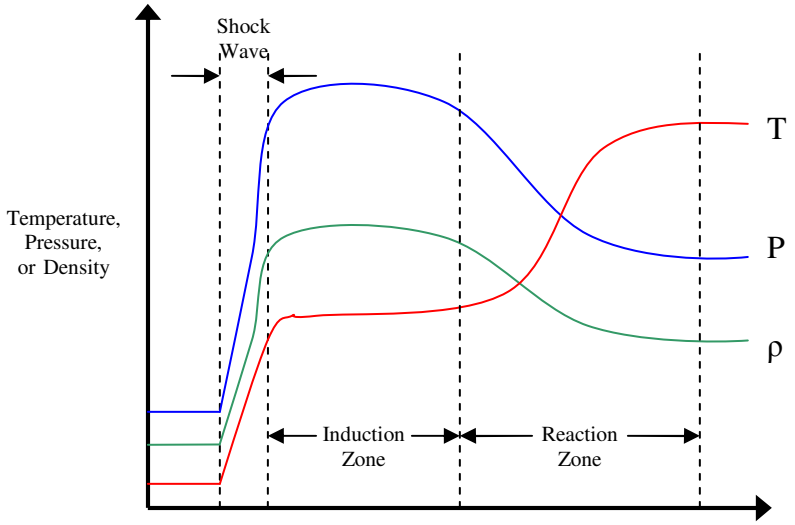

Figure 3. Generic diagram of thermodynamic property variation across a ZND detonation model

The thin shock wave induces severe spikes in temperature, pressure, and density. The increase in temperature is such that the fuel/air mixture can react at a rate high enough for the trailing deflagration wave to travel at the same rate as the shock. The peak pressure reached directly behind the shock is referred to as the von Neumann spike. The magnitude of the increases in temperature, pressure, and density are dependent on

the fraction of gaseous mixture reacted. Within the induction zone, the reaction rate slowly begins to increase, while the thermodynamic properties remain constant. The reaction zone is located directly after the induction zone, and is denoted by a sharp increase in reaction rate. The reaction zone continues until the thermodynamic properties reach equilibrium. The entire distance including shock, induction zone, and reaction zone, is on the order of 1 cm (0.39 in) thick. (Kuo, 2005:381-382)

Detonation Cell Size and Initiation Energy

A one-dimensional detonation wave is described well using the ZND model, but an actual detonation wave is multidimensional in behavior. Within long narrow channels, detonation waves are governed by primarily two-dimensional phenomena. Three-dimensional effects are generally important when the width of the channel is much greater than the natural transverse-wave spacing (Fickett, 1979:298). Based on the dimensions of the detonation tubes used during this research, two-dimensional effects dominate the detonation wave behavior; therefore, only two-dimensional effects will be discussed.

A fully developed detonation wave traversing through a reactive mixture produces repeating structures, known as cells. This cell structure is bounded by the path traversed by the triple point. The triple point is the location where the Mach stem, incident shock, and reflected shock intersect. The cell structure has been captured experimentally using a smoke foil. The smoke foil uses soot along the path of the detonation wave to capture the shape of the cell structure. At the triple point, a slip line is formed. The slip line divides the material that passes through the Mach stem from the material that passes through the

incident and reflected shocks. The division of materials causes a discontinuity coupled with high vorticity that creates a pattern in the soot. The result is a fish-scale like pattern, shown in Figure 4 and Figure 5. Figure 4 is a representative drawing of the two-dimensional detonation cell structure with a representative triple point. Figure 5 is a CFD model for of the two-dimensional cell structure of a H_2/air mixture

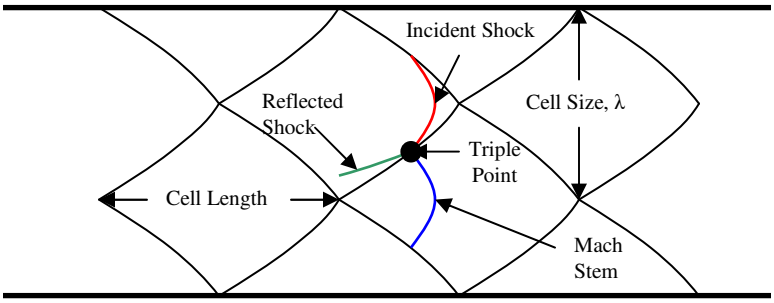

Figure 4. Drawing of representative two-dimensional detonation cell structure

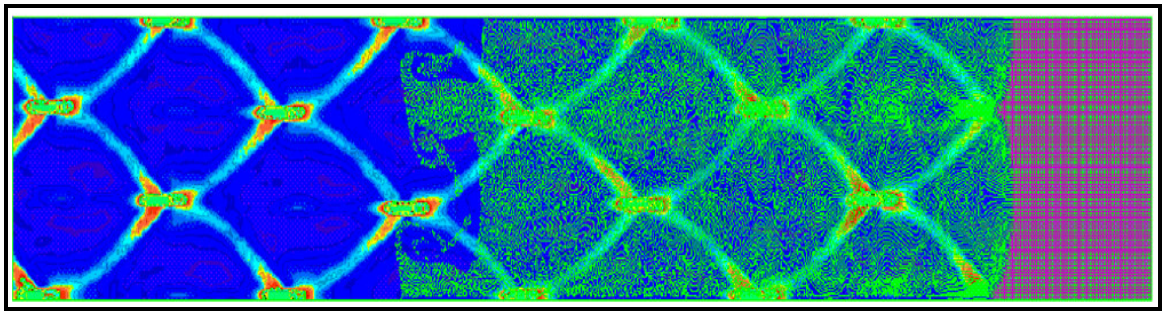

Figure 5. CFD smoke foil for two-dimensional H_2/air mixture detonation cell structure (Katta, 1999)

An important feature depicted in Figure 4, is the cell size, λ. The cell size is defined as the height of the cell structure and is related to the direct detonation initiation energy. The direct detonation initiation energy is the experimentally determined energy required by a combustion system to initiate a detonation directly. Previous experimental

research has shown that a typical stoichiometric low vapor pressure liquid hydrocarbon/air mixture requires 1 MJ (948 Btu) of energy to directly initiate detonation (Tucker, 2005:25). Figure 6 is a plot of cell size versus direct initiation detonation energy for several stoichiometric fuel/oxydizer mixtures. From a best-fit curve through the data, a simple relationship between the cell size and direct initiation detonation energy is:

$$E_{DID} = 3.375\lambda^3 \tag{11}$$

where E_{DID} is the *direct initiation detonation energy* in Joules and λ is the *cell size* in millimeters. The important item to notice is the detonation energy varies with the cube of the cell size.

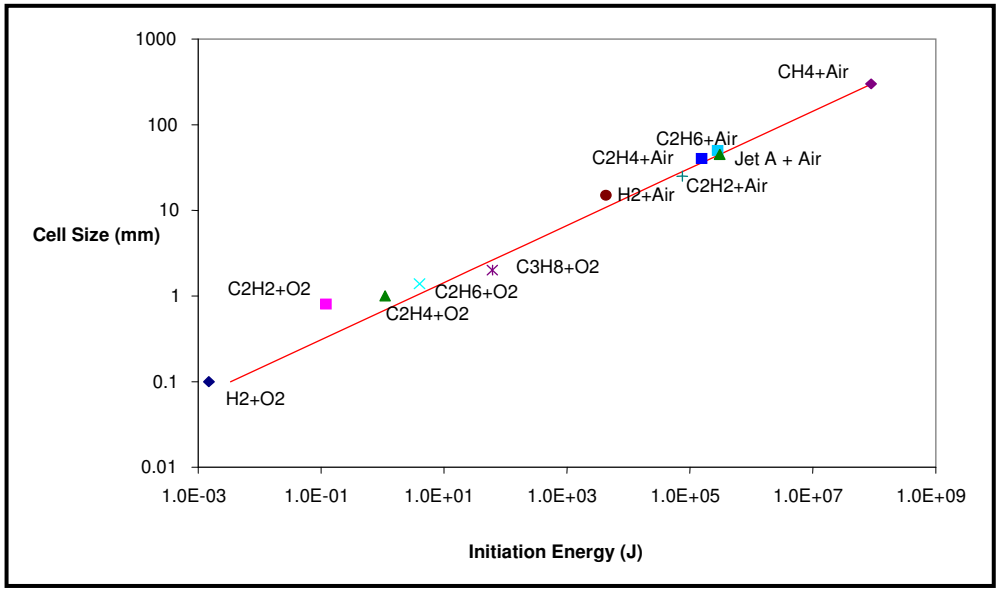

Figure 6. Experimentally determined relationships between cell size (mm) and direct initiation energy (J) for various stoichiometric fuel/air mixtures (Tucker, 2005:25)

Pulse Detonation Engine Cycle

To understand this research, a basic understanding of the PDE cycle is required. The PDE cycle used for this effort consists of three sequential phases; fill, fire, and purge. For this research, each phase was allotted an equal length of time. Crucial tasks are performed during each of the three phases.

During the fill phase, shown in Figure 7, fill valves release a fuel/air mixture into the PDE detonation tubes. The volume of fuel/air mixture discharged into the detonation tube is based on the fill fraction. The fill fraction (FF) is the ratio of fuel/air mixture volume at ambient conditions to the tube volume. For this effort, a fill fraction of one was used exclusively. The closing of the fill valves ends the fill phase.

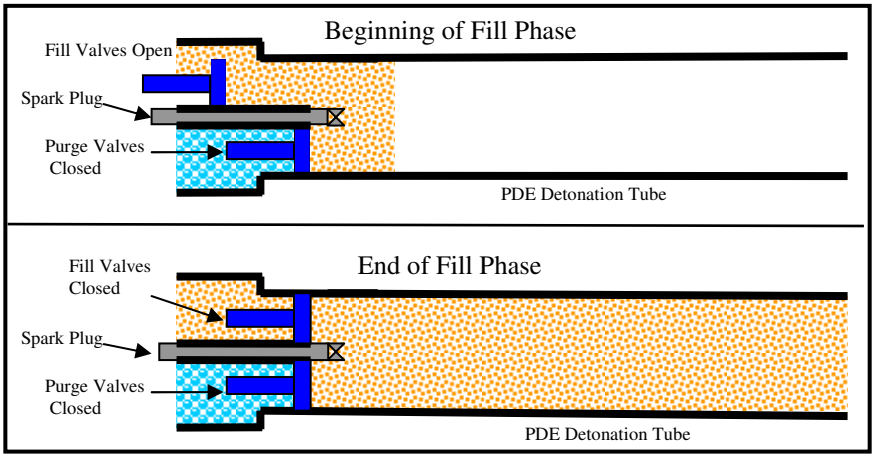

Figure 7. Typical pulse detonation engine fill phase

The fire phase, shown in Figure 8**,** is the most complex phase in the PDE cycle. At the onset of the fire phase, a spark is deposited by the spark plug. The release of the spark energy causes a deflagration wave to form at the closed end of the tube. The

deflagration wave transitions to a detonation wave within the length of the detonation tube via the process discussed earlier in the chapter. The process of transitioning from deflagration to detonation is known as deflagration to detonation transition (DDT). The distance between the closed end of the tube and the location where detonation begins is defined as the detonation distance.

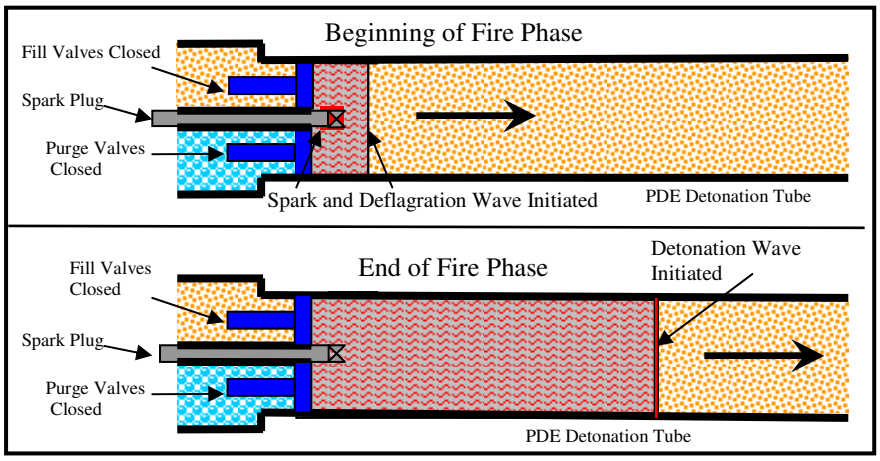

Figure 8. Typical pulse detonation engine fire phase

It is necessary to examine the fire phase in more detail. The fire phase can be divided into smaller segments, shown in Figure 9. These smaller segments are defined by crucial events. The first event is the closure of the fill valves, which also marks the beginning of the fire phase. The next event is the release of spark energy. The delay between the closure of the fill valves and the release of the spark energy is defined as the ignition delay. The third event is the formation of a deflagration wave, which is known as ignition. The time that is required for the ignition of the spark to form a deflagration wave is known as the ignition time. The fourth event is the formation of the detonation wave. The time elapsed between the formation of the deflagration wave and the

detonation wave is known as the deflagration to detonation transition time. The fifth and final event is the exit of the detonation wave from the detonation tube. The blowdown time is defined as the time between the detonation wave formation and the exit of the wave from the tube. The thrust of the PDE is produced during the blowdown.

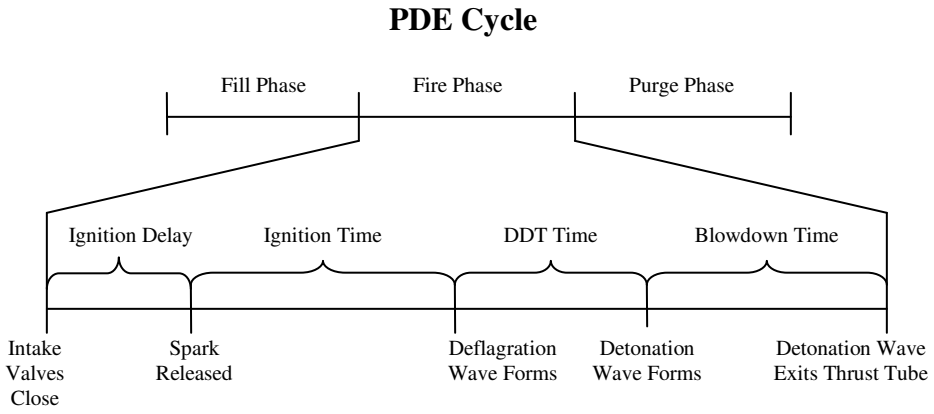

Figure 9. Typical pulse detonation engine fire cycle divided into critical segments

The third and final phase of the PDE cycle is the purge phase, shown in Figure 10. The purge phase begins with the opening of the purge valves. Whereupon, purge air enters the detonation tubes. The volume of purge air released into the detonation tubes is determined by the purge fraction (PF), the ratio of the purge air volume at ambient conditions to the tube volume. Except where noted, a purge fraction of 0.5 was used during this effort. The closing of the purge valves marks the end of the purge phase, and the PDE cycle.

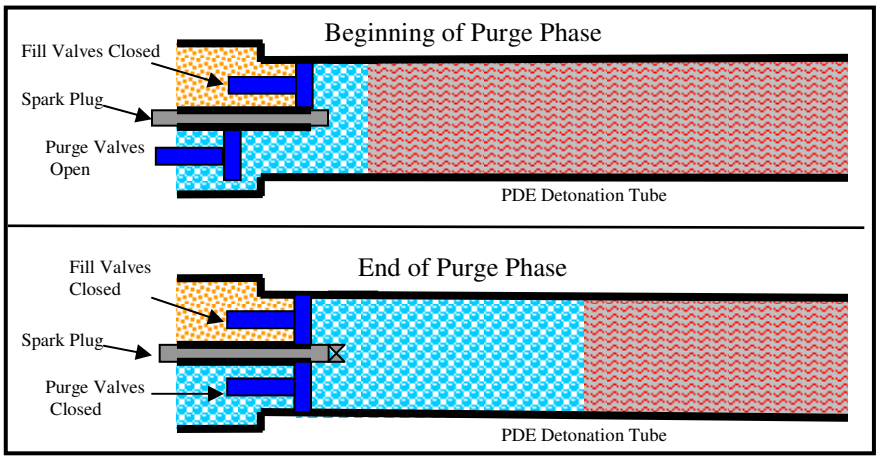

Figure 10. Typical pulse detonation engine purge phase

The PDE cycle occurs at a specified frequency, given in hertz. As the frequency of a pulse detonation engine is increased, the time allotted for each phase is decreased. For example, each phase is allotted 22.22 msec for a frequency of 15 Hz, but only 16.67 msec for a frequency of 20 Hz. When the frequency is too high, the objectives of the phase are not met, and poor performance will ensue. There is very little concern about the completion of either the fill or purge phases, based on the frequencies typically used for research. The problems arise when the fuel/air mixture does not ignite, transition to a detonation, and exit the tube within the allotted time. An example of the time limitation is as follows: Based on previous research, the blowdown time is estimated at 2 msec and the total time to detonation is approximately 10 msec for JP-8/air mixtures, thus the ignition delay can be no higher than 4.67 msec when running at 20 Hz. This restriction led to the selection of the 4 msec ignition delay that was used for all tests run at a frequency of 20 Hz.

JP-8 SUPERTRAPP Data

The thermodynamic properties of JP-8 were needed to perform vital calculations for this research. Unfortunately, there is no set of empirical thermodynamic properties of JP-8 available above 393 K (247.7 ˚F). Properties for temperatures below 393 K (247.7 ˚F) can be found in the CRC Handbook of Aviation Fuel Properties (CRC, 2004). Since empirical data is unavailable at higher temperatures, several computational methods of predicting thermodynamic properties have been developed, and one example is SUPERTRAPP. SUPERTRAPP was developed by the National Institute of Standards and Technology (NIST), and is an interactive computer database used for the prediction of thermodynamic and transport properties of fluid mixtures (NIST, 2003).

JP-8 is not a pure substance, but is a mixture of several complex hydrocarbons. JP-8 is defined by MIL-T-83133 which dictates fuel performance and thermodynamic properties, but not chemical makeup. Since the exact chemical makeup of JP-8 is not controlled, modeling all JP-8 thermodynamic properties is very difficult. In order to model the particular properties of JP-8 using SUPERTRAPP, a JP-8 surrogate was developed to match specific thermodynamic properties. A surrogate is a combination of pure substances used to mimic impure substances (Edwards, 2001). The surrogate used for this research was provided by the Air Force Research Laboratory Propulsion Directorate (AFRL/PR). Table 2 is a complete list of the pure substances, along with mole fractions, used in the AFRL JP-8 surrogate. There are published surrogates for JP-7 and RP-1, but not for S-8 or JP-900. JP-10 is a single component fuel, thus no surrogate is necessary.

Table 2. AFRL SUPERTRAPP JP-8 surrogate composition

Component	Mole Fraction	Component	Mole Fraction
methylcyclohexane	0.065	nampthalene	0.058
meta-xylene	0.07	n-dodecane	0.175
ethylcyclohexane	0.067	1-methylnapthalene	0.052
n-decane	0.157	n-tetradecane	0.113
butylbenzene	0.056	n-hexadecane	0.066
isobutylbenzene	0.056	2,5-dimethylhexane	0.065

Using the AFRL JP-8 surrogate, SUPERTRAPP can estimate the density, specific heat, viscosity, and thermal conductivity of JP-8. SUPERTRAPP is limited to temperatures between 273 and 998 K (32 and 1337.7 ˚F) and pressures between 1 and 85 atm (14.7 and 1249.16 psi). Figure 11 is a plot of the output data for JP-8 density for various pressures as a function of temperature, using the AFRL JP-8 surrogate. A large reduction in density is noted as temperature is increased. Figure 11 is a representative sample of the thermodynamic properties estimated by SUPERTRAPP.

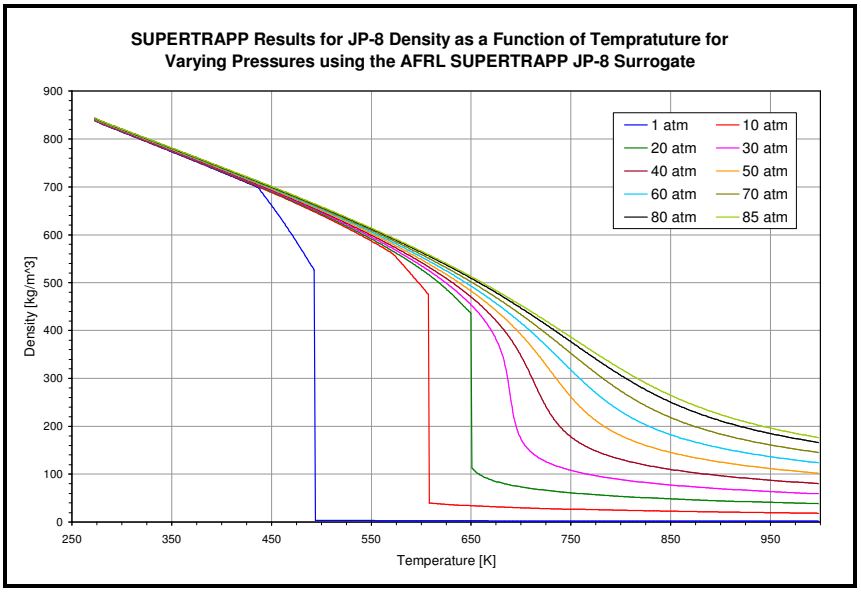

Figure 11. SUPERTRAPP results for JP-8 density as a function of temperature for varying pressure using the AFRL SUPERTRAPP JP-8 surrogate

It should be noted that SUPERTRAPP does not take in to account the effects of endothermic reactions occurring in the fuel, therefore thermodynamic property data is only reliable up to 810.7 K (1000 ˚F).

Fuel States

During the course of this research, fuel was heated from ambient to an excess of 755.4K (900 ºF). As the temperature of low vapor pressure fuel increases, the fuel transitions through three phases: liquid, gas, and supercritical. At high temperatures, the fuel will under go endothermic reactions. The temperature range where endothermic reactions occur will be referred to as the endothermic region. With the current experimental setup, the fuel begins in the liquid state.

In a pulse detonation engine, an efficient method of transitioning the liquid fuel to the gas state is through flash vaporization. Previous research has shown that flash vaporization of JP-8 will occur with a fuel injection temperature above 530 K (494 ˚F) and pressure above the saturated liquid line (Tucker, 2005: 94). The fuel flash vaporization temperature varies with fuel. For flash vaporization to occur, two initial conditions need to be satisfied: (1) fuel enthalpy at or above the flash vaporization temperature and (2) fuel pressure above the saturated liquid line. This initial condition is shown as state 1 on the temperature vs. pressure plot in Figure 12. Flash vaporization can then be induced by forcing an adiabatic pressure drop in the fuel. If the pressure drop is sufficient, the fuel will transition from liquid through the vapor dome and into the gas phase. The gaseous state of the fuel is shown as state 2 in Figure 12.

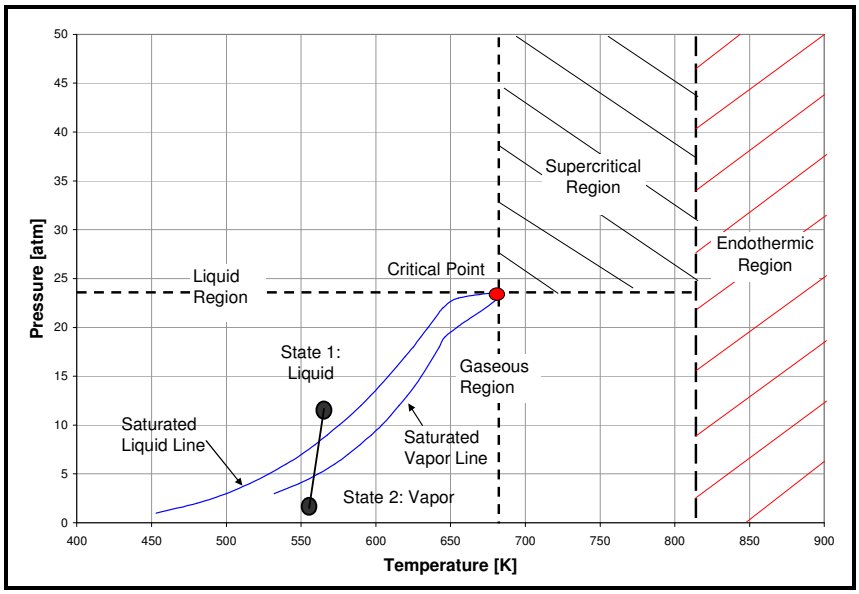

Figure 12. Representative pressure vs. temperature diagram for a typical low vapor pressure fuel

Flash vaporization is beneficial for use in the PDE because it eliminates the presence of liquid fuel droplets within the fuel/air mixture. If the liquid fuel droplets exist, they must be evaporated and then be heated to the auto ignition temperature. The current PDE setup does not allow enough time for the liquid fuel droplets to evaporate completely; therefore, a portion of the fuel trapped in liquid droplet form cannot be burned. If the fuel/air mixture has a stoichiometric global equivalence ratio, the existence of liquid fuel droplets causes a locally fuel lean mixture. Therefore, vaporization of the fuel droplets significantly improves the performance of the PDE.

The fuel becomes supercritical once it exceeds both the critical pressure and the critical temperature. The intersection of the critical pressure line and the critical temperature line is denoted as the critical point (see Figure 12). Within the supercritical region, the density of the fuel significantly decreases as the fuel temperature increases. This phenomenon is discussed in more detail in subsequent sections. The critical

pressures and temperatures for the fuels used in this research are shown in Table 3. There are no published critical properties for either S-8 or JP-900, but it was still necessary to determine these values. A method, covered in Appendix C, was used to predict the critical properties based on correlations.

Table 3. Summary of the critical temperature and pressure for the six fuels used in this research (Edwards, 2002:1095)

Fuel	Critical Temperature [K]	Critical Pressure [atm]	Critical Temperature [ºF]	Critical Pressure [psi]
JP-8	683.15	23.14	770	340
JP-7	672.04	20.75	750	305
JP-10	697.59	36.88	796	542
RP-1	683.15	21.43	770	315
S-8	682.00	26.70	768	392
JP-900	670.00	25.60	746	376

Finally, the endothermic region is where the long hydrocarbon chains that make up the fuel begin to break apart (crack) and form smaller, lighter hydrocarbon chains or hydrogen atoms. Fuel undergoing endothermic reactions absorbs surrounding heat to break apart the chemical bonds. In most liquid hydrocarbon fuels the first endothermic reactions are seen at temperatures near 755.4 K (900 °F), but the bulk of the effects are seen at temperatures around 810.9 K (1000 °F). The fuel pressure has not been shown to affect the degree of endothermic reactions that occur in a low vapor pressure fuel. The amount of cracking that the fuel undergoes is not only a function of the temperature, but also the time in which the fuel remains at the specified temperature, known as the residence time.

Effects of Temperature and Pressure on Ignition Time

The effect of varying pressure and temperature of the fuel/air mixture on ignition time in a PDE was examined experimentally during this effort. Before experimentation was performed, it was necessary to predict this effect. The ignition time is directly related to the time it takes for the necessary chemical reactions to proceed to completion, known as the chemical reaction time. Using global reaction theory, the chemical reaction time (hence the ignition time) can be related to the thermodynamic properties of the fuel/air mixture (Lefebvre, 1986). The properties of interest are mixture temperature and head pressure. Global reaction theory assumes that the reaction of a fuel/air mixture can be modeled as a single global reaction. Low vapor pressure fuel/air mixture combustion is not governed by a single global reaction; however, global reaction theory can be used to predict ignition trends. The ignition time is inversely related to the reaction rate, where the reaction rate is determined by the Arrehenius expression (Equation (12)).

$$IgnitionTime \propto \frac{1}{RR} = \frac{1}{A} P^{-n} [fuel]^{-m} [oxydizer]^{-j} e^{\left(\frac{E_a}{R_u T_{mix}}\right)} \tag{12}$$

where *RR* is the *reaction rate*, *A* is the *Arrehenius constant*, *P* is the *head pressure*, *[fuel]* is the *fuel concentration*, *[oxidizer]* is the *oxidizer concentration*, R_u is the *universal gas constant*, E_a is the *global activation energy*, and T_{mix} is the *mixture temperature*. To predict the effect of temperature and pressure on ignition time, the constant values of *n*, *m*, and E_a are needed. Values of *n*, *m*, and E_a were found experimentally for Jet-A (Lefebvre, 1986). Jet-A is a jet fuel defined by fuel properties that are similar to JP-8. Since the

global reaction theory is only used for trend prediction, the values for Jet-A will be used. The values of n, m, and E_a were determined to be 0.98, 0.37, and 29.6 kcal/kg-mol, respectively (Lefebvre, 1986:89). The exact value of j has not been determined, but is of no consequence to this research, since the concentration of oxidizer was not varied during this research. Figure 13 is a plot of the expected effect of increasing mixture temperature on normalized ignition time. The ignition time has been normalized by the ignition time for a mixture temperature of 394 K (250 ˚F), since that is the initial mixture temperature. Using a normalized ignition time causes all variables in Equation (12), other the one of interest, to drop out of the calculation.

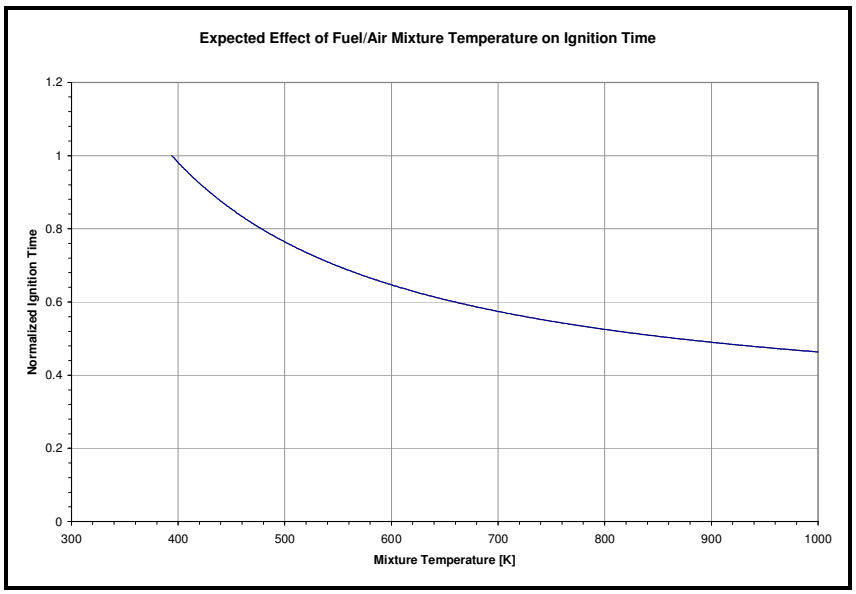

Figure 13. Expected effect of fuel/air mixture temperature on ignition time based on global reaction theory

The ignition time is expected to drop by over 50% as the mixture temperature is increased from 394 to 1000 K (300 to 1340 ˚F). As will be shown later, the mixture temperature only increases from 394 to 415 K (250 to 287 ˚F), as the fuel injection

temperature increases form 422 to 755 K (300 to 900 ˚F). This small mixture temperature increase is only expected to decrease the ignition time by 6.6%. As expected, no significant change in ignition time was seen as fuel injection temperature increases.

The effect of head pressure on ignition time is shown in Figure 14. The ignition time is normalized by the ignition time for a head pressure of 1 atm (14.7 psi). Figure 14 demonstrates that for head pressures ranging from 0.5 to 1.5 atm (7.35 to 22.1 psi), the ignition delay decreases by a factor of four. Therefore, a substantial decrease in ignition delay is expected as head pressure is increased. As shown in Chapter V, the ignition time varied with pressure as predicted in Figure 14.

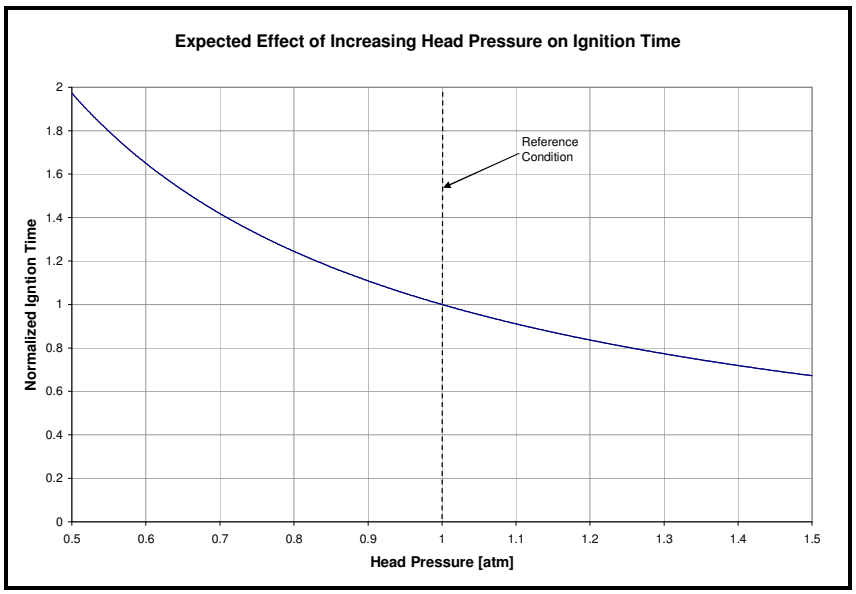

Figure 14. Expected effect of head pressure on ignition time based on global reaction theory

Ignition Delay and Initial Pressure

The pressure in the PDE head pressure fluctuates due to the presence of compression and expansion waves in the detonation tube. These waves are created as the

fill and purge air is forced into the detonation tubes. By selection of a spark delay, it is possible to deposit the spark during a compression wave, when the head pressure is above ambient. Figure 15 is the pressure time history during the PDE fire phase without combustion at 15 Hz with a mixture temperature of 394 K (250 ˚F). Ignition delays of 2, 4, 6, 8, and 10 msec are denoted as vertical lines in Figure 15.

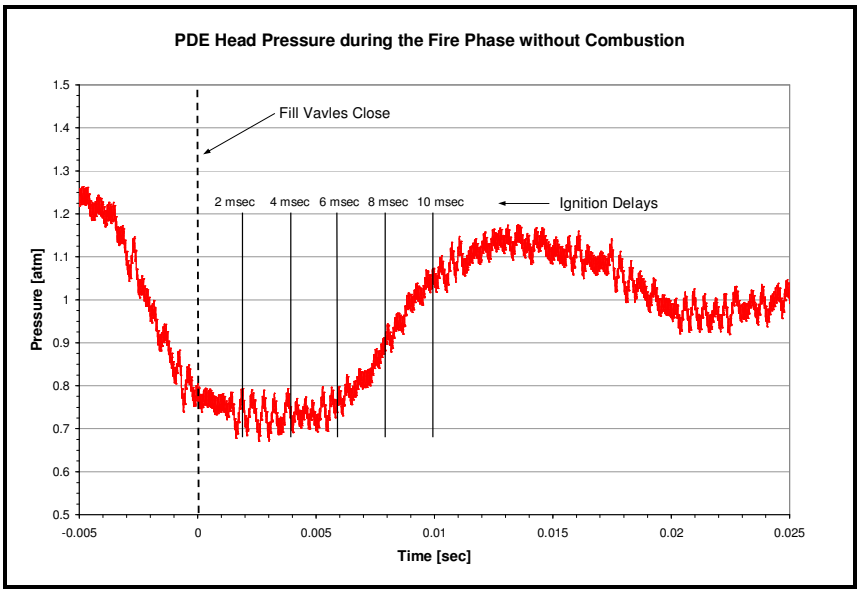

Figure 15. PDE head pressure during fire phase without combustion (vertical lines denote various spark delays)

Figure 15 demonstrates the benefit of selecting a high ignition delay. Selection of a 6, 8, or 10 msec ignition delay allows combustion to occur during a compression wave, while a 0 msec ignition delay forces combustion to occur during an expansion wave. The ignition time is not only affected by the pressure when the spark is deposit. The entire pressure history during the formation of a deflagration wave directly affects the ignition time. The time it takes for a deflagration wave to form following the spark (ignition time) is approximately 7 msec for JP-8. Therefore, the average pressure over the 7 msec

following the deposit of the spark was determined for all ignition delays from Figure 15, and is shown in Table 4

Table 4. Initial head pressure and average head pressure occurring over the 7 msec following the spark deposit

Ignition Delay [msec]	Initial Pressure [atm]	Average Pressure [atm]
2	0.712	0.819
4	0.728	0.907
6	0.765	1.005
8	0.932	1.079
10	1.042	1.105

Table 4 can be used to determine the potential effect of ignition delay for a fuel injection temperature of 394 K (250 ˚F). The difference between the average pressure of the 2 msec and 10 msec ignition delay cases is 0.286 atm (4.2 psi), or 25.9%. This difference is substantial, meaning that a large difference in ignition time is expected between the 2 msec and the 10 msec cases. A difference in ignition time is also expected between the 4 msec and the 10 msec cases, but it will be less than the difference between the 2 msec and the 10 msec cases. The 6, 8, and 10 msec ignition delays should produce similar ignition times, because the maximum difference between their average head pressures is 0.100 atm (1.47 psi), or 9%.

Effects of Temperature and Pressure on Detonability

The effect of varying pressure and temperature of the fuel/air mixture upon DDT time and detonation distance in a PDE was examined experimentally during this effort. Before experimentation was performed, it was necessary to predict this effect. Very little research has been performed to determine the relationship between initial mixture

properties (temperature and pressure) and the detonability of a low vapor pressure fuel/air mixture. Literature is available for lighter hydrocarbon/air mixtures, but little is focused on determining the effect of initial mixture temperature on cell size. The cell size of three different light hydrocarbons as a function of initial mixture temperature is shown in Figure 16. All data in Figure 16 is from the *Detonation Database*. (Kaneshige, 1997)

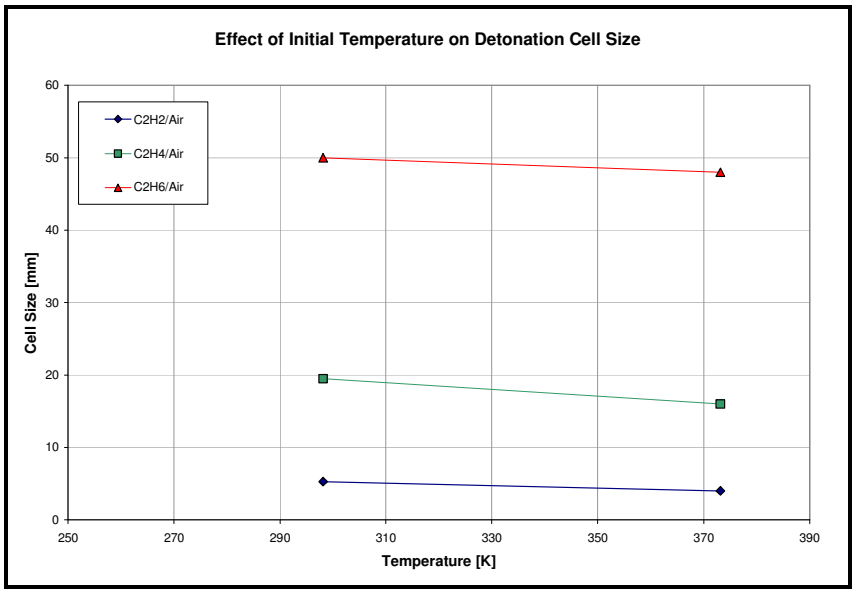

Figure 16. Effect of initial temperature on detonation cell size (data from Kaneshige ,1997)

The trend of these hydrocarbons is for the cell size to decrease slightly with increased mixture temperature. The three hydrocarbons examined in Figure 16 are all very light compared to low vapor pressure liquid hydrocarbons, with only two carbon atoms apiece. While the trends of smaller hydrocarbons do not dictate the trends of much heavier hydrocarbon, they do suggest that increasing initial mixture temperature will decrease the cell size. The decrease in cell size is an indication of an increase in performance. According to Equation (11), the direct initiation detonation energy

decreases by the cube of the cell size. As the direct initiation detonation energy decreases, the detonability of the mixture will increase. The increased detonability is expected to decrease DDT time and detonation distance. The percent of ignitions resulting in detonations is expected to increase with increasing fuel injection temperature.

The effect of initial pressure is well documented for lighter hydrocarbons, but little research has been performed with heavier hydrocarbons. The *Detonation Database* contains data that demonstrates the effect of initial pressure on cell size (Kaneshige, 1997). Figure 17 is a plot of initial pressure versus cell size for three light hydrocarbon/oxydizer mixtures and one H_2/O_2 mixture. All data in Figure 17 is from the *Detonation Database* (Kaneshige, 1997).

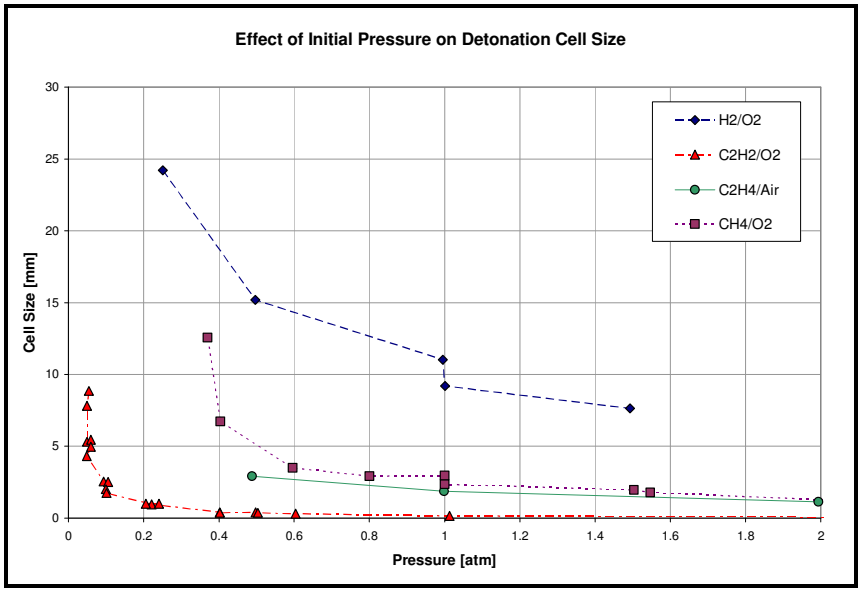

Figure 17. Effect of initial pressure on detonation cell size (Data from Kaneshiga, 1997)

Reduction in cell size is possible by increasing the initial pressure in light hydrocarbons. The exact trend shown in Figure 17 is not expected to occur in much

heavier hydrocarbons, but a general decrease in cell size with increasing initial pressure is expected. As stated earlier, smaller cell sizes indicate a decrease in direct initiation detonation energy. It is expected that increases in both initial head pressure and initial mixture temperature will result in decreased DDT time and detonation distance, as well as increased percentage of ignitions resulting in detonations.

Fuel Mass Flow Rate in Supercritical Regime

During previous research, it was found that the fuel density in a constant pressure system declined as temperature increased near the supercritical regime. Figure 18 is a plot of the fuel injection temperature and resultant fuel mass flow rate of a PDE operating with a JP-8/air mixture without a fuel mass flow regulation system (Miser, 2006:4-5). A 60% decrease in fuel mass flow rate is noted as the fuel temperature is increased to 755 K (900 ˚F).

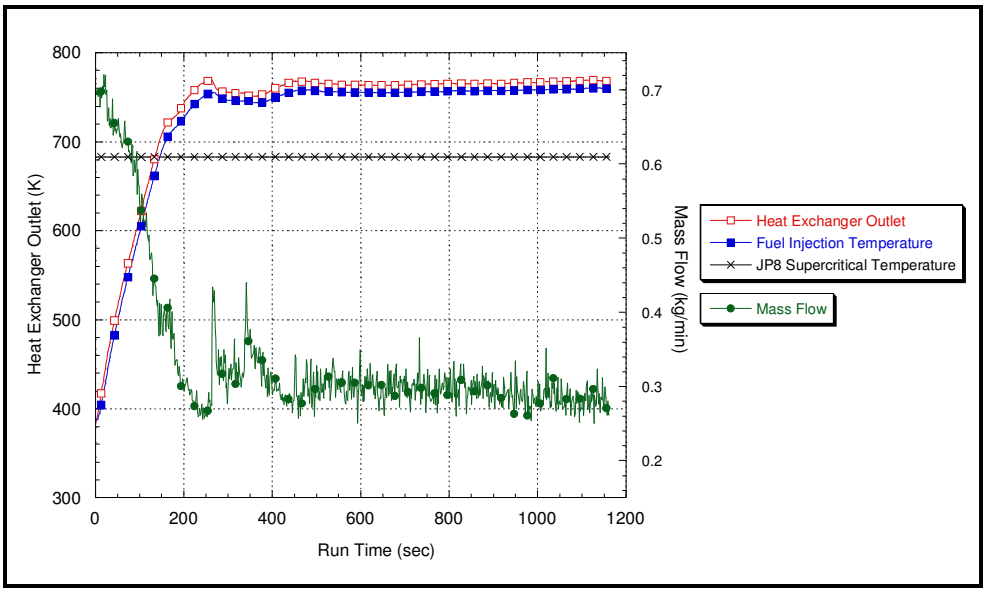

Figure 18. Effect of increasing fuel injection temperature on fuel mass flow rate without a fuel mass flow regulation system (Miser, 2006:4-5).

Based on SUPERTRAPP data, the decline in density as temperature increased was expected, as shown in Figure 11. Equation (13) demonstrates how a decline in density will cause a decline in fuel mass flow rate, for a given pressure drop and flow number:

$$\dot{m}_{fuel} = FN\sqrt{\Delta P}\sqrt{\rho/\rho_{ref}} \tag{13}$$

where $\dot{m}_{fuel}$ is the *fuel mass flow rate*, *FN* is the *flow number* (set by the selection of injection nozzles), ΔP is the *pressure drop* across the injection nozzles, and ρ is the *fuel density* at the inlet to the nozzle (Bartok, 1991). Equation (13) was derived from the Bernouli equation; therefore, it is only valid for incompressible flow. The existing system used for heated fuel experimentation lacked the flexibility to compensate for the density decrease, therefore a new fuel mass flow rate regulation system was developed. The details of the new fuel mass flow rate regulation system are discussed in Chapter III.

Fuel Descriptions

There were six fuels analyzed during this effort: JP-8, JP-7, JP-10, JP-900, RP-1, and S-8. Before detonating the six fuels, it was necessary to understand the differences between them. Table 5 is a list of the most important properties of the fuel, with respect to this research. Each fuel was designed for a specific purpose; therefore, each has advantages and disadvantages for use in a pulse detonation engine. The fuel descriptions given here are basic. A more in-depth discussion of these fuels can be found in the referenced papers and journal articles.

Table 5. Important fuel properties (Edwards, 2002)

Fuel	Approximate Formula	Net Heating Value [kJ/kg]	Specific Gravity @ 289 K	Viscosity @ 294 K [cst]
JP-8	C11H21	43,140	0.81	1.45
JP-7	C12H25	43,895	0.79	1.84
JP-10	C10H16	42,174	0.96	3.00
JP-900	C11H19.8	42,546	0.88	2.18
RP-1	C12H23	43,370	0.81	2.02
S-8	C11H23.7	44,016	0.78	1.59

JP-8

The baseline fuel used in this research was JP-8, or Jet Propellant 8. JP-8 has been the standard aviation fuel used by the United States Air Force since conversion from JP-4 in the 1980's. JP-8 replaced JP-4 to increase aircraft safety. JP-8 is governed by military specification, MIL-T-83133, which specifies fuel properties that must be met. There is no specification that governs the chemical makeup of JP-8; hence, there are an infinitely large number of chemical combinations possible. JP-8 performs unfavorably at elevated temperatures. When JP-8 is heated, the trapped oxygen molecules within the mixture begin to react with fuel, causing carbon deposits to form. The formation of carbon deposits is referred to as coking. (Edwards, 2001:1092)

JP-7

JP-7, or Jet Propellant 7, is a specialty fuel that was originally designed for use in the SR-71 aircraft. JP-7 is a low volatility/ high thermal stability aviation fuel. The SR-71 routinely flew at Mach 3, which dictated the need for a fuel with higher thermal stability. JP-7 is also highly refined, meaning that it contains low levels of sulfur and

aromatics. The drawback of JP-7 is the high cost; it is nearly three times the cost of JP-8. (Edwards, 2001:1092)

JP-10

JP-10, or Jet Propellant 10, was developed in the 1970's for use in turbine-powered cruise missiles. It is still the only air-breathing missile fuel used by the United States Air Force. JP-10 is different from all of the other fuels examined, because it is composed of only one component, *exo*-tetrahydrodicyclopentadiene. It is a high-density fuel with a low freezing point. Both of these qualities make JP-10 a perfect fuel for use in cruise missiles. Cruise missiles are stored for long times, and quite often in frigid environments. (Edwards, 2002:1095)

JP-900

JP-900 is a coal-based hydrocarbon fuel developed at The Pennsylvania State University. JP-900 is in the last stages of development, but the final version has not been completed. The focus of the JP-900 fuel program is to develop a coal-based fuel that is thermally stable to 755.4 K (900 ˚F). JP-900 is another highly refined fuel, resulting in extremely low quantities of sulfurs, olefins, and paraffins. (Schobert, 2002:192)

RP-1

RP-1, or Rocket Propellant 1, was developed in the 1950's during the Rocketdyne Rocket Engine Advancement Program. RP-1 is defined by military specification MIL-P-25576. RP-1 is highly refined to remove coke-forming components, such as sulfurs,

olefins, and aromatics. A mixture of RP-1 and liquid oxygen (LOX) was the propellant utilized in the first stage booster of the Saturn V, used during the first manned moon landing mission in 1969. (Edwards, 2002:1100)

S-8

S-8 is a synthetic fuel produced from natural gas using the Fischer Tropsch process. The batch of S-8 used for this research was produced by Syntroleum. S-8 is composed of 99.7% paraffins with only trace amounts of any other components. It has the lowest specific gravity and highest hydrogen-to-carbon ratio of those fuels studied.

Fuel Flow Meter Calibration

The fuel feed system used for this research incorporated a turbine mass flow meter to measure the fuel flow rate. The flow meter uses calibration curves to translate a rotational frequency into a volumetric flow rate. The volumetric flow rate is then converted to a mass flow rate using Equation (14):

$$\dot{m} = \rho \dot{V} \tag{14}$$

where $\dot{m}$ is the *fuel mass flow rate*, $\dot{V}$ is the fuel *volumetric flow rate*, and ρ is the *fuel density*. The turbine flow meter requires a calibration for each fuel used. The calibration for JP-8 and JP-10 were completed prior to this research, but calibration curves were needed for the other fuels used in this effort. It was correctly theorized that the JP-8 calibration might be suitable for JP-7, JP-900, RP-1, and S-8. The primary thermodynamic property affecting the flow meter calibration is the fuel viscosity. As

shown in Table 5, the viscosity of JP-900 is the highest of the four fuels mentioned earlier, and therefore has the largest difference in magnitude as compared to JP-8. A calibration test of JP-900 was performed to determine if new calibration curves for the JP-7, JP-900, RP-1, and S-8 were needed.

The calibration test was performed by flowing JP-900 through the flow meter at various flow rates. The actual flow rate was determined by measuring the volume of JP-900 that filled a graduated cylinder in two minutes. During the test, the flow meter frequency was recorded on the control computer. The average flow meter frequencies measured during the test and the corresponding volumetric flow rates are shown in Figure 19.

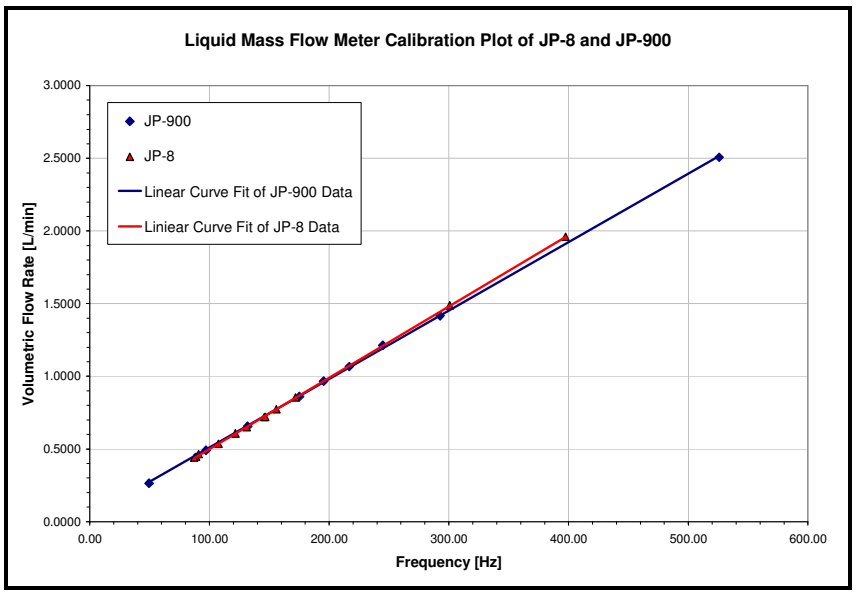

Figure 19. Fuel mass flow meter calibration test results

The lines are curve fits to the data points shown on the plot. The curve fits are used in the *LabVIEW* program to convert frequency to flow rate. The JP-8 and JP-900

curve fits are nearly identical, especially in the range of flow rates used during testing, 0.4 to 0.8 L/min (0.106 to 0.212 gal/min). Therefore, the JP-8 calibration was used for all fuels in this effort, except JP-10.

III. Test Facilities and Methodology

Pulse Detonation Research Facility

This research was conducted at the Pulse Detonation Research Facility located in Building 71A, D Bay, Wright-Patterson Air Force Base, Ohio (D-Bay). The Pulse Detonation Research Facility is managed by the Air Force Research Laboratory Propulsion Directorate, Turbine Engine Division, Combustion Sciences Branch (AFRL/PRTC). A contractor manages normal operation and testing.

The PDE test facility located in D-Bay was originally designed for testing turbojet engines, but has since been retrofitted to support pulse detonation engine research. The major areas of D-Bay used for PDE research are the test cell, control room, and liquid fuel room. The 21,200 m^3 (748,670 ft^3) explosion proof test cell includes a static thrust stand capable of measuring thrust upwards of 267,000 N (60,024 lbf) (not used for this research) (Schauer, 2001). The static thrust stand acts as a base for a smaller damped thrust stand upon which the PDE research engine is mounted. An exhaust tunnel is situated directly down stream of the PDE research engine, and is used to vent out exhaust products during operation.

The control room and test cell are located alongside each other, but are separated by a 0.61 m (2 ft) thick concrete wall. All testing is regulated from the control room by the use of a control panel and *LabVIEW* control software that is run on a dedicated computer. The *LabVIEW* program provides real-time monitoring of all control parameters in addition to a multitude of air and fuel properties. Data was captured by two different *LabVIEW* programs running on separate computers. Low-speed data was

captured on the same computer that controls the facility, while high-speed data is gathered on a dedicated computer. The test cell was monitored during testing by the use of closed circuit cameras placed within the test cell that feed into monitors in the control room.

The liquid fuel room is located adjacent to both the test cell and the control room, and is separated from both by 0.61 m (2 ft) thick concrete walls. The liquid fuel room contains the facility's low point ventilation system, liquid storage equipment, and fuel conditioning equipment. Liquid fuels are pressure fed from the liquid fuel room to the test cell during testing. Another closed circuit camera that feeds into the control room is located in the fuel room, for observation during liquid fuel testing.

Air Supply System

Two Ingersoll-Rand Pac air compressors (Model # PA 300V) provide the compressed air for both the purge and fill cycles of the PDE. Each compressor provides up to 40 m^3/min (1,412.6 ft^3/min) and is rated to 6.8 atm (100 psi). Under normal operation, one compressor is sufficient to supply the necessary airflow to the PDE. The air is pumped from the compressor into a 4.5 m^3 (159 ft^3) receiver tank (Serial # 10894, Buckeye Fabrication Co.). Both the air compressors and the receiver tank are stored in a separate room within D-Bay, referred to as the compressor room. Photographs of a compressor and the receiver tank are shown in Figure 20.

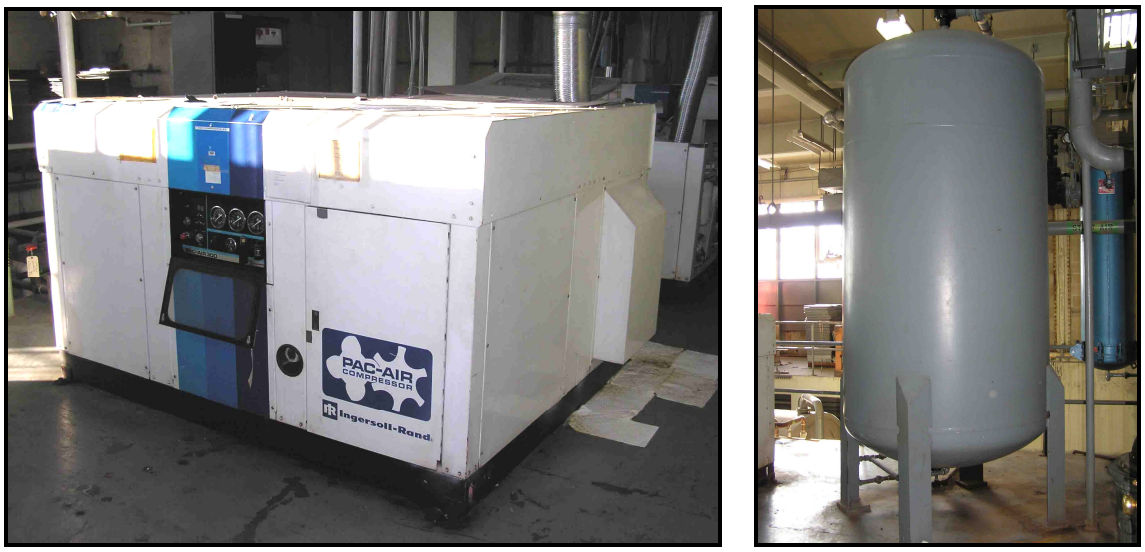

Figure 20. Photographs of the air compressors (left) as well as the receiver tank (right), located in the compressor room

Air is routed from the compressor room into the test cell, where it is fed into the PDE. Once the air enters the test cell it runs under the static test stand. The air flow then separates into air for the fill and purge lines, shown in Figure 21. Dome loader type pressure regulators control the air mass flow rate for both the fill and purge lines. Tescom Electropneumatic PID Controllers (Model # ER 1200) that actuate pressure regulators, shown in Figure 21. A pressure transducer downstream of the pressure regulator monitors the pressure. The air mass flow regulation process is discussed further in the next section. Calibrated orifice plates are situated downstream of the pressure regulator to choke the flow, shown in Figure 21. The orifice plates come in a variety of orifice diameters and can be removed and replaced easily to facilitate a large range of airflow rates. For this effort, a 12.7 mm (0.5 in) orifice plate was used in the fill supply line and an 8.99 mm (0.354 in) orifice plate was used in the purge supply line. Surge

tanks are located down stream of the orifice plates to preclude any disruption of the flow at the orifice plate from compression waves that are generated in the engine intake system.

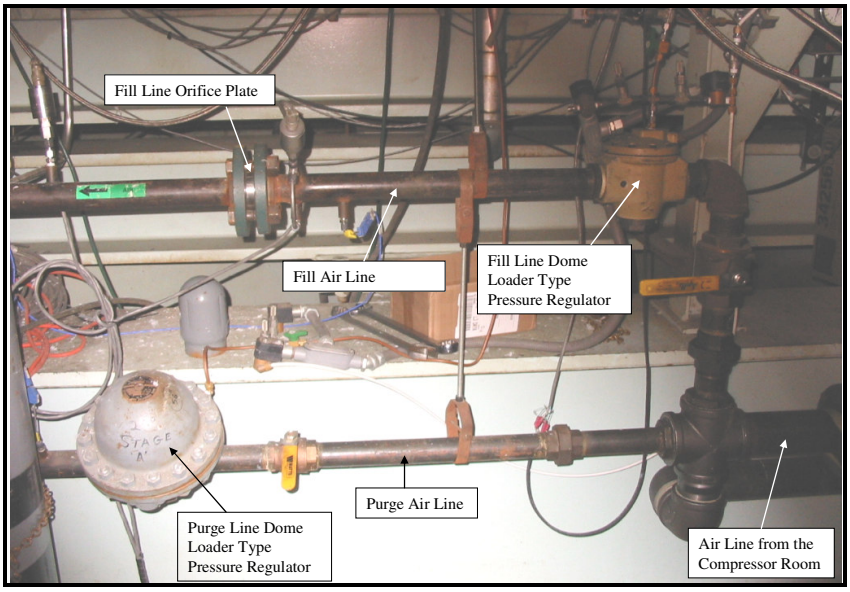

Figure 21. Photograph of the air flow system under the static test stand

The fill air enters the test stand where it is immediately routed through a Chromalox Circulation Heater (P/N 053-500870-187). The *LabVIEW* program in the control room regulates the air temperature exiting the heater. An amperage is set in the *LabVIEW* program that is translated to an upper temperature limit and sent to the Chromalox temperature controller (Model # 2104) on the control panel. After leaving the heater, the fill air flows into the fill manifold. Within the fill air manifold, the fuel is added to create the fuel/air mixture that is fed into the head of the engine. The purge air runs through the purge manifold from the surge tank to the engine head. A schematic diagram of the entire airflow system is shown in Figure 22.

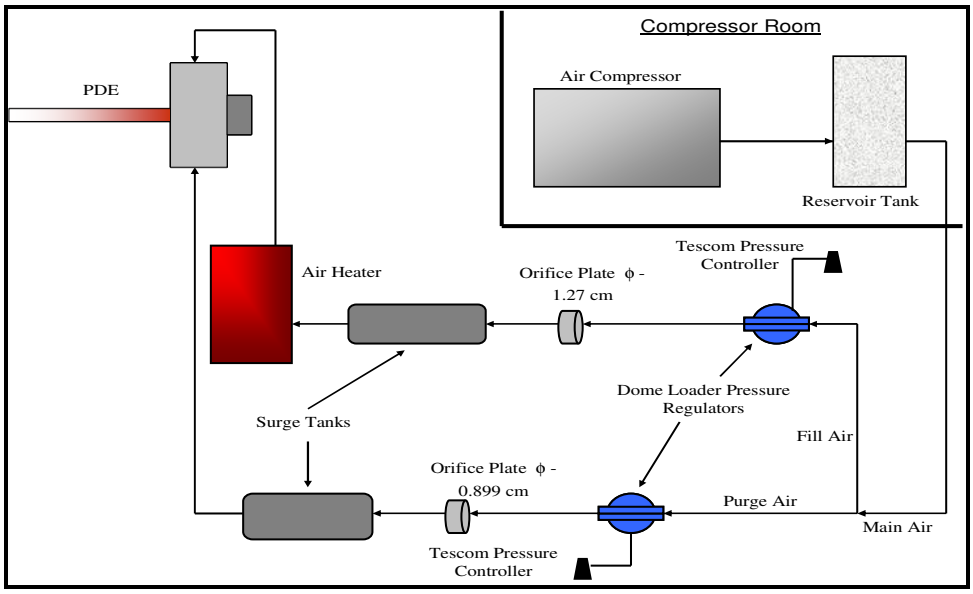

Figure 22. Diagram of PDE main air supply system

Air Mass Flow Rate Regulation

The *LabVIEW* program determines the necessary airflow rate based on operating conditions that are input into the program. To determine the airflow rate, it is necessary to input the frequency, tube volume, and fill fraction. Again, the fill fraction is the standard temperature and pressure air volume admitted divided b the tube volume. Air mass flow rate is calculated using Equation (15).

$$\dot{m}_{air} = \frac{(\#_{tubes})(freq)(V_{tube})(FF)(P)}{(R)(T)} \tag{15}$$

where *freq* is the *cycle frequency*, V_{tube} is the *tube volume*, $\#_{tubes}$ is the *number of tubes*, *FF* is the *fill fraction*, *P* is the *pressure*, *R* is the *specific gas constant* for air (287.1 J/kg*K or 1,716 ft^2/s^2*ºR), and *T* is the *air temperature*. Once the *LabVIEW* program has calculated the required air mass flow rate, it sends an electronic signal to the Tescom that

sends a pneumatic pressure signal to a dome loader that increases the pressure upstream of the orifice plate. The increase in upstream pressure causes a pressure differental, ΔP, across the orifice plate. The orifice plates are designed to provide a specific air mass flow rate for a given pressure differential. There are also pressure transducers located both upstream and downstream of the orifice plates that detect and send the static pressure readings back to the *LabVIEW* program. Once the flow is choked at the orifice plate, only the upstream pressure is necessary to determine air mass flow. The signal from the pressure transducers serves as a control loop, which ensures the correct air mass flow rate is provided at all times.

Liquid Fuel Supply System

There were no gaseous fuels used in this effort, only liquid, therefore liquid fuel will henceforth be denoted as just fuel. Six different fuels were used in this effort: JP-8, JP-7, JP-10, RP-1, JP-900, and S-8. JP-8 was used more often than the other fuels because it is considered the baseline fuel for this research. The fuel supply system is identical for all of the six fuels, and therefore it will only be presented once. JP-8 required deoxygenation, or conditioning, before use. The details of the conditioning process are discussed in detail in the next section. This section will discuss the fuels as if it has already undergone the conditioning process. JP-8 is obtained from AFRL/PRTG and stored in D-Bay in 208.20 L (55 gallon) fuel drums. JP-7, JP-10, RP-1, JP-900, and S-8 are all obtained locally from AFRL/PRTG and stored in D-Bay in 18.93 L (5 gallon) fuel containers until use.

For testing, fuel was placed in a 41.64 L (11 gallon) stainless steel fuel reservoir (S/N 28108-007), shown in Figure 23. The fuel is pressure fed using compressed nitrogen into two 9.46 L (2.5 gallon) Greer hydraulic accumulators (Model # 30A-2½A), shown in Figure 23, that are rated to 204.14 atm (3,000 psi). Once the fuel is transferred into the accumulators, the fuel reservoir is not used. High-pressure nitrogen bottles pressurize both accumulators. The accumulators use a rubber diaphragm to separate the nitrogen and the fuel. The high-pressure nitrogen is regulated with a dome loader type pressure regulator. The fuel mass flow regulation process is discussed in a later section. During testing, a ball valve is opened in the fuel room that causes the fuel to be pushed out of the accumulators and into fuel lines in the test cell. Figure 24 is a schematic of the accumulator fill and fuel feed processes.

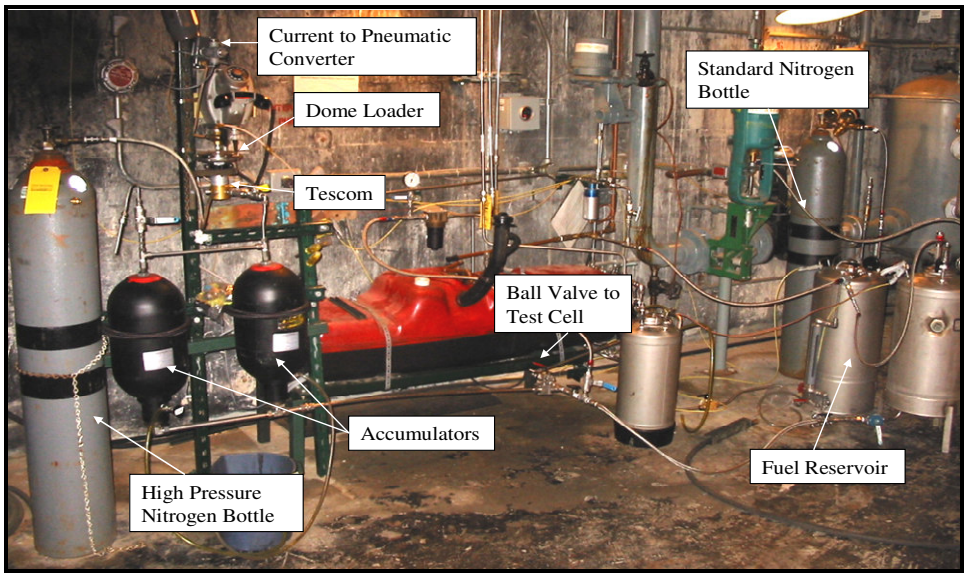

Figure 23. Photograph of the liquid fuel feed system inside the fuel room

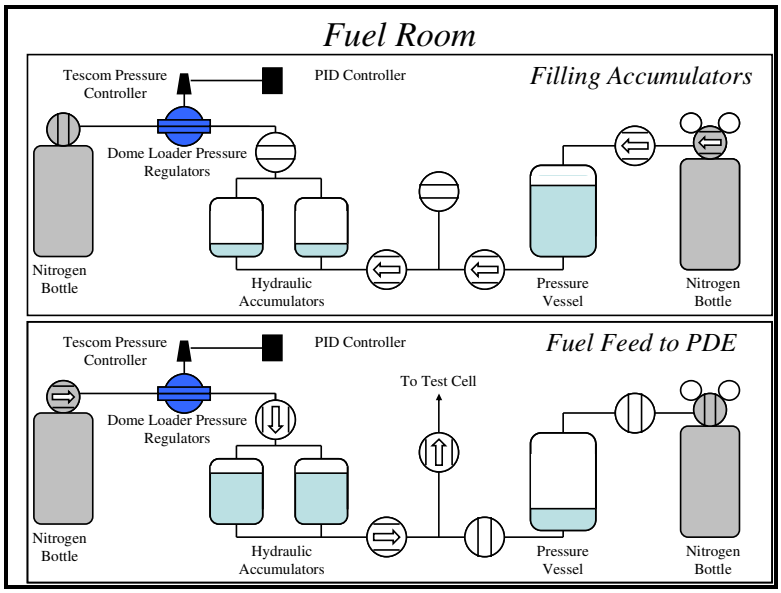

Figure 24. Schematic diagram of the liquid flow in the fuel room during both filling and testing

Once the fuel has moved into the test cell, it intersects a Flow Technology turbine volumetric flow meter (Model # FT4-8AEU2-LEAT5). There is a bypass built around the flow meter to prevent damage to the flow meter during initial fuel system pressurization. During testing, the flow meter bypass is closed and the path to the flow meter is opened. A thermocouple is located immediately downstream of the flow meter to allow for temperature compensation in fuel density during fuel mass flow rate calculations within the *LabVIEW* program. After the fuel flow meter, the fuel line travels to a pneumatic valve, referred to as the last chance valve. The last chance valve is commanded to open and close by the *LabVIEW* program in the control room. During testing the last chance valve is used to commence and terminate fuel flow. After the last chance valve, the fuel line enters the test stand, where the fuel flows through the heat exchangers into the fill air manifold. During testing, the fuel was injected into the fill air manifold by means of a spray bar and a series of Delevan Spray Technologies flow

nozzles. The flow nozzles come in a variety of sizes and can be removed and replaced to regulate the amount of fuel flow. The spray bar is welded inside of the fill air manifold; and is shown in Figure 25, along with a representative Delavan nozzle.

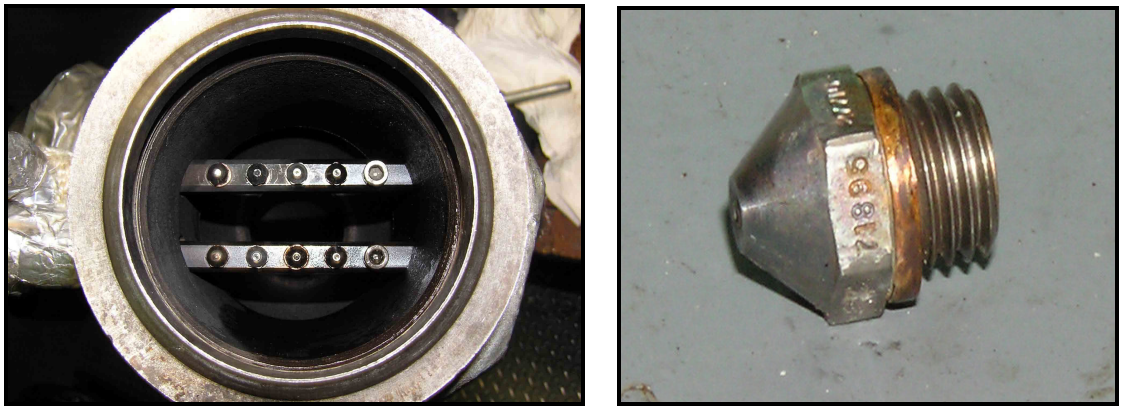

Figure 25. Photographs of the fill air manifold with spray bars (left) and a representative fuel flow nozzle (right)

Fuel Deoxygenation

JP-8 is the only fuel used in this effort that requires deoxygenation, the removal of excess oxygen from the fuel. This is necessary, because dissolved air in the fuel, specifically the oxygen molecules, will begin reacting with the fuel at temperatures at or above 450 K (350 ºF). The reaction of oxygen and fuel creates carbon deposits, or coking, on metal surfaces. Fuel deoxygenation is sufficient to mitigate coking up to 810 K (1000 ºF), where endothermic reactions create coking due to fuel cracking (Tucker, 2005). The methods developed to mitigate coking within the endothermic regime are discussed in Appendix D.

The method of deoxygenation used in this effort is sparging. Sparging is the process of bubbling nitrogen through the fuel to agitate and displace the dissolved oxygen

in the fuel. All fuel sparging took place in a 41.64 L (11 gallon) fuel reservoir, equipped with a coiled section of stainless steel tubing with numerous small holes drilled in it, shown in Figure 26. The section of coiled tubing is connected to non-drilled stainless steel tubing that is attached to a standard nitrogen bottle and manual pressure regulator. A ball valve is welded to the top of the reservoir to allow for venting, shown in Figure 26. During sparging the ball valve is opened and the nitrogen is driven through the drilled section of coiled tubing at a low rate (a rate just high enough for the nitrogen to be audibly detected bubbling through the fuel) and allowed to bubble through the fuel. The oxygen and excess nitrogen are expelled from the fuel tank into the atmosphere. Once a sufficient volume of nitrogen has been bubbled though the fuel, the vent ball valve is closed and the fuel reservoir is pressurized. This completes the sparging process, and the fuel is ready to be moved into the accumulators. (Panzenhagen, 2004:3.12-3.15)

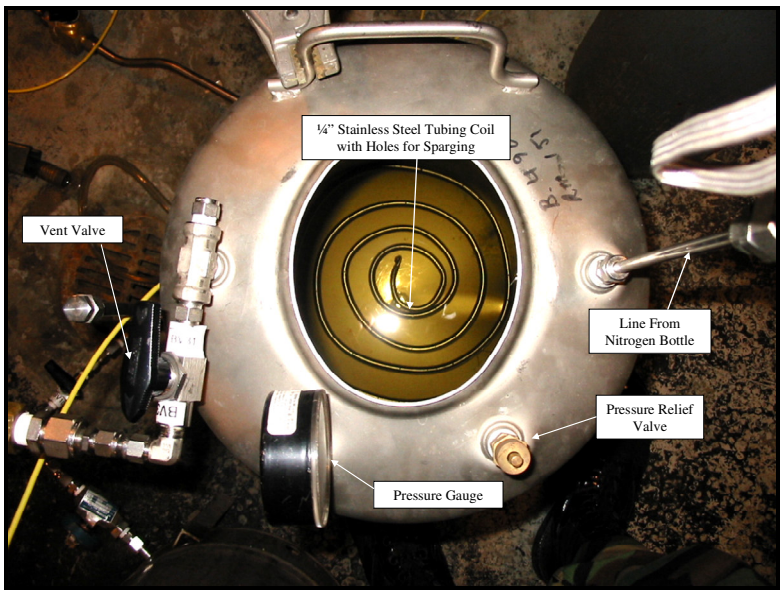

Figure 26. Photograph of the top view of fuel conditioning holding tank with nitrogen bubbling coiled tube at the tank bottom

Constant Equivalence Ratio Fuel Regulation System

A new fuel flow rate regulation system has been installed in D-Bay as a part of this research. The objective of the regulation system is to provide a constant fuel mass flow rate and equivalence ratio during large fluctuations in fuel density. Before the new system was installed, the fuel flow rate was set by both the selection of Delavan nozzles and the pressure applied to the liquid fuel accumulators. The fuel injection nozzles could not be changed during firing for obvious reasons. A manual pressure regulator attached to a high-pressure nitrogen bottle regulated the amount of pressure applied to the fuel. The manual pressure regulator was located in the fuel room that is inaccessible during firing of the PDE; hence, the fuel mass flow rate could not be varied during testing. As stated in the Chapter II, the fuel mass flow drops as the fuel is heated; so it is necessary to be able to increase the fuel pressure to keep a constant fuel mass flow rate.

The new constant equivalence ratio system allows the *LabVIEW* program to control the fuel mass flow rate in a similar fashion as the air mass flow rate regulation system. A pneumatic pressure regulator has replaced the manual pressure regulator leading from the high-pressure nitrogen bottle. The *LabVIEW* program calculates what pressure needs to be applied to the accumulators for a given injector nozzle arrangement to supply the necessary fuel mass flow rate, based on Equation (13). The desired pressure level is determined by the *LabVIEW* program, which sends a signal to a Tescom Electropneumatic PID Controller (Model # 26-2015T24A272) that actuates the pressure regulator. The fuel flow meter in the test cell measures the actual fuel mass flow rate and sends a signal back to the *LabVIEW* program. The signal from the fuel flow meter serves

as a control loop, which ensures the correct fuel mass flow rate and equivalence ratio are maintained.

Once the desired air mass flow rate is determined, the *LabVIEW* program only requires one additional input, equivalence ratio (Φ), to ascertain the required fuel mass flow ratio. Equivalence ratio is defined by equation (16).

$$\Phi = \frac{\left(\frac{\dot{m}_{fuel}}{\dot{m}_{air}}\right)_{actual}}{\left(\frac{\dot{m}_{fuel}}{\dot{m}_{air}}\right)_{st}} \tag{16}$$

where Φ is the equivalence ratio, $\dot{m}_{fuel}$ is the actual fuel mass flow rate, $\dot{m}_{air}$ is the *actual air mass flow rate,* and $\left(\frac{\dot{m}_{fuel}}{\dot{m}_{air}}\right)_{st}$ is the s*toichiometric ratio of fuel and air mass flow rate*, which is a know value for each fuel. By rearranging Equation (16), Equation (17) can be used to solve for the required fuel mass flow rate.

$$\dot{m}_{fuel} = \dot{m}_{air} * \Phi * \left(\frac{\dot{m}_{fuel}}{\dot{m}_{air}}\right)_{st} \tag{17}$$

Ignition System

The PDE uses a 12 VDC MSD Digital DIS-4 ignition system to provide the spark energy to initiates combustion. The angular position of the camshaft is read by a BEI optical endcoder (Model # H25) and sent to the *LabVIEW* program. The *LabVIEW* program energizes the encoder. An ignition delay has been implemented in the ignition

system to mitigate the chance of backfiring. The ignition delay is input by the operator, into the *LabVIEW* program. The *LabVIEW* program uses the ignition delay and frequency to determine the ignition timing. Once the ignition timing has been determined, the *LabVIEW* program transmits a signal to the ignition relay box. The relay box sends the signal to the 12 VDC MSD Digital DIS-4 ignition system. During each cycle, the ignition system uses four 105-115 mJ (0.93-1.02 in-lbf) sparks per tube for a total ignition energy of 420-460 mJ (3.72-4.07 in-lbf) per tube. The ignition system utilizes modified NGK spark plugs as an ignition source. The NGK spark plugs have the grounding electrode removed and a small piece of tube welded to the end.

Pulse Detonation Engine

The research PDE in D-Bay uses the head of a General Motors Quad 4 engine with dual overhead camshafts shown in Figure 27. A variable speed Baldor electrical motor (Model # M4102T) drives a timing belt to turn the camshafts. The *LabVIEW* program supplies the motor control and frequency. The General Motors Quad 4 engine is designed with four valves in each cylinder head; typically, two are used for intake and two are used for exhaust. The PDE is designed to use the two intake valves for injection of a fuel air mixture during the fill cycle. Similarly, the two exhaust valves allow for injection of the purge air during the purge cycle.

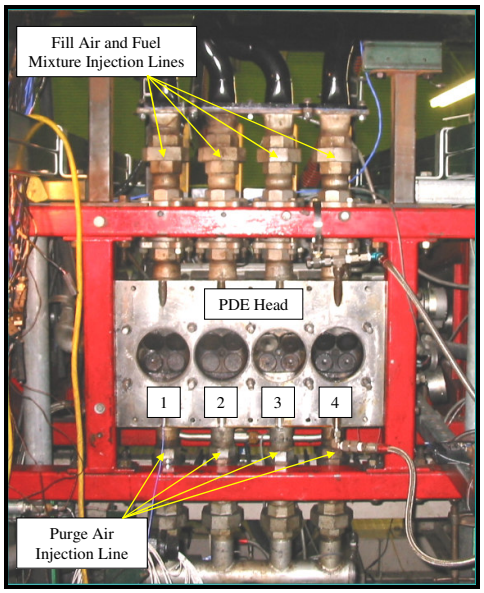

Figure 27. Photograph of GM Quad 4 engine head being used by PDE research engine with tube locations denoted by Arabic numerals

A Viking electric oil pump (Model # FH432) along with an external oil reservoir provide automotive oil to the valve train. The automotive oil provides all of the necessary lubrication to the engine. A 1.5 hp Teel electric water pump (Model # 9HN01) supplies water to the PDE engine head. The water is pumped through the existing head cooling water ports.

The PDE detonation tubes are attached to the engine head with mounting plates. The 1.27 cm (0.5 in) thick stainless steel mounting plates are fixed to the engine head with existing head bolts and nuts. While the mounting plates can vary, all mounting plates used in this effort were threaded to accept a 2" national pipe thread (NPT). To seal the mounting plates to the engine head, a stock head gasket was placed between the head and the mounting plates.

When using liquid hydrocarbon fuels it is necessary to use a detonation-initiating device to achieve detonations within a reasonable length of tube. Numerous types of detonation initiation methods exist, including detonation tripping devices, detonation branching, and predetonators (Tucker, 2003; Panzenhagen, 2004; and Gallia, 2006). For this research a 0.914 m (36 in) structurally enhanced schelkin-like spiral (Schelkin, 1940) was used, shown in Figure 28. The spiral is installed prior to the mounting plates and held in place by the mounting plates. The detonation tube is then slid over the spiral and threaded into the mounting plate.

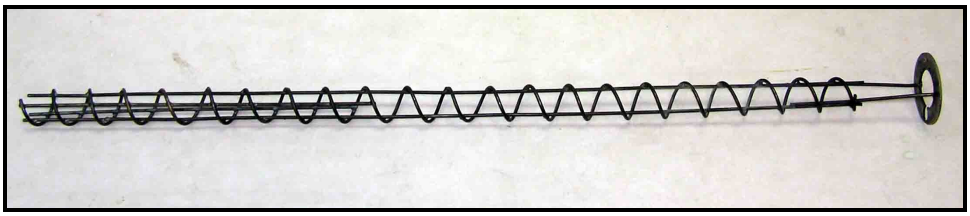

Figure 28. Photograph of a schelkin-like spiral with structural support

Heat Exchanger Configuration

Two stainless steel heat exchangers were developed for this effort. Two identical stainless steel heat exchangers were built. One of the stainless steel heat exchangers is shown in Figure 29. These heat exchangers were constructed of two 91.4 cm (36 in) long concentric tubes. The inner tube was fabricated from 2" type 316 stainless steel schedule 40 pipe and the outer tube was fabricated from 2 ½" type 316 stainless steel schedule 40 pipe. The inner and outer tubes were welded to 7.62 cm x 7.62 cm x 6.35 mm (4 in x 4 in x 0.25 in) type 316 stainless steel plates on both ends. When constructed a 1.22 mm

(0.048 in) annular gap was left between the inner and outer tubes for the fuel to flow. The technical drawings of the stainless steel heat exchanger are located in Appendix E.

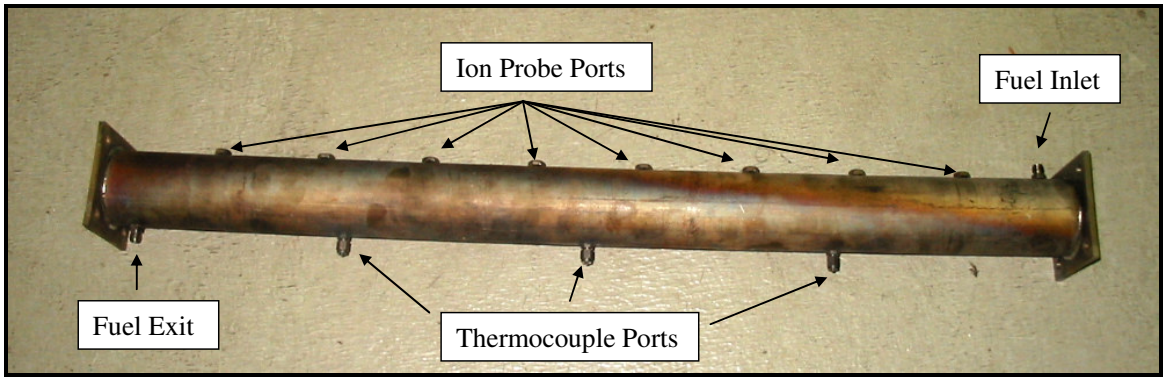

Figure 29. Photograph of one of the stainless steel heat exchangers after extensive testing

The outer tube had two ¼" Swagelok male unions welded at opposite ends with a 180º radial offset. These fittings served as the inlet and outlet for the fuel. Three 1/8" male Swagelok fittings were welded to the outer tube, aligned radially with the fuel outlet fitting and axially at 22.86 cm (9 in), 45.72 cm (18 in), and 68.58 cm (27 in). Similar heat exchangers have been built, but lacked the capability to be instrumented for wavespeed data collection (Miser, 2005). To alleviate the instrumentation problem, a method was developed to install ion probe ports with minimal degradation of the fuel flow inside the heat exchanger. Ion probes are discussed in a later section. Eight 3/8"-24 stainless steel nuts were welded to the outer tube to allow an ion probe to be fastened. All eight of the nuts were aligned radially with the fuel inlet fitting. The axial positions of the nuts are displayed in Table 6. For an ion probe to measure the wavespeed accurately, it must protrude slightly inside the detonation tube. To allow the ion probe to penetrate the detonation tube, a hole was drilled and tapped through both the

inner and outer tubes at the location of each nut. The gap between the inner and outer tube was welded together around each hole to prevent fuel from leaking around the ion probe.

Table 6. Ion probe port locations along the stainless steel heat exchangers

Ion Probe Port Number	Axial Location [cm]	Axial Location [in]
1	10.16	4
2	20.32	8
3	30.48	12
4	40.64	16
5	50.8	20
6	60.96	24
7	71.12	28
8	81.28	32

To attach the heat exchangers to existing detonation tube sections, four (two for each heat exchanger) 15.24 cm (6 in) extensions were fabricated from 2" type 316 stainless steel schedule 40 pipe. A 7.62 cm x 7.62 cm x 6.35 mm (4 in x 4 in x 0.25 in) type 316 stainless steel endplate was welded at one end of the extension. The end plates of the extension and the endplates of the heat exchanger bolt together. A gasket is placed between the extension and the heat exchanger to prevent leakage. The end of the extension opposite the end plate is threaded with male 2" NPT that is used to connect to other detonation tube sections with female 2" NPT pipe collars as shown in Figure 30. In each extension two 3/8"-24 stainless steel nuts were welded to the extension at 2.54 cm (1 in) and 10.15 cm (4 in) from the end plate, to serve as ion probe ports. A 1/8" Swagelok union was welded to each extension 6.35 cm (2.5 in) from the end plate and

aligned radially with the ion probe ports. The 1/8" Swagelok union welded to the extension to serve as a thermocouple port.

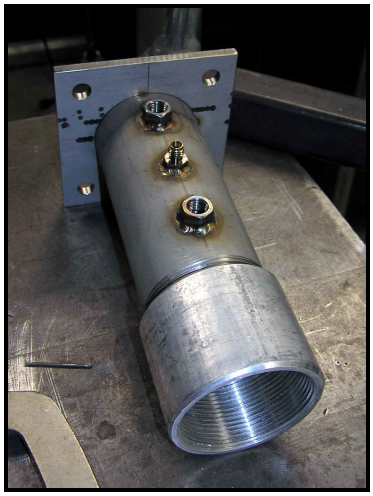

Figure 30. Photograph of a heat exchanger connecting extension connected to a female 2" pipe collar

The heat exchangers were hydrostatically pressure tested in accordance with ASME B31.3, paragraph 345.4. The rated working temperature and pressure for the stainless steel heat exchangers are 866.5 K (1100 ºF) and 68 atm (1000 psi), respectively. The heat transfer characteristics of the heat exchangers were unknown prior to testing. Previous work has shown that a similar heat exchanger developed very complex heat transfer characteristics that could not easily be modeled (Miser, 2005:70-74). After initial testing, it was discovered that the fuel heating system could easily heat the fuel beyond the structural limits of the stainless steel heat exchanger due to thermally induced stresses; therefore, it was necessary to constantly monitor the fuel temperature and pressure combination to maintain safety. The monitored temperature and pressure values were compared to an operating diagram. The operating diagram is a pressure versus

temperature plot that depicts the safe combinations of fuel temperature and pressure based on the rating of the heat exchanger (Figure 31). Note that the temperature and pressure values on Figure 31 are in English units, because the equipment used to monitor the fuel temperature and pressure displayed English units.

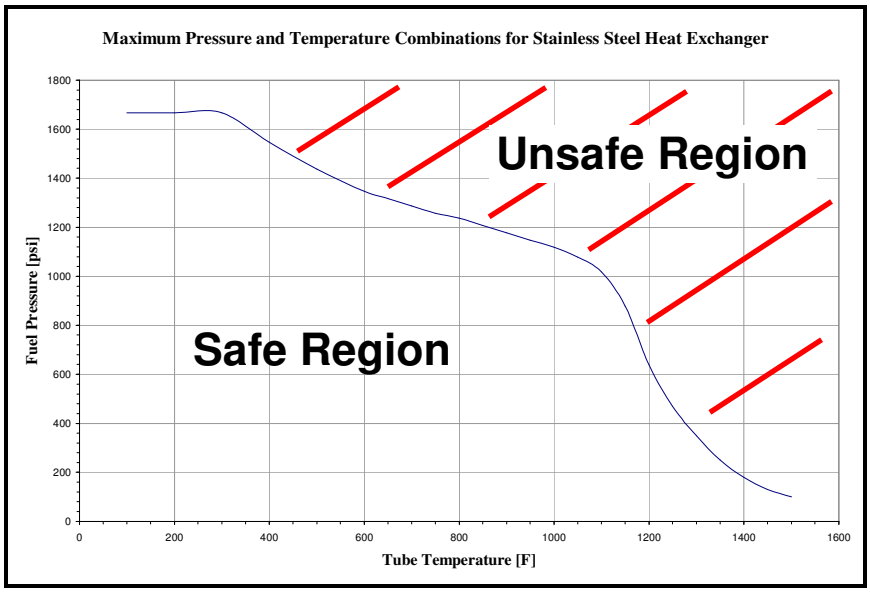

Figure 31. Fuel temperature and pressure operating limits for the stainless steel heat exchanger

Instrumentation

The instrumentation for all tests was identical, and consisted of thermocouples, pressure transducers, and ion probes. Temperature was measured at the inlet and outlet of each heat exchanger using 1/16" J-Type thermocouples placed in the center of the fuel flow path. Fuel injection temperature was gathered at the inlet to the fill air manifold using a 1/16" J-Type thermocouple. The fuel-air mixture temperature was gathered directly before the entrance to the PDE head using a 1/8" T-Type thermocouple. The temperature in the head of both tubes was found using a 1/8" T-Type thermocouple,

located at the top of the head cavity. External heat exchanger wall temperatures were measured with J-type thermocouples mounted externally by compression clamps to the PDE detonation tube. A pressure transducer was situated in the head cavity of tubes one and four to gather the head pressure data used to determine the ignition time. Ion probes were placed in the ion probe ports in both the tube one and four heat exchangers. The axial distances from the PDE head to the location of the ion probes and the tube numbers that they were located on are shown in Table 7.

Table 7. Location of ion probes along detonation tubes used during testing

Ion Probe Number	Tube Number	Axial Location [cm]	Axial Location [in]
1	1	60.33	23.75
2	1	70.49	27.75
3	1	80.65	31.75
4	1	90.81	35.75
5	1	100.97	39.75
6	1	111.13	43.75
7	4	61.94	24.39
8	4	72.10	28.39
9	4	82.26	32.39
10	4	92.42	36.39
11	4	102.58	40.39
12	4	112.74	44.39

Nitrogen Purge System

A nitrogen purge system was designed to prevent supercritical fuel from remaining in the heat exchangers at the end of a test (Figure 32). The nitrogen purge system consists of a high-pressure nitrogen bottle, manual pressure regulator, pneumatic valve, check valve, and ball valve. Before testing began, the ball valve was opened to allow for operation of the nitrogen purge system. The manual pressure regulator was set above the critical pressure of the fuel. The pneumatic valve is placed in the nitrogen

purge line to commence and terminate the nitrogen flow. The pneumatic valve can be activated from the *LabVIEW* program. Once a test has ended, the pneumatic valve is opened and the liquid last chance valve is closed, allowing the nitrogen to purge the heat exchangers of supercritical fuel. A check valve is located directly after the pneumatic valve to prevent fuel from entering the nitrogen line.

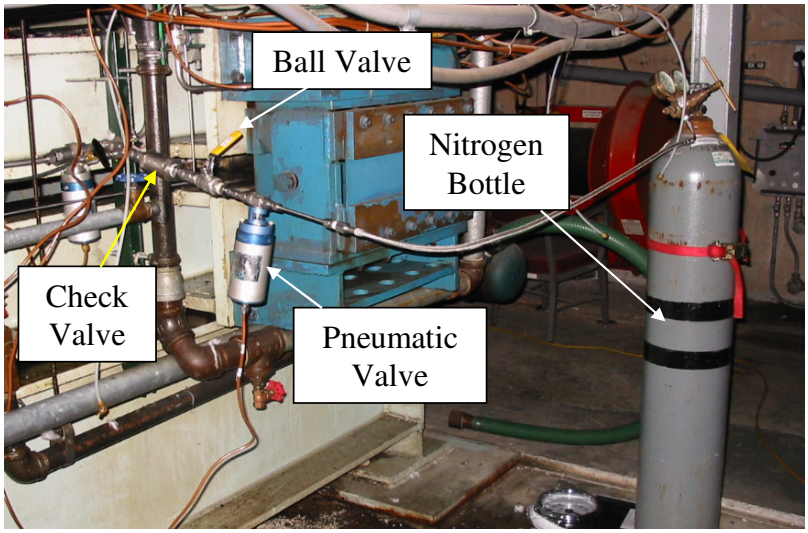

Figure 32. Photograph of the nitrogen purge system

Supercritical Fuel Heating System

All six fuels were tested using the supercritical fuel heating system, shown in Figure 33. Fuels were tested at temperatures between 422 and 755.4 K (300 and 900 ºF). The supercritical fuel heating system consisted of the nitrogen purge system, two stainless steel heat exchangers, fuel filter assembly, instrumentation, and the associated tubing and fittings necessary to connect the critical components. All components of the supercritical fuel heating system are connected by ¼" stainless steel tubing and various stainless steel Swagelok fittings. The PDE was setup with two detonation tubes, each

with a stainless steel heat exchanger. Detonation tubes one and four were used for all tests.

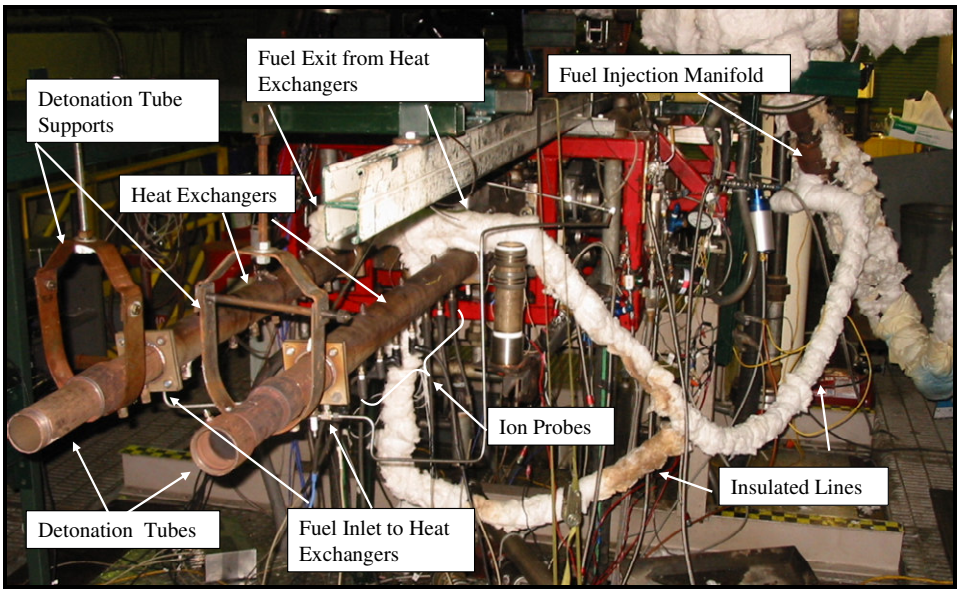

Figure 33. Photograph of the supercritical fuel heating system with heat exchangers installed on detonation tubes one and four

A Swagelok Tee-Type filter (Part No. SS-4TF-LF) is installed in the fuel line directly before the entrance to the fill air manifold. A filter was necessary to capture the small amounts of coking that occurred at temperatures near 755.4 K (900 ºF). If the coking was not filtered out before reaching the fill air manifold, it would clog up the Delevan flow nozzles. A 90 micron filter element (Part No. SS-4F-K4-90) was used in the filter for all of the tests.

Supports were used to prevent sagging of the detonation tubes during testing. Previous PDE heat exchanger research demonstrated that the weight of the heat

exchanger caused the detonation tubes to bend (Miser, 2005). The supports can be seen in Figure 33.

The fuel enters the test stand through a ball valve where the flow is split into two fuel lines. One fuel line leads to the inlet of the heat exchanger on tube four, while the other fuel line leads to the inlet of the heat exchanger on tube one. After the two fuel paths have exited their respective heat exchanger, they are teed back together. The fuel is then led through the filter and to the fill air manifold, where it is injected into the air stream. The fuel lines that carry heated fuel (fuel that has traversed through a heat exchanger) are insulated with fiberglass insulation. The flow path and instrumentation are shown in schematic form in Figure 34.

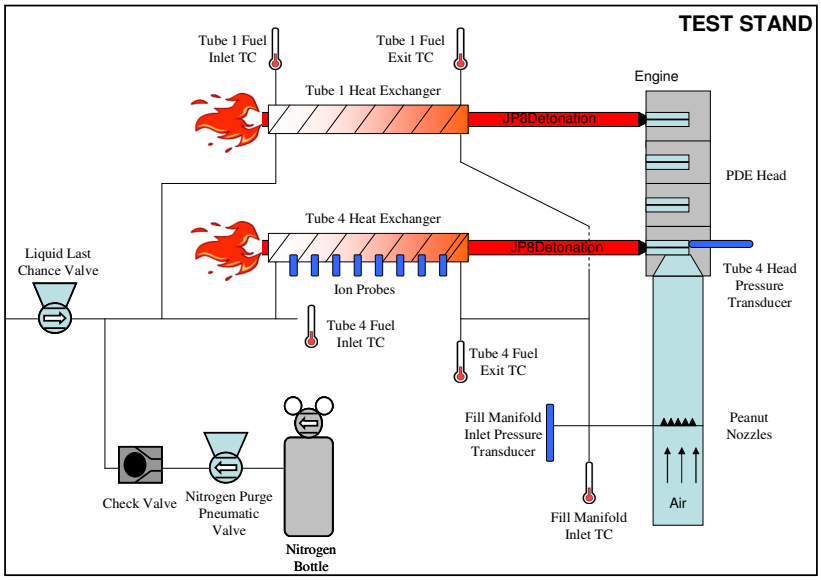

Figure 34. Diagram of PDE engine with supercritical fuel heating system and instrumentation

Test Procedure

The procedures of all tests for this research were identical. Prior to the beginning of a test, the water supply, oil pump, encoder, and engine were all energized. The engine was brought to the appropriate frequency and the ignition delay was set. The fill fraction, purge fraction, tube volume, number of tubes, orifice plate sizes, and desired equivalence ratio were all input into the *LabVIEW* program on the control computer. The air heater was set at the appropriate temperature. Once the air reached the input temperature and desired mass flow rate, testing was ready to begin.

To commence testing low-speed data collection was initiated, the igniters were energized, and the fuel flow was initiated by opening the last chance valve. After the fuel mass flow rate steadied, combustion began in the detonation tubes. The fuel injection temperature was monitored as it rose from near ambient. At specific temperatures, data sets were taken on the high-speed computer, gathering the pressure transducer and ion probe data. The pressure was increased throughout the test to maintain a constant equivalence ratio. Once either the fuel injection temperature reached 755.4 K (900 °F) or the structural limit of the heat exchanger was met the test was finished. To end the test the last chance valve was closed and the nitrogen purge system was activated. Small amounts of ignition occurred as the nitrogen purge system pushed the residual fuel out of the heat exchangers. The igniters were turned off once all combustion had ceased. This ended the test.

IV. Data Reduction and Uncertainty Analysis

Data Acquisition

All combustion data was gathered on a dedicated computer employing a *LabVIEW* program named *OnLineWavespeed*. Using *OnLineWavespeed*, 16 channels of raw data (two spark traces, two head pressure traces, and 12 ion probe traces) were collected in 0.5 second intervals. The master scan rate was set at 1,000,000 scans per second, therefore 500,000 data points were gathered for each channel in 0.5 seconds. The output file from this program was roughly 20 megabits of binary data. The output file also includes a curve fit to convert the binary values back into floating point. In this form, the data must be refined if any usable information is to be gathered.

Data Reduction

A C++ program, named *PTFinder*, was employed to convert the raw data to a usable form. *PTFinder* translates the binary data into floating point using the curve fit saved with the data. The program then segments the data into separate firing cycles using the spark trace. Each spark trace denotes a new firing cycle.

Each firing cycle is then analyzed for ignition time information. The head pressure trace data is passed through a fourth-order, 401 point Savitzky-Golay digital finite-impulse response filter (Parker, 2003:1). An example of the effect of the pressure trace filter is shown in Figure 35. The filter is used to smooth out the data and remove the high frequency noise. Significant high frequency data is lost using this filter, but the shape of the pressure trace remains. Linear regression is then used to determine the slope

of the pressure curve. A window of 1000 points is analyzed to determine the average pressure rise. The window begins with the first 1000 points of the pressure trace and moves forward along the pressure trace until an average pressure rise of 340.2 atm/sec (5000 psi/sec) is detected. The time in the center of the window is taken as the ignition time.

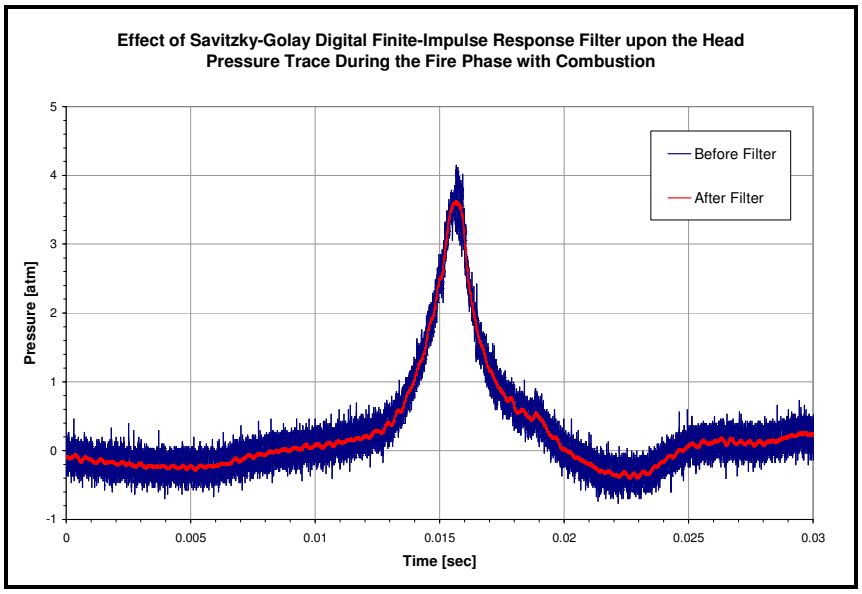

Figure 35. Effect of Savitzky-Golay digital finite-impulse response filter on the head pressure trace during the fire phase with combustion

After the ignition time is determined, the probe times are calculated. The probe times are the time that the combustion wave crosses each of the ion probes. To determine the probe times, *PTFinder* takes an average of the first 1000 points of the ion probe traces to find a baseline value for the trace. The program then looks for the trace to drop below the baseline value for at least 500 consecutive data points. The probe time is the first point in the series of 500 points below the baseline value. This method essentially finds

the corners of the ion probe trace and determines the time that they are found. Figure 36 is a plot of a sample pressure trace, along with a spark trace and eight ion probe traces.

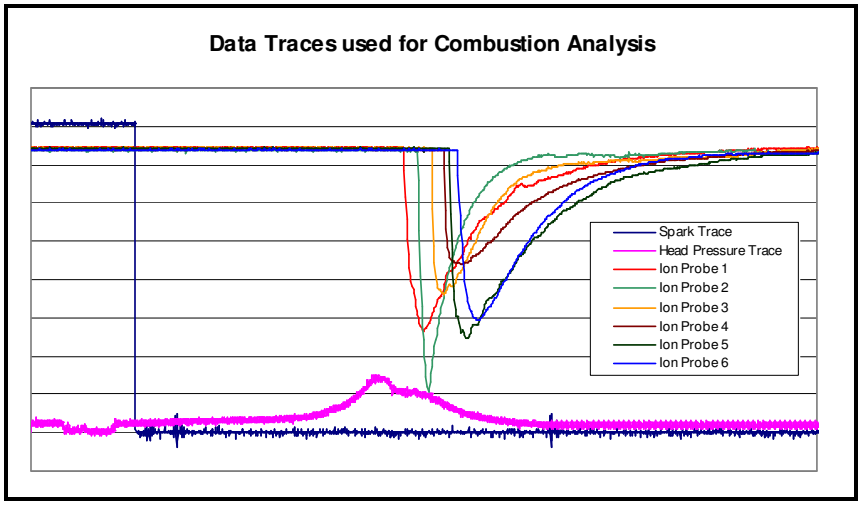

Figure 36. Representative output traces used to determine critical performance parameters

Once both the ignition times and probe times are found, they are inserted into an *Excel* spreadsheet. The spreadsheet first calculates the wavespeeds by dividing the difference in distance between two ion probes (10.16 cm or 4 in for this effort) by the difference in the corresponding probe times. The spreadsheet then looks for wavespeeds above the upper C-J velocity of 1800 m/s (5905.5 ft/s). Once a wavespeed above the upper C-J limit is found, the program linearly interpolates between the wavespeed above the upper C-J wavespeed and the wavespeed at the location before it (below the upper C-J wavespeed) to determine the time and location where a wavespeed of exactly 1800 m/s (5905.5 ft/s) occurs. The time and location found are the DDT time and the detonation distance, respectively.

The final performance parameter that was determined was the percent of ignitions that result in detonations. There is a large amount of controversy in the pulse detonation engineering community over the wavespeed threshold used to determine if a detonation has occurred in a hydrocarbon/air mixture. Many scientists use a wavespeed threshold of 1400 m/s, while others use 1800 m/s. To aid in determining what threshold would be used in this research, a histogram of every wavespeed calculated for JP-8 during this effort was created (Figure 37).

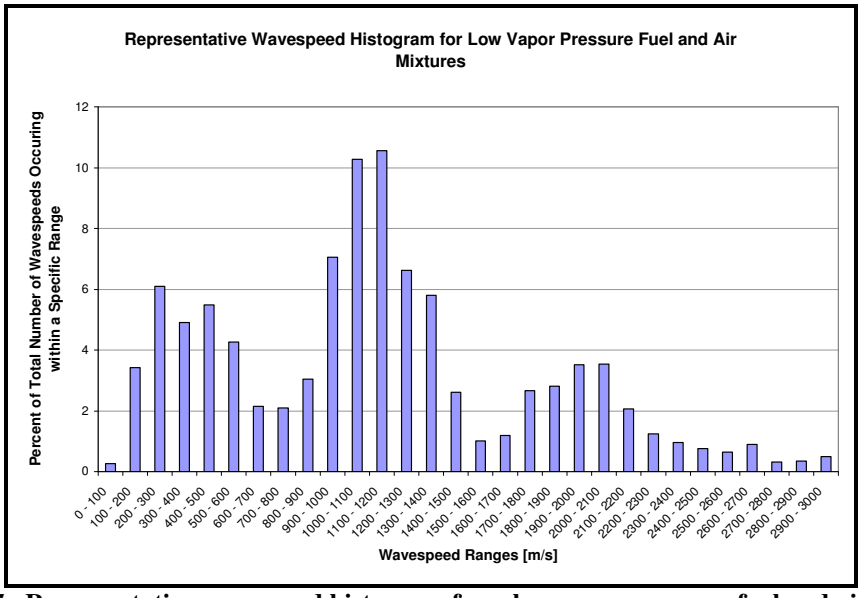

Figure 37. Representative wavespeed histogram for a low vapor pressure fuel and air mixture

The wavespeed histogram is a tool used to determining the major wavespeed regimes seen in the PDE detonation tube. There are three discernable wavespeed regimes. The first regime is centered around 400 m/s, which is in the weak deflagration regime. The third regime is centered around 2000 m/s, which is in the strong detonation regime for low vapor pressure fuel/air mixtures. The second regime is centered around 1100 m/s,

which is approximately the choked flame speed. Note that the wavespeeds shown in Figure 37 were only taken at axial positions between 0.603 and 1.127 m (23.75 and 44.385 in) on 1.829 m (72 in) tubes. This means that the wavespeeds shown in Figure 37 are skewed toward the second regime. It is likely that if wavespeeds were taken along the entire tube that the first and third regimes would outweigh the second regime. Based on Figure 37, there is no evidence that suggests a wavespeed cutoff of anything below the upper C-J wavespeed should be used to determine if a detonation has occurred. However, the local practice is to use 1400 m/s as the cutoff, and it has been shown that the difference in performance between detonations and choked flames is insignificant (Hoke, 2005:6). For these reasons, results using both the 1400 and 1800 m/s cutoffs are shown. Results for wavespeeds above 1400 m/s will be referred to as the 1400 m/s wavespeed percentage, and the results for wavespeeds above 1800 m/s will be referred to as the detonation percentage.

Statistical Inference

Statistical inference is a powerful tool used to understand experimental results. In the previous section, the method for determining one value for each parameter was laid out. This one value may or may not be identical to the next value determined for the same parameter due to the unsteadiness of the PDE cycle, and the inherent variations that occur during experimental research. To compensate for the aforementioned issues, several data points were taken for each parameter. The experimental mean was determined using Equation (18):

$$\bar{x} = \frac{\sum_{i=1}^{n} x_i}{n} \tag{18}$$

where $\bar{x}$ is the experimental mean, x_i are the individual data points, and n is the number of data points (Milton, 2003:203). All plots in Chapter V display the experimental mean unless noted.

To determine the precision of the experimental mean, the experimental standard deviation was found using Equation (19):

$$\sigma = \sqrt{\frac{\sum_{i=1}^{n} \left(\bar{x} - x_i\right)^2}{n-1}} \tag{19}$$

where σ is the experimental standard deviation (Milton, 2003:207). The experimental standard deviation is plotted in Chapter V wherever possible. Another method to illustrate the precision of the experimental mean is to use a confidence interval. A 95% confidence interval was determined for the results of the fuels study. The 95% confidence interval was computed using Equation (20):

$$CI = \bar{x} \pm \frac{t_{\alpha/2}\sigma}{\sqrt{n}} = \bar{x} \pm P_{\bar{x}} \tag{20}$$

where *CI* is the *confidence interval*, $P_{\bar{x}}$ is the *precision error*, and $t_{\alpha/2}$ is a *T-function* whose value is based on the number of data points and the level of confidence required (Milton, 2003:266). A table of values for $t_{\alpha/2}$ can be found in Milton (Milton, 2003:266).

95% confidence intervals are plotted as error bars in Appendix A. The utility of the precision error is discussed in the following section.

Equations (18) through (20) hinge on the assumption that the experimental results have a normal distribution (Milton, 2003:264). While a rigorous test of normality was not conducted, a simple histogram of five random data sets was plotted; and is shown in Figure 38. The shape of the histogram closely resembles that of a normal distribution. While this does not guarantee normality, it is a good check.

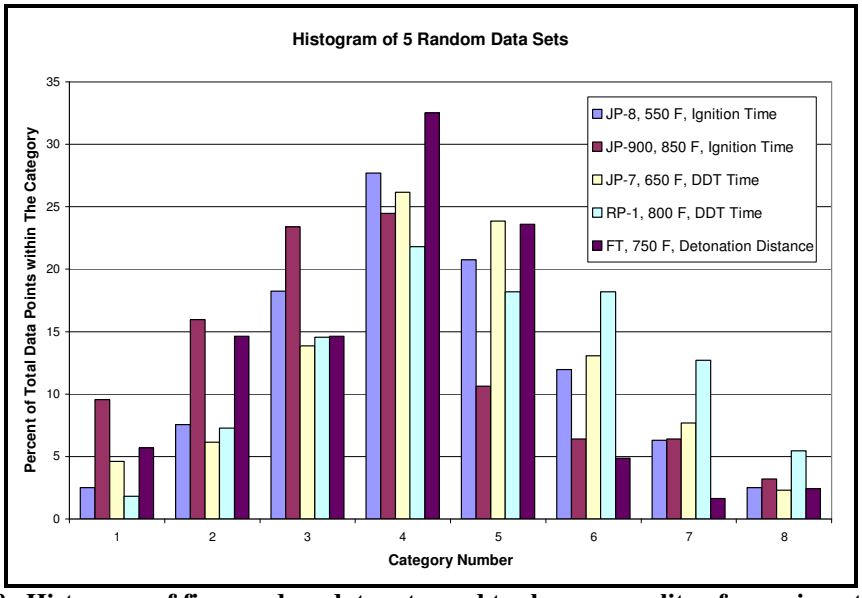

Figure 38. Histogram of five random data sets used to show normality of experimental results

Uncertainty Analysis

With any experimentation comes a certain amount of uncertainty, or error. The uncertainty can be mitigated, but never full eradicated. It is therefore necessary to analyze and understand the uncertainty involved with the results presented in this paper.

The uncertainty analysis was performed in accordance with techniques outlined in Coleman (Coleman, 1989).

The total uncertainty is a combination of the bias error and the precision error. The bias error, or bias, is a measure of the experimental uncertainty resulting from inaccuracies in measurements and data reduction. The bias is fixed for a particular variable, while the precision error varies for each data point. The method for determining the precision error was outlined in the previous section. The total uncertainty of the experimental result is determined using Equation (21):

$$U_{\bar{r}} = \sqrt{B_r^2 + P_{\bar{r}}^2} \tag{21}$$

where $U_{\bar{r}}$ is the *total uncertainty*, $B_{\bar{r}}$ is the *bias*, $P_{\bar{r}}$ is the *precision error*, and *r* the experimental result of interest. Since the precision error can be determined using Equations (18), (19), and (20), only the method for determining the bias is presented. (Coleman, 1989:7, 94-95)

During the course of any experiment, many variables are measured directly. The measurement of these variables has an inherent uncertainty. Often, there are several contributions to the uncertainty for each measured variable, known as elemental uncertainties. The uncertainty contributions are summed using a root-sum-square method, shown in Equation (22):

$$B_i = \sqrt{\sum_{k=1}^{m} \left(B_i\right)_k^2} \tag{22}$$

where there are *m* uncertainty contributors for the *i*th measured variable. (Coleman, 1989:79)

Since the variable of interest is not always measured during the experiment, the propagation of uncertainty from the measured variables to the variable of interest must be determined. If the experimental result *r* is a function of *i* variables, then the bias for the experimental result is determined using Equation (23):

$$B_r = \sqrt{\sum_{j=1}^{i}\left[\left(\frac{\partial r}{\partial X_j}\right)^2 B_j^2\right]} \tag{23}$$

where B_r is the *bias of the variable of interest*, *r* is the *variable of interest*, and B_i is the *bias of each measured variable*. The bias uncertainty analysis began with an analysis of the elemental bias uncertainties.

Elemental Bias Uncertainties

As stated earlier, elemental uncertainties are the root cause of the uncertainty in the experimental results. The elemental uncertainties propagate through the data reduction process, resulting in bias error. The causes of elemental uncertainties are discussed in detail.

Pressure Transducer Uncertainty

The PCB pressure transducers used in this research measure a voltage that can be converted to a pressure reading. The pressure transducers are calibrated to with in 0.1%

of the measured voltage. The maximum voltage produced during combustion is 0.0588 V, resulting in a PCB calibration uncertainty of ± 0.0588 mV. The pressure transducers are also limited by their response time. The response time of the pressure transducers is within 1 μsec, therefore the PCB rise time uncertainty is ± 0.5 μsec (PCB Piezotronics, 2003).

Signal Digitization Uncertainty

For every channel used to record data, a voltage range is selected by the operator. A small voltage range results in a higher resolution, while a large voltage range results in less resolution. The voltage range for the channels capturing head pressure data was ± 1 volt. This resulted in a step size of 0.5 mV, leading to a signal digitization uncertainty of ± 0.25 mV. The voltage range for the channels capturing the spark trace and ion probe data was 0 to 5 V. This resulted in a higher step size of 2.5 mV. The exact value of the ion probe and spark voltage is not used for any calculations, therefore no uncertainty is produced. In addition, all data samplings were taken at a rate of 1 MHz, or one sample per 1 μsec; resulting in a sample rate uncertainty of ± 0.5 μsec.

Ion Probe Uncertainties

The location of the ion probes was measured to the nearest 1.6 mm (1/16 in), therefore the ion probe location uncertainty is ± 0.8 mm (1/32 in). The distance between the ion probes affects the accuracy of the DDT time and detonation distance calculations. The ion probes are located 10.16 cm (4 in) apart, resulting in an ion probe spacing error

of ± 5.08 cm (2 in). The ion probe performance is limited by the probe response time of 0.1 μsec. Therefore the ion probe response uncertainty is ± 0.05 μsec (Zdenek, 2004).

Temperature Measurement Uncertainty

As stated in Chapter III, all temperature measurements were made using either J- or T-Type thermocouples. The J-Type thermocouples have an uncertainty of ± 3 K for the temperature range examined, while the T-Type thermocouples have an uncertainty of ± 1.5 K for the temperature range examined. The accuracy of the thermocouples varies slightly with temperature, but is negligible for this research. An additional uncertainty arises due to the method of data collection. High-speed data was collected as close to the desired temperature as possible, but resulted in a temperature collection error of ± 2 K.

Air Mass Flow Rate Uncertainty

The air mass flow rate accuracy is primarily dictated by the tolerance of the orifice plates in the fill air lines. The 1.27 cm (0.500 in) diameter orifice plates are accurate to ± 0.00254 cm (0.001 in). An improper air mass flow rate can also ensue due to the fluctuation in back pressure, resulting in error. The air control system is set to maintain the air mass flow rate for both the fill and purge cycles to within 1%. The average air mass flow rate is 13.0 lbm/min, resulting in an air control system uncertainty of ± 0.13 lbm/min.

Fuel Mass Flow Rate Uncertainty

The uncertainty of the fuel mass flow rate is dictated by the turbine flow meter calibration uncertainty. The calibration uncertainty is a result of the method of

calibration, discussed in Chapter II. The graduated cylinder used to measure volume is accurate is to 20 mL, resulting in a fuel volume calibration uncertainty of ± 10 mL. The time was measured using a stop watch that is accurate to 0.1 sec, resulting in a fuel time calibration uncertainty of ± 0.05 sec.

Summary of Elemental Uncertainties

Table 8 is a summary of all elemental errors determined for this research. In addition, the experimental results that each elemental error influences are displayed in Table 8.

Table 8. Summary of elemental uncertainties with the variables they influence

Elemental Uncertainty	Uncertainty Interval	Experimental Results Influenced
PCB Calibration	± 0.0588 mV	Ignition Time
PCB Rise Time	± 0.5 μsec	Ignition Time
Signal Digitization	± 0.25 mV	Ignition Time
Sample Rate	± 0.5 μsec	Wavespeed, Ignition Time, DDT Time
Ion Probe Location	± 0.8 mm	Wavespeed, DDT Time, Detonation Distance
Ion Probe Spacing	± 5.08 cm	Wavespeed, DDT Time, Detonation Distance
Ion Probe Response Time	± 0.05 μsec	Wavespeed, DDT Time, Detonation Distance
T-Type Thermocouple	± 3 K	Fuel Injection Temperature
J-Type Thermocouple	± 1.5 K	Fuel/Air Mixture Temperature
Temperature Collection	± 2 K	Fuel Injection Temp, Mixture Temp
Orifice Plate Toleratance	± 0.00254 cm	Equivalence Ratio
Air Control System	± 0.13 lbm/min	Equivalence Ratio
Fuel Volume Calibration	± 10 mL	Equivalence Ratio
Fuel Time Calibration	± 0.05 sec	Equivalence Ratio

Experimental Result Bias Uncertainty

The results of the uncertainty analysis for wavespeed, ignition time, DDT time, detonation location, temperature, and equivalence ratio are discussed below.

Wavespeed Uncertainty

The wavespeed is calculated by dividing the distance between two ion probes by the time it takes to travel between the two ion probes. The wavespeed bias uncertainty is a function of the location uncertainty and the time uncertainty. The location uncertainty is determined by the ion probe spacing and location uncertainties. The time uncertainty is a function of the sampling interval and ion probe response time uncertainties. Using Equations (22) and (23), the wavespeed bias uncertainty was calculated to be ± 55.12 m/s (180.9 ft/sec).

Ignition Time Uncertainty

The ignition time is calculated by determining when a pressure rise of 5000 psi per second occurs using the head pressure trace. The major sources of error are the time and pressure uncertainties. The time uncertainty is defined by the PCB response time and the sample rate uncertainties. The pressure uncertainty is a result of the pressure transducer calibration and signal digitization uncertainty. Using Equations (22) and (23), the ignition time bias uncertainty was calculated to be ± .0514 msec.

The bias uncertainty of ± .0514 msec does not take into account the largest uncertainty in ignition time results. The largest uncertainty occurs in the processing of the pressure signal. A window of 1000 data points was used to determine the ignition time. Since the data was taken at a rate of 1 MHz, a 1000-point window translates to 1 msec. Therefore, there was a $\pm$ 0.5 msec uncertainty associated with the ignition time results. This was higher than desired, so a study of the effect that the window size had on the mean and standard deviation of ignition time was performed. Several representative

samples were run through the *PTFinder* program with varying window sizes. The results for one example are shown in Figure 39. Figure 39 demonstrates that *PTFinder* will produce mean ignition time results within 2% difference with a window of 325 to 1000 data points. The standard deviation varies by less than 1% for window sizes of 575 to 1000 data points. Therefore, the effective window size uncertainty to the mean ignition time is $\pm$ 287.5 µsec, using the more conservative standard deviation as the benchmark. The total bias uncertainty was found by computing the root-sum-square of the original bias uncertainty (± .0514 msec) and the window size uncertainty, resulting in a total bias uncertainty for ignition time of ± 0.292 msec.

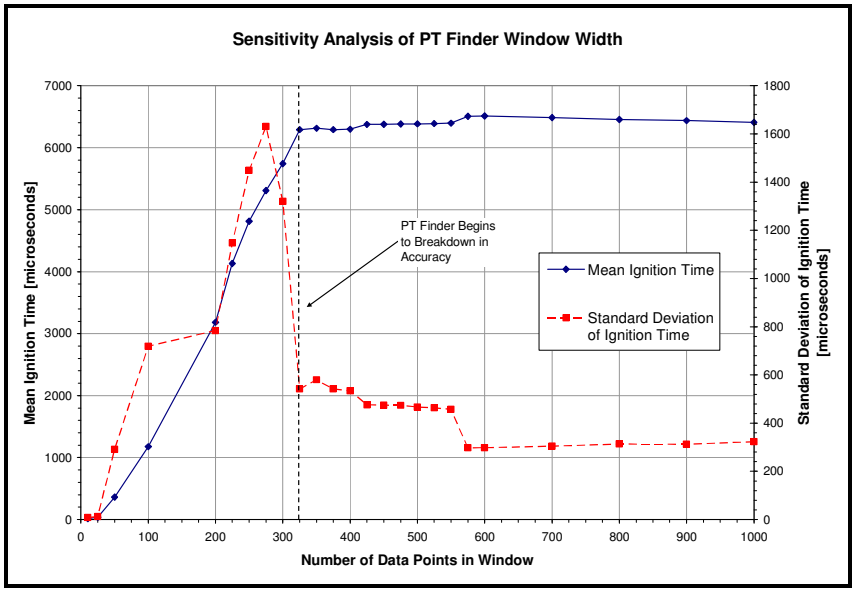

Figure 39. Sensitivity analysis of the *PTFinder* window size on the mean ignition time and the standard deviation of the ignition time

DDT Time Uncertainty

The DDT time is a function of the wavespeed and the probe time. Therefore, the DDT time bias uncertainty is a function of the location uncertainty, the time uncertainty,

and the wavespeed uncertainty. The location uncertainty is determined by the ion probe spacing and location uncertainties. The time uncertainty is a function of the sampling interval and ion probe response time uncertainties. The wavespeed uncertainty was determined earlier. Using Equations (22) and (23), the DDT time bias uncertainty was calculated to be ± 0.0568 msec.

Detonation Distance Uncertainty

The detonation distance is a function of the wavespeed and probe locations. Therefore, the wavespeed bias uncertainty is a function of the location uncertainty and the wavespeed uncertainty. The location uncertainty is determined by the ion probe spacing and location uncertainties. The wavespeed uncertainty was determined earlier. Using Equations (22) and (23), the bias uncertainty of the mean detonation distance was calculated to be ± .0568 m (2.24 in).

Temperature Uncertainty

The fuel injection temperature data was gathered with a T-Type thermocouple, while the fuel/air mixture temperature data was gathered with a J-Type thermocouple. Combining the thermocouple uncertainty and the temperature collection uncertainty using Equation (22), the bias uncertainty for the fuel injection and fuel/air mixture temperatures was found to be ± 3.6 K and 2.5 K, respectively.

Equivalence Ratio Uncertainty

Equivalence ratio, calculated with Equation (16), is a function of the fuel mass flow rate and the air mass flow rate. The major sources of equivalence ratio bias uncertainty are the fuel mass flow meter calibration uncertainty, orifice plate tolerance, and air control uncertainty. Using Equations (22) and (23), the bias uncertainty of the equivalence ratio was calculated to be ± 0.0147.

Total Experimental Uncertainty

As mentioned earlier, the total experimental uncertainty is determined by combining the bias and precision uncertainties using Equation (21). The bias uncertainties are constant for all data points of the same variable, while the precision uncertainties vary for each data point. Therefore, the total experimental uncertainty will vary by data point. A summary of the bias errors calculated earlier is shown in Table 9.

Table 9. Summary of bias uncertainties for experimental results

Experimental Result	Bias Uncertainty
Wavespeed	± 55.12 m/s
Ignition Time	± 0.292 msec
DDT Time	± 0.0568 msec
Detonation Distance	± 0.0568 m
Fuel Injection Temperature	± 3.6 K
Fuel/Air Mixture Temperature	± 2.5 K
Equivalence Ratio	± 0.0147

V. Result and Discussion

The analysis of various operating parameters for increasing fuel injection temperature is presented. The results include ignition time, deflagration to detonation time, detonation distance, and detonation percentage, with all parameters plotted versus fuel injection temperature. Each data point represents the mean value of 40 to 60 ignitions, using data from two tubes. The standard deviation is presented whenever possible.

This chapter begins with the results of the validation tests for the constant mass flow rate fuel delivery system. Next, the performance of the fuel heating system is presented. Subsequently, the effect of fuel injection temperature on wavespeed is presented. The effect of fuel injection temperature on the performance of the PDE with variation of the following operating parameters is shown: Fuel selection, internal spiral length, purge fraction, ignition delay, frequency, and equivalence ratio. Finally, issues with the heat exchanger are discussed.

Validation of Constant Fuel Mass Flow Rate Systems

A new fuel feed system was installed to allow for an increase in fuel pressure at the inlet to the fuel injection nozzles to compensate for the fuel density reduction that occurs with increasing fuel injection temperature (see Figure 18). The details of the new constant fuel mass flow rate system setup are located in Chapter III. The system was tested to determine if the fuel mass flow rate could be kept constant despite operating parameter perturbations within the system. To simulate a variation in density, the firing

frequency was varied within a reasonable range. Varying the frequency drives the fuel feed system to vary fuel pressure, similar to a change in density. To maintain safety the system was not tested while fuel was injected into the engine, but instead the fuel was routed into a bucket. Figure 40 shows the results of the validation tests. Since the overall goal of the system is to maintain a constant equivalence ratio, not just a constant fuel mass flow rate, the equivalence ratio is shown in Figure 40.

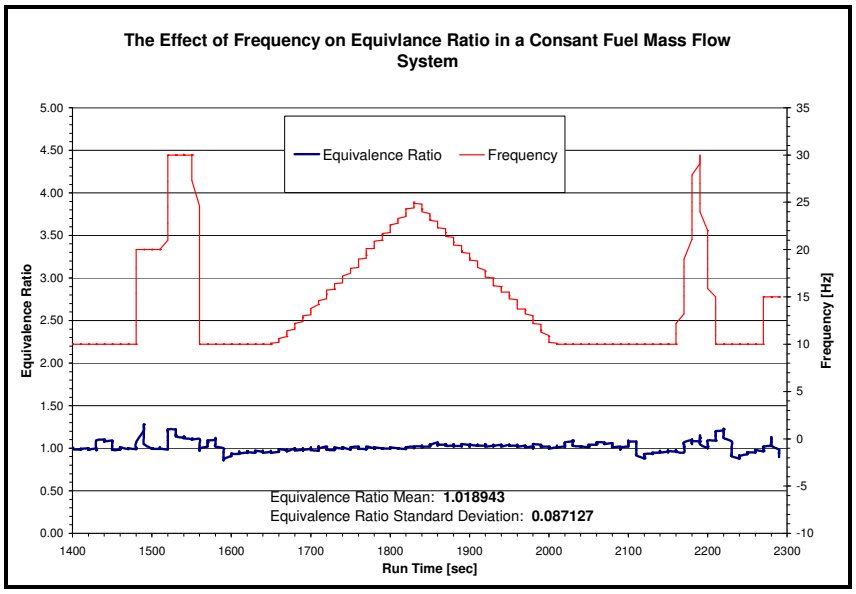

Figure 40. Results of constant fuel mass flow rate validation test

The frequency was varied using large step increases, moderate step increases, and gradual increases. Not surprisingly, the gradual increases produced the best results. This is fortunate, since the density drop seen during testing is gradual in nature. The system kept the equivalence ratio within the ignition limits of most low vapor pressure hydrocarbons for the entire test. The mean equivalence ratio over the test was found to

be 1.019 and the standard deviation of the equivalence ratio was found to be 0.087. Both of these values are acceptable for use during this research.

Fuel Heating System Performance

The fuel heating system used in this research is very similar to systems that were previously used, but enough changes were made to necessitate an examination of performance. The new heat exchanger design and the fuel heating system setup were discussed in Chapter III. The new fuel heating system is also compared to previous systems.

In previous research, only one heat exchanger was used to provide heated fuel to the engine. However, during this research two heat exchangers were used to heat the fuel. Figure 41 is a comparison of the rate at which the fuel injection temperature is increased from 366.5 K (200 ˚F) to 755.4 K (900 ˚F) with the single and dual heat exchanger system using identical operating parameters, and JP-8 as the fuel.

The dual heat exchanger system was expected to heat the fuel to all temperatures faster than the single heat exchanger system. This was not the case. Both heat exchanger systems heated the fuel at nearly the same rate until just over 610 K (638 ˚F). Above 610 K (638 ˚F) the performance of the two systems diverges, and the dual heat exchanger system heats the fuel much faster than the single heat exchanger system. It is interesting to point out that the two systems perform nearly identical until well above the flash vaporization temperature of JP-8, 530 K (494.3 ˚F). Therefore, if the flash vaporization of fuel is found to be the only benefit of heating the fuel, then only one heat exchanger is necessary.

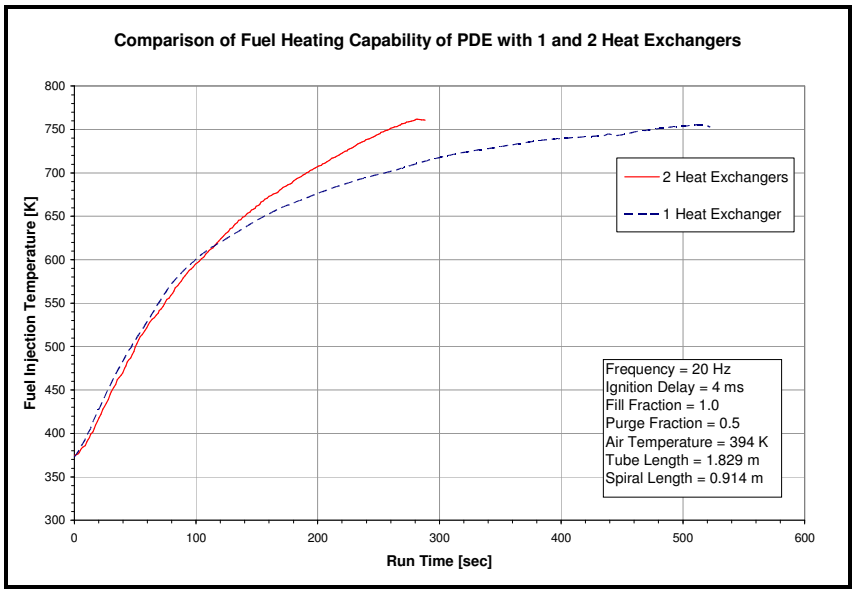

Figure 41. Comparison of fuel heating system with one and two heat exchangers using a JP-8/ air mixture with a frequency of 20 Hz and an ignition delay of 4 msec

Data was taken on both tube one and tube four during experimentation. In theory, the two tubes should produce identical results. In reality that is not always true. Three primary reasons that the tubes might produce different results are the slight difference in mixing length, the dissimilar wear on the injection valves, and the small variations in equivalence ratio. Therefore, it was necessary to determine whether the data gathered using the two tubes could be combined to draw conclusions on the PDE performance. The data for tubes one and four was analyzed and compared against each other. Figure 42 is a comparison of ignition time and DDT time for tubes one and four.

The percent difference between tubes one and four is below 7% for the entire temperature range for both ignition time and DDT time. The difference between the tubes is within the experimental error. Figure 43 is a comparison of the detonation distance for tubes one and four. The percent differences are all below 8% for the entire temperature range for detonation distance. Again, the differences between the two tubes

are within the error of the experiment. These differences are acceptable based on the accuracy of the data (see Chapter IV).

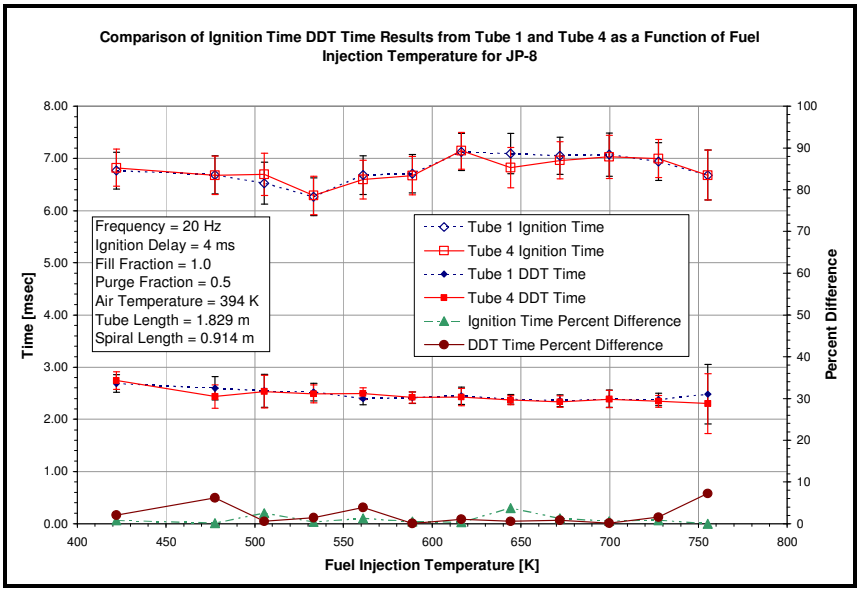

Figure 42. Comparison of ignition time and DDT time data gathered simultaneously from tubes one and four with JP-8 as the fuel with a frequency of 20 Hz and an ignition delay of 4 msec

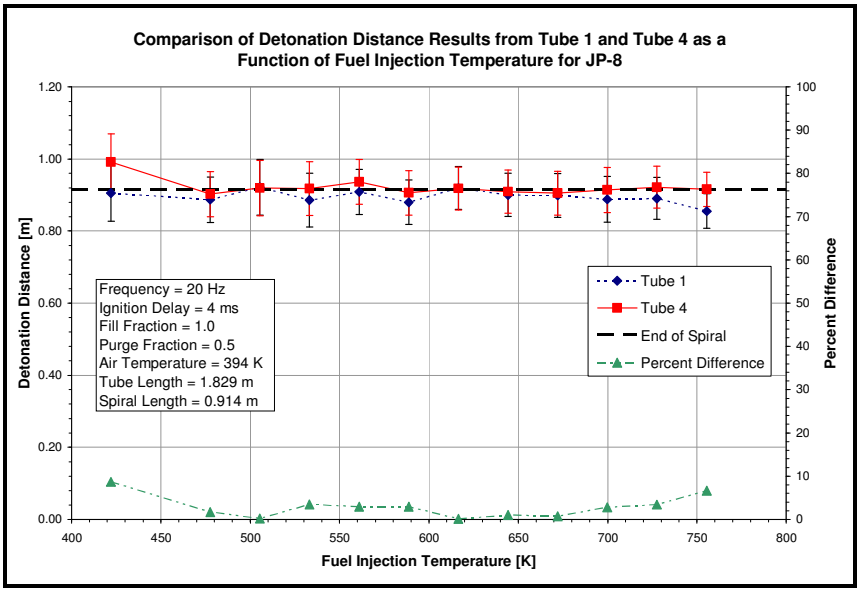

Figure 43. Comparison of detonation distance data gathered simultaneously on tubes one and four with JP-8 as the fuel with a frequency of 20 Hz and an ignition delay of 4 msec

To demonstrate the potential of the current fuel heating system for increasing fuel injection temperatures to the point where endothermic reactions occur, JP-8 was heated to the temperature and pressure limits of the heat exchangers. Figure 44 is a plot of the temperatures at the inlet to the heat exchangers, exit of the heat exchangers, and injection to fill air manifold along with the fuel/air mixture temperature during this test. The fuel temperature at the exit of the heat exchangers exceeded 860 K (1088 ˚F). The fuel heating system had the capacity to further heat the fuel, but the test was ended because the maximum pressure limit of the heat exchangers was reached. Reaching fuel temperatures of 860 K (1088 ˚F) is promising because endothermic reactions are quite prevalent at temperatures above 810.9 K (1000 ˚F). It should also be noted that even though the fuel injection temperature increased from 422 to 860 K (300 to 1088 ˚F), the fuel/air mixture temperature only increased from 394 to 446 K (250 to 344 ˚F).

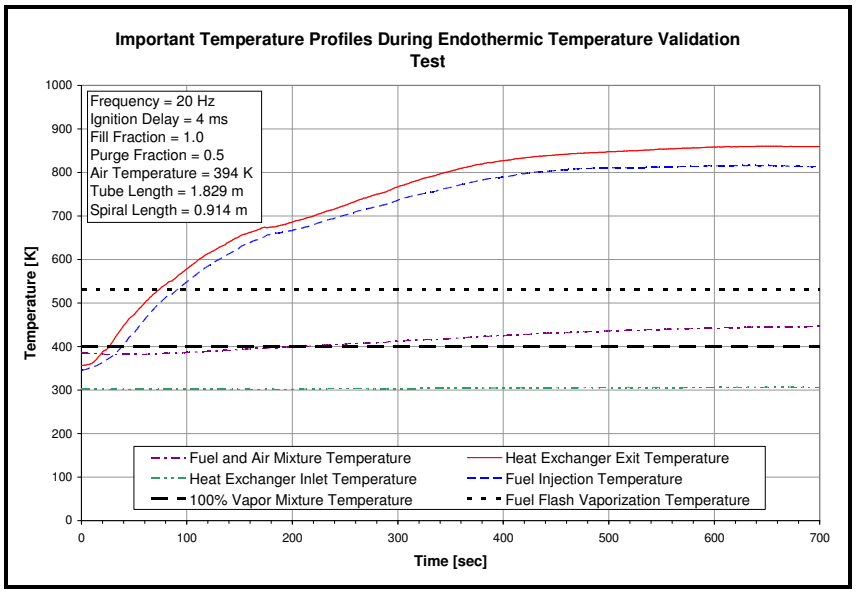

Figure 44. Temperature profiles from endothermic JP-8 validation test

Wavespeed

One of the most important parameters during the fire phase of the PDE cycle is the wavespeed. As mentioned earlier, the wavespeed is used to determine the DDT time, detonation distance, and detonation percentage. Therefore, the effect of increasing the fuel injection temperature on the wavespeed was examined. Figure 45 is a plot of the wavespeed of a stoichiometric JP-8/air mixture along the axial length of the detonation tube for several different fuel injection temperatures.

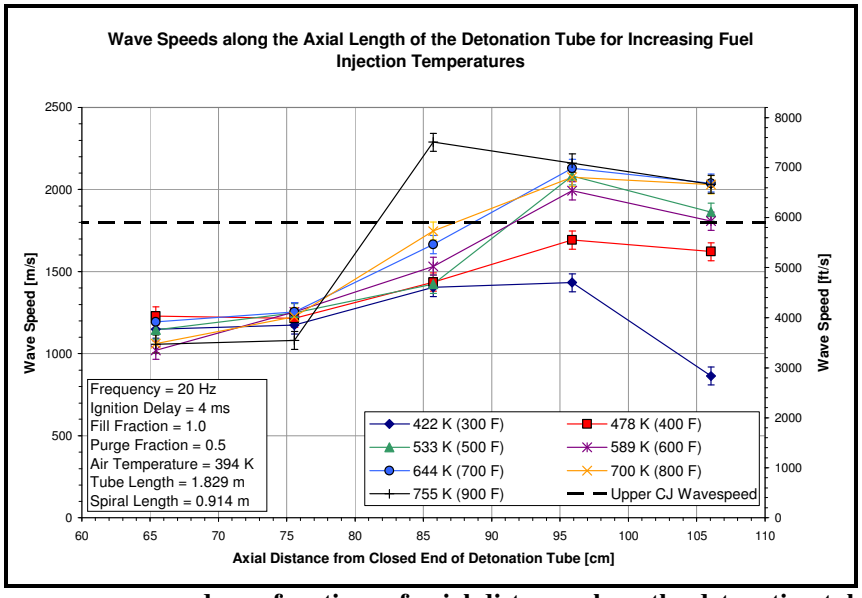

Figure 45. Average wavespeed as a functions of axial distance along the detonation tube of PDE for several fuel injection temperatures with a stoichiometric JP-8/air mixture with a frequency of 20 Hz and an ignition delay of 4 msec

Figure 45 displays several key issues that should be addressed. The first is that the upper C-J wavespeed is not reached when operating the PDE with a fuel injection temperature below 533 K (500 ˚F). This is important, because the flash vaporization temperature of JP-8 is between 533 and 561 K (500 and 550 ˚F). Hence, one benefit of

flash vaporization is demonstrated. According to Figure 45, detonation occurs before 95.885 cm (37.75 in) at wavespeeds between 533 and 700 K (500 and 800 ˚F). Above 700 K (800 ˚F), detonation occurs prior to 85.725 cm (33.75 in). This leads to speculation that the detonation distance should decrease by approximately 10 cm (4 in) as the temperature is increased from 422 to 755 K (300 to 900 ˚F). The final trend displayed in Figure 45 is that the wavespeed increases as the fuel injection temperature is increased. This trend was seen at nearly every axial position.

Fuels Study

Six fuels (JP-8, JP-7, JP-10, JP-900, RP-1, and S-8) were tested to determine how each affected the cycle performance of a PDE as the fuel injection temperature was increased. There were two main objectives of this study:

- Prove that all six fuels could be successfully used in a PDE.
- Compare the performance of the six fuels analyzed.

This section contains a comparison of the performance of the PDE with all six fuels. A more detailed analysis of each fuel, that includes confidence intervals and discussion of each performance parameter, is included in Appendix A. The fuels were examined over a temperature range of 422 to 755 K (300 to 900 ˚F).

While the fuel injection temperature was increased from 422 to 755 K (300 to 900 ˚F), the fuel/air mixture temperature was elevated on a much lower scale. Figure 46 is a plot of the resultant fuel/air mixture temperatures as a function of fuel injection temperature for all six fuels. For an increase of fuel injection temperature from 422 to

755 K (300 to 900 ˚F), the fuel/air mixture temperature increases form 394 to 415 K (250 to 287 ˚F).

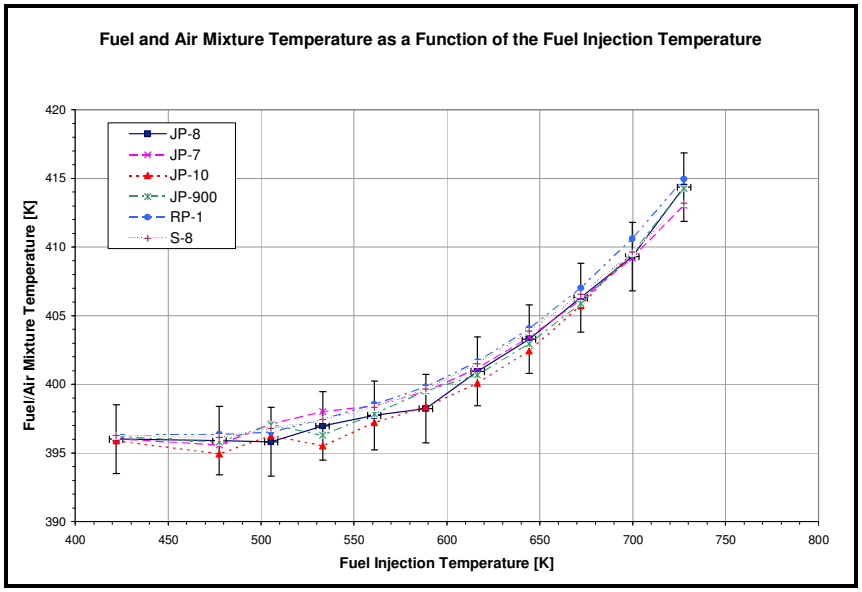

Figure 46. Resultant fuel/air mixture temperature as a function of fuel injection temperature with a frequency of 20 Hz and an ignition delay of 4 msec

It is interesting to note the shape of the mixture temperature curve in Figure 46. The curve is not a straight line as might be expected, but instead the rate of increase of the fuel/air mixture temperature increases with increasing fuel injection temperature. This is due to a combination of heating the fill air manifold and an increase in mixing at higher temperatures. The six fuels produce identical fuel/air mixture temperatures for given fuel injection temperatures. Therefore, the fuels can be compared without the any bias as a result of mixture heating effects.

Figure 47 is a plot of the mean and standard deviation of ignition time as a function fuel injection temperature for all six fuels. No differentiation amongst the fuels can be made. JP-8 has a noticeably higher ignition time in the range of 586 to 755 K

(600 to 900 ˚F). The probable cause of this trend is detailed in the next paragraph. In addition, S-8 produced the lowest ignitions for almost the entire temperature range. JP-7, JP-900, and RP-1 demonstrate almost no difference in trend or magnitude, which was expected due the similarity of the fuels. With the exception of JP-8, ignition times for all fuels are independent of fuel injection temperature in the temperature range examined, as expected based on global reaction theory. There is also virtually no stratification amongst the standard deviations of the six fuels.

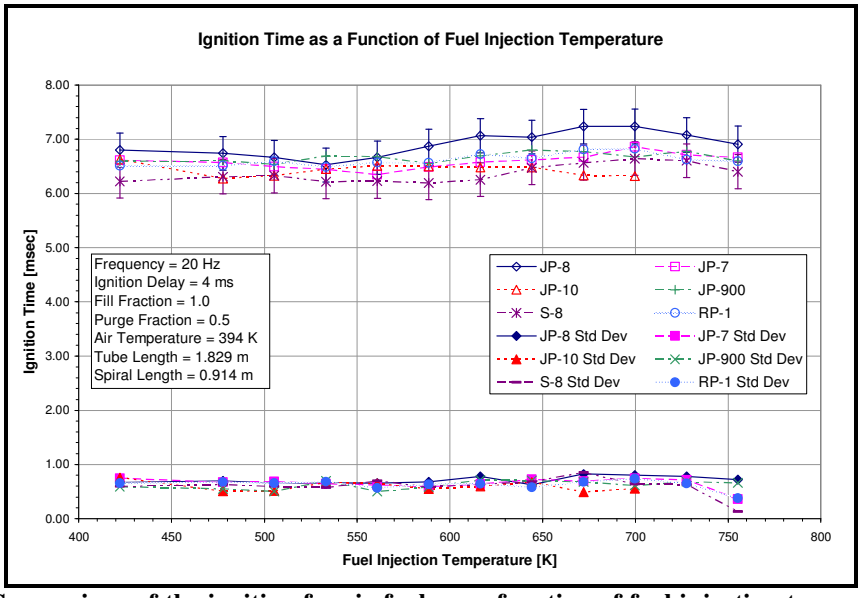

Figure 47. Comparison of the ignition for six fuels as a function of fuel injection temperature with a frequency of 20 Hz and an ignition delay of 4 msec

An unexpected trend, noted earlier, is identified for JP-8. The ignition time appears to decrease initially with increasing fuel injection temperature. A minimum ignition time of 6.53 msec is noted at 533 K (500 ˚F). At approximately the flash vaporization temperature, the ignition time begins to increase with an increase in fuel injection temperature. A maximum ignition time of 7.24 ± .292 msec is noted at 700 K

(800 ˚F). Finally, at approximately the supercritical temperature, the ignition time begins to decrease again with increasing fuel injection temperature. While this trend only occurs over a span of 0.8 msec, it is still significant. This phenomenon is not completely understood, but an educated hypothesis can be formed. The initial decrease in ignition time is a consequence of the local equivalence ratio converging with unity. The ensuing increase in ignition time is an effect of the thermal degradation that occurs within JP-8, causing degradation in performance. The final decline in ignition time is a result of the initial endothermic reactions occurring in the fuel. It is interesting to note that all of the fuels exhibit an ignition time trend similar to JP-8, but the magnitude of fluctuation for the other fuels is within the experimental error.

It was found that detonation of a JP-10/air mixture was very difficult with the current setup. Do to the lack of detonations, the DDT time and detonation distance data for JP-10 was heavily scattered. The atrocious precision of the JP-10 detonation data renders the DDT time and detonation location results for JP-10 unusable. Therefore, the DDT time and detonation distance results for JP-10 have been omitted. The DDT time for the other five fuels is displayed in Figure 48 as a function of fuel injection temperature.

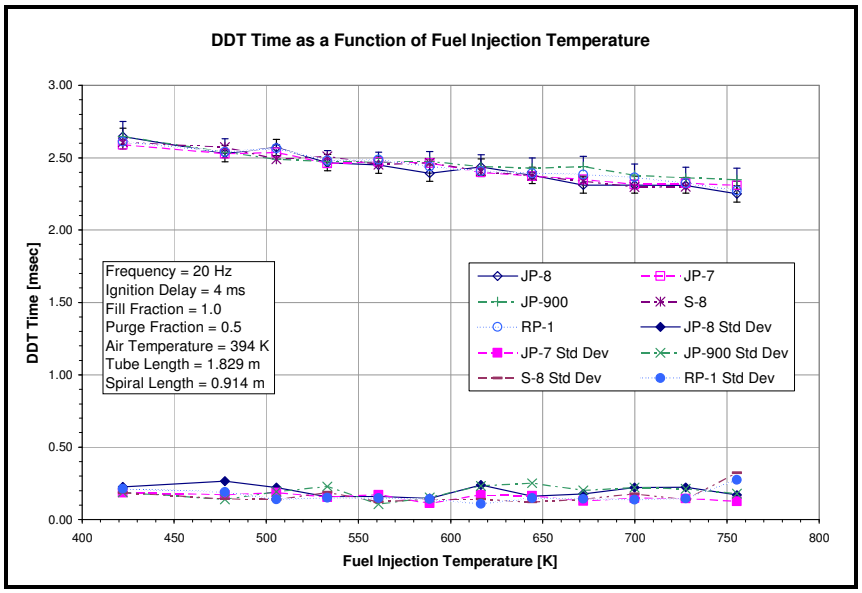

Figure 48. Comparison of the DDT time for five fuels as a function of fuel injection temperature with a frequency of 20 Hz and an ignition delay of 4 msec

No stratification is seen for either the mean or standard deviation of DDT time. The difference between any two fuels is within the experimental error for the entire temperature range. All five fuels are inversely related to fuel injection temperature, as expected. A nearly linear trend is shown for each fuel with approximately a 15% decrease in DDT time over the temperature range. The standard deviation of the DDT time is independent of fuel injection temperature.

The next parameter analyzed was the detonation distance. The detonation distance as a function of fuel injection temperature for all fuels other than JP-10 is shown in Figure 49. As expected, the detonation distance of all five fuels demonstrates an inverse relationship with fuel injection temperature. Below 644 K (700 ˚F) the detonation distance of the five fuels differs in both magnitude and slope, but above 644 K (700 ˚F) the fuels produce identical detonation distances.

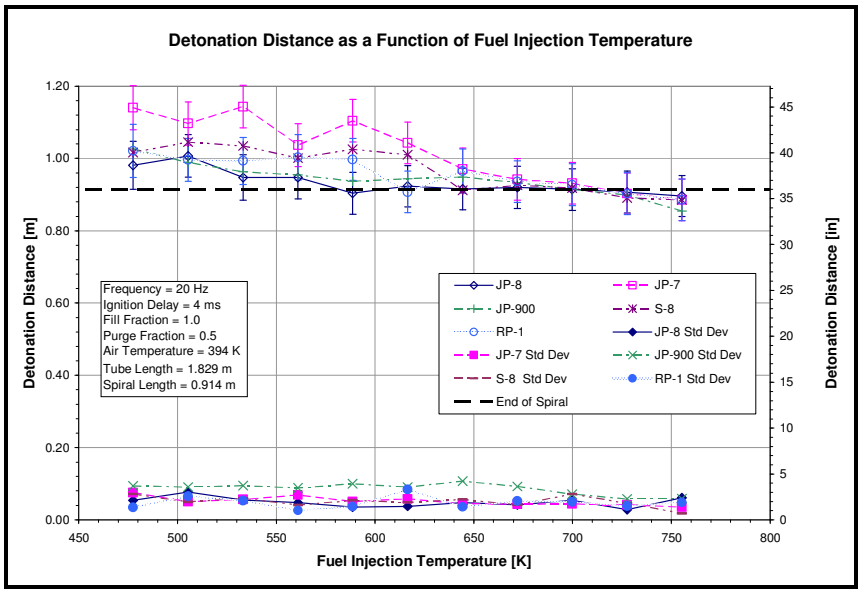

Figure 49. Comparison of the detonation distance for five fuels as a function of fuel injection temperature with a frequency of 20 Hz and an ignition delay of 4 msec

The fuels show significant stratification below 644 K (700 ˚F). JP-8 has the lowest detonation distances, followed closely by JP-900. JP-7 performs the poorest above 644 K (700 ˚F), with a maximum value of 1.14 m (44.9 in). RP-1 and S-8 perform very similarly, both with detonation distance between JP-7 and JP-900. Once the individual fuels reach flash vaporization temperatures, detonations occur very close to the end of the spiral. The standard deviation of the detonation distance is independent of fuel injection temperature for all fuels, but JP-900 has a slightly higher standard deviation than the other four fuels. The detonation distance of JP-8 showed a decrease of 11 cm (4.33 in), which is within 1 cm of what was predicted based on examination of the wavespeed trends in Figure 45.

The final parameters examined were the detonation percentage and 1400 m/s wavespeed percentage. The 1400 m/s wavespeed percentage is shown in Figure 50 as a function of fuel injection temperature. As stated earlier, the 1400 m/s wavespeed

percentage is the percentage of ignitions that result in a combustion wavespeed of 1400 m/s or greater.

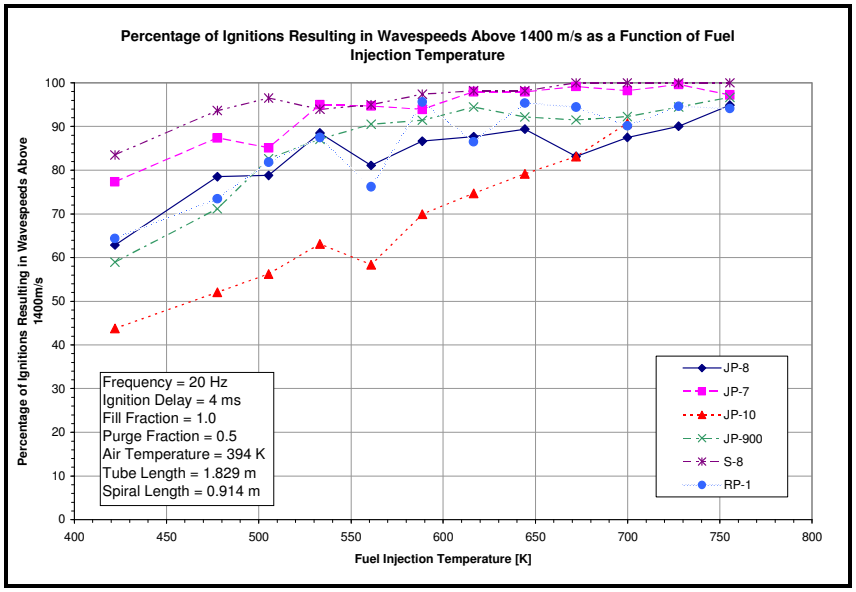

Figure 50. Comparison of the percentage of ignitions that result in wavespeeds above 1400 m/s for six fuels as a function of fuel injection temperature with a frequency of 20 Hz and an ignition delay of 4 msec

All six fuels show a significant increase in 1400 m/s wavespeed percentage as fuel injection temperature increases. Figure 50 shows an approximately 20 to 30% increase in 1400 m/s wavespeed percentage for all fuels. All fuels reach a 1400 m/s wavespeed percentage above 90% at the highest temperatures. JP-10 stands out as the fuel with the lowest 1400 m/s wavespeed percentage for the majority of the temperature range. The detonation percentage is shown in Figure 51 as a function of fuel injection temperature. Again, the detonation percentage is the percentage of ignitions that result in a combustion wavespeed of 1800 m/s or greater.

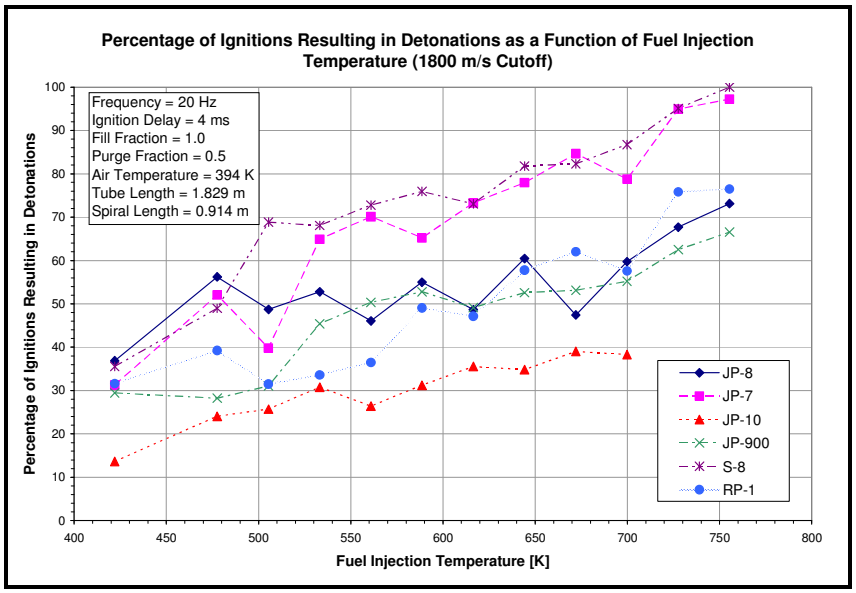

Figure 51. Comparison of the detonation percentage for six fuels as a function of fuel injection temperature with a frequency of 20 Hz and an ignition delay of 4 msec

All fuels demonstrate a strong trend of increasing detonation percentage for an increase in fuel injection temperature. Examining both Figure 50 and Figure 51, JP-7 and S-8 stand out as the fuels that produce the largest percentage of detonations. The fuels can be lumped into three categories, based on Figure 50 and Figure 51. The first group, JP-7 and S-8, demonstrate remarkable increases in detonations as fuel injection temperature increases. Both JP-7 and S-8 provide nearly 100% detonations at 755 K (900 ˚F). JP-8, JP-900, and RP-1 make up the second category; they all demonstrate very similar trends for both the detonation and 1400 m/s wavespeed percentages. JP-8, JP-900, and RP-1 produce detonation percentages between 65 and 75% at a fuel injection temperature of 755 K (900 ˚F). The final category includes only JP-10. While JP-10 demonstrates an increase in detonation percentage and 1400 m/s wavespeed percentage as fuel injection temperature is increased, the magnitude of the detonation percentage remains undesirable. The detonation percentage of JP-10 increases from 14 to only 38%.

These meager detonation percentages led to the large uncertainty in DDT time and detonation distance data for JP-10/air mixtures.

Table 10 is a summary of the important values determined during the fuels study. While these values are taken directly from Figure 47 through Figure 51, the table was added for quick reference. Since the ignition time was shown to be constant for all fuel other than JP-8, an average value is presented in Table 10. DDT time, detonation distance, and detonation percentage all demonstrated nearly linear relationships with fuel injection temperature; therefore, the maximum and minimum values are presented in Table 10.

Table 10. Summary of important performance parameter values determined during fuels study

Fuel	Average Ignition Time [msec]	Maximum DDT Time [msec]	Minimum DDT Time [msec]	Maximum Detonation Distance [m]	Minimum Detonation Distance [m]	Maximum Detonation Percentage	Minimum Detonation Percentage
JP-8	6.90	2.65	2.25	1.00	0.90	36.9	73.1
JP-7	6.59	2.59	2.31	1.14	0.89	31.3	97.2
JP-10	6.43	N/A	N/A	N/A	N/A	13.6	38.3
JP-900	6.63	2.65	2.35	1.03	0.85	29.5	66.5
RP-1	6.62	2.61	2.27	1.02	0.89	31.6	76.5
S-8	6.37	2.61	2.26	1.02	0.89	35.5	100.0

Internal Spiral Length

A qualitative analysis of internal spiral length was performed to determine the minimum spiral length that could produce consistent strong detonations with a JP-8/air mixture. It is advantageous to use the shortest spiral possible in a PDE detonation tube. It has been demonstrated that as the length of a spiral is decreased the thrust produced by the PDE is increased (Hoke, 2005:4-5). All previous heated JP-8 research was conducted using a 1.22 m (48 in) spiral. Only one test was performed with the 1.22 m (48 in) spiral

to determine detonation distance. The only data point calculated during the one test was at 647 K (705 ˚F), where the detonation distance was found to be 1.09 m (42.89 in). As shown in Figure 49, the detonation distance of a JP-8/air mixture only varies by 0.10 m (3.93 in) for a fuel injection temperature range of 422 to 755 K (300 to 900 ˚F). The 0.91 m (36 in) spiral JP-8 tests, shown in the previous section, produced detonation distances that decrease from 1.00 to 0.90 m (39.4 to 35.4 in). Since the detonation distance produced with a 1.22 m (48 in) spiral is larger than that produced by the 0.91 m (36 in) spiral, it was hypothesized that the presence of an excessively long spiral section actually prohibited the culmination of the deflagration to detonation transition. To test this, a 0.76 m (30 in) spiral was tested in exactly the same setup as the used in the fuels studies. The 0.76 m (30 in) spiral proved to be insufficient to produce consistent detonations. It was then concluded that 0.91 m (36 in) is the minimum spiral length that can be used with a JP-8/air mixture. According to Hoke, a reduction in spiral length from 1.22 m (48 in) to 0.91 m (36 in) will result in a thrust increase of over 10% (Hoke, 2005:5)

Purge Fraction

A qualitative analysis was performed to determine the lowest purge fraction that could be safely used on a JP-8 fueled PDE. For most PDE research, the purge phase is the same duration as the fill and fire phases, but this may not be the case in operational engines. Therefore, it is advantageous to use the smallest purge fraction, because that will lead to the minimum duration of the purge phase. Decreasing the length of the purge phase will allow more time for other phases or permit an increase in frequency.

For a purge fraction to be considered safe, the PDE must be able to begin and sustain operation with no backfiring or detriment to performance. To determine the minimum purge fraction, the purge fraction was set at 0.0 and an attempt was made to start up the PDE. The tests using a purge fraction of 0.0 resulted in immediate backfires, so trials with a purge fraction of 0.1 were completed. Again, constant backfiring occurred. During the 0.2 purge fraction trials, backfiring during startup occurred approximately 50% of the time. The 0.3 purge fraction trials resulted in consistent and safe operation of the PDE, therefore 0.3 was determined to be the minimum purge fraction for use with a JP-8/air mixture in a PDE. A reduction in purge fraction from 0.5 to 0.3 results in a 40% decrease in time required for the purge phase.

Ignition Delay

As discussed in Chapter II, an ignition delay can increase the performance of a PDE. To determine the effect of varying ignition delay, a series of tests were performed for varying ignition delays. All ignition delay testing was performed with JP-8 as the fuel. Do to the time constraints of the fire phase, a frequency of 15 Hz was used for all ignition delay testing. By selecting a frequency of 15 Hz, ignition delays of up to 10 msec could be tested safely. Ignition delays of 0, 2, 4, 6, 8 and 10 msec were examined. The 0 msec ignition delay case resulted in constant backfiring of the PDE, therefore no data was taken.

Figure 52 is a plot of the ignition time as a function of fuel injection temperature for a JP-8/air mixture with ignition delays ranging from 2 to 10 msec. With the exception of the 2 msec ignition delay case, there is no significant stratification, especially at low

temperatures. The 2 msec ignition delay results demonstrate significantly higher ignition times for all temperatures as compared to the other ignition delays, as expected based on global reaction theory. The 4 msec case produces slightly higher ignition times at low temperatures, but lower ignition delays at higher temperature. The ignition delays between 6 and 10 msec do not show significant stratification amongst each other. It should be noted that the difference between the 4 msec case and the higher ignition delay cases is within the experimental error at temperatures below 589 K (600 ˚F).

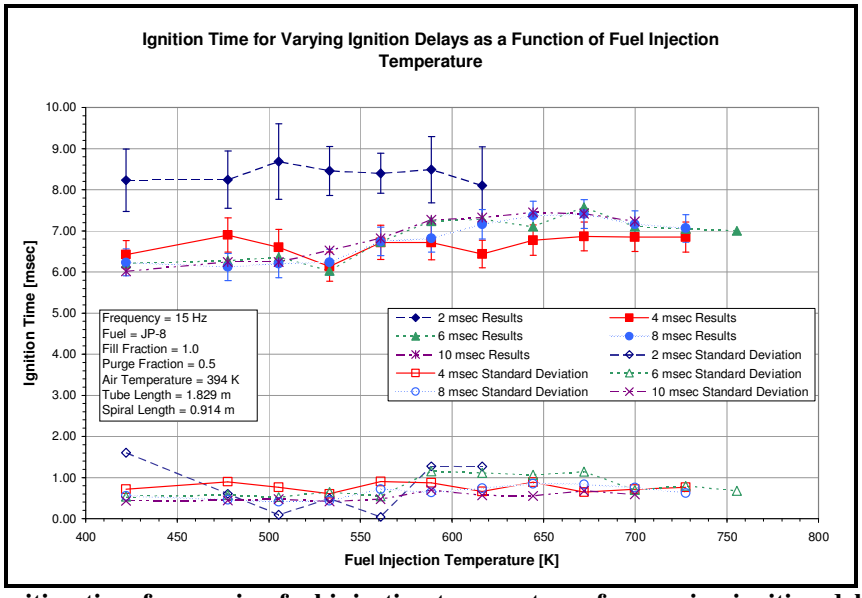

Figure 52. Ignition time for varying fuel injection temperatures for varying ignition delays for a JP-8/air mixture with a frequency of 15 Hz

The ignition time for each ignition delay at 422 K (300 ˚F) can be used to determine the accuracy of the global reaction theory at low fuel injection temperatures. The global reaction theory approximation (discussed in Chapter II) for normalized ignition time as a function of average head pressure is shown in Figure 53. Along with the global reaction theory approximation, the experimentally determined normalized

ignition time as a function head pressure is displayed in Figure 53. The experimentally determined ignition times at 422 K (300 °F) are taken from Figure 52 as a function of ignition delay. The ignition delay corresponds to an average head pressure, from Table 4. The ignition times were normalized by the ignition time corresponding to an ignition delay of 6 msec, because the average head pressure of the 6 msec case is within 1% of ambient pressure.

Figure 53 shows that the experimental results compare well with global reaction theory. The global reaction theory approximation is within the experimental uncertainty of the experimental mean. This is an analysis of global reaction theory only at a fuel injection temperature of 422 K (300 °F). No conclusion is made about the validity of global reaction theory at very high fuel injection temperatures.

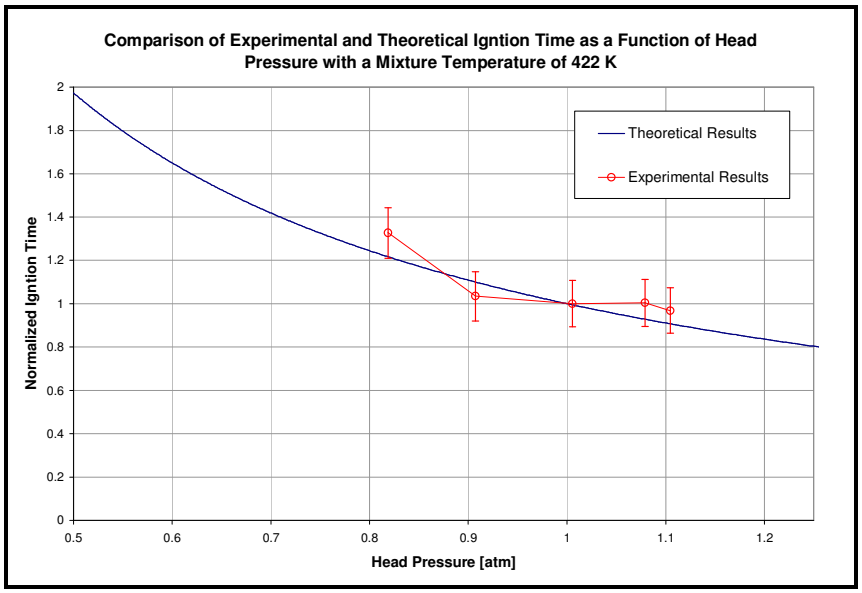

Figure 53. Comparison of experimental and theoretical ignition time as a function of head pressure for a JP-8/air mixture

Figure 54 is a plot of the DDT time for a JP-8/air mixture as a function of fuel injection temperature for various ignition delays. The 2 msec ignition delay trials resulted in sporadic and meager detonations, leading to extremely poor confidence in results. Therefore, the DDT time and detonation distance data is not presented. All other ignition delays demonstrate the same trend, where increasing fuel injection temperature leads to decreasing DDT time. It is also apparent that increasing the ignition delay will reduce the DDT time. The DDT time was expected to decrease with increasing head pressure, based on the light hydrocarbon/air detonation data (shown in Chapter II). The standard deviation of the DDT time is similar for all ignition delays.

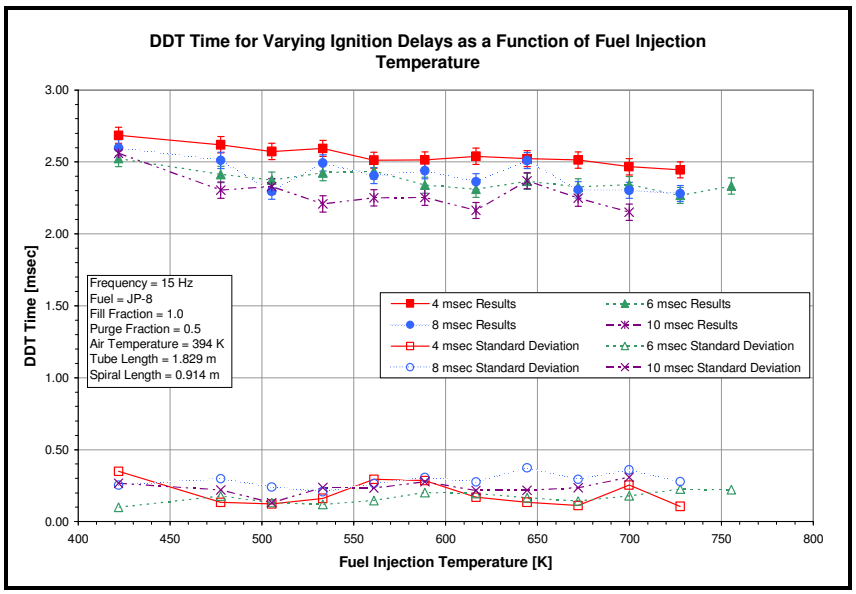

Figure 54. DDT time for a JP-8/air mixture as a function of fuel injection temperature for varying ignition delays with a frequency of 15 Hz

To compare the overall effect of varying ignition delays in a PDE, the total time to detonation is plotted as a function of fuel injection temperature for various ignition delays in Figure 55. The total time to detonation is the sum of the ignition delay, ignition

time, and DDT time. The reduction in ignition time and DDT time as ignition delay is increased is overshadowed by the increase in ignition delay. Therefore, an ignition delay of 4 msec produces the total time to detonation, and an ignition delay of 10 msec produces the highest total time to detonation.

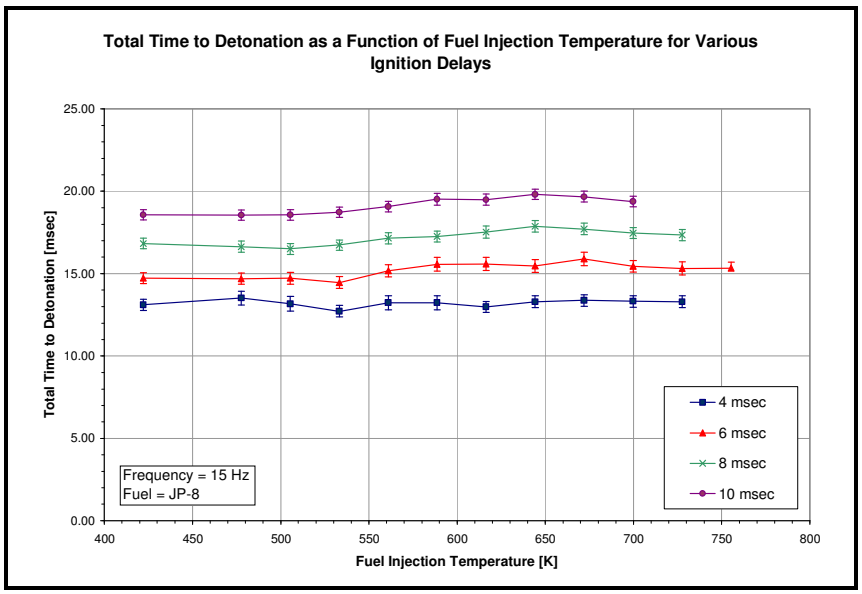

Figure 55. Total time to detonation for a JP-8/ari mixture as a function of fuel injection temperature for various ignition delays with a frequency of 15 Hz

Figure 56 is a plot of the detonation distance of a JP-8/air mixture as a function of fuel injection temperature for various ignition delays. The four ignition delays all show an inverse relationship with fuel injection temperature. The 4 msec ignition delay case stands out with the lowest detonation distance for all fuel injection temperatures; although, the difference between the 4 msec ignition delay and the higher ignition delays is within the experimental error. The other three ignition delays are nearly identical, especially at the lower temperatures. The standard deviation of the detonation distance is fairly constant for the four ignition delays.

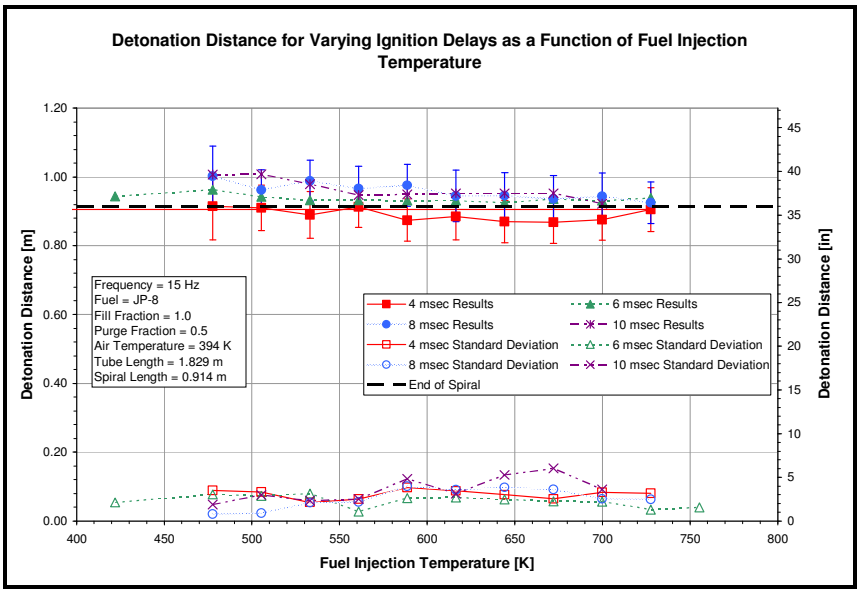

Figure 56. Detonation distance for a JP-8/air mixture as a function of fuel injection temperature for varying ignition delays with a frequency of 15 Hz

The 1400 m/s wavespeed percentage for varying ignition delays is displayed in Figure 57 as a function of fuel injection temperature. The fuel injection temperature did not strongly influence the 1400 m/s wavespeed percentage in any fuel. The 1400 m/s wavespeed percentage for the 10 msec ignition delay is clearly the lowest. The 4, 6, and 8 msec ignition delays produced 1400 m/s wavespeed percentages above 80% at all temperatures above 422 K (300 °F).

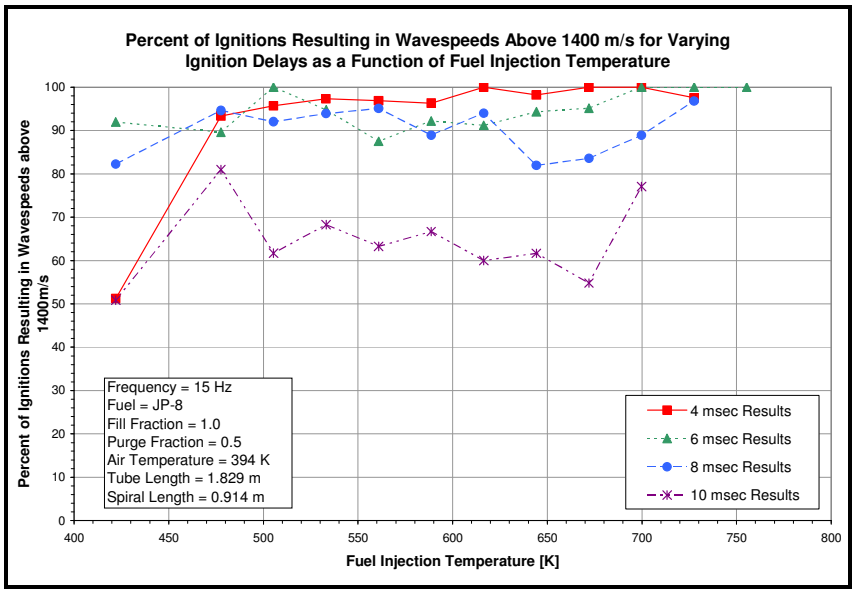

Figure 57. Percent of ignition resulting in a wavespeed above 1400 m/s for varying ignition delays as a function of fuel injection temperature with a frequency of 15 Hz

The relationship between detonation percentage and ignition delay is much more evident (Figure 58). The detonation percentage is significantly impacted by the ignition delay. The detonation percentage increases steadily as the ignition delay decreases. The 10 msec ignition delay results in detonation percentages ranging from 13.3 to 37.7%, while the ignition delay for the 4 msec case increases from 33.3 to 95.0%. In fact, the detonation percentage for the 4 msec ignition delay is near 90% for all fuel injection temperatures above 505 K (450 °F).

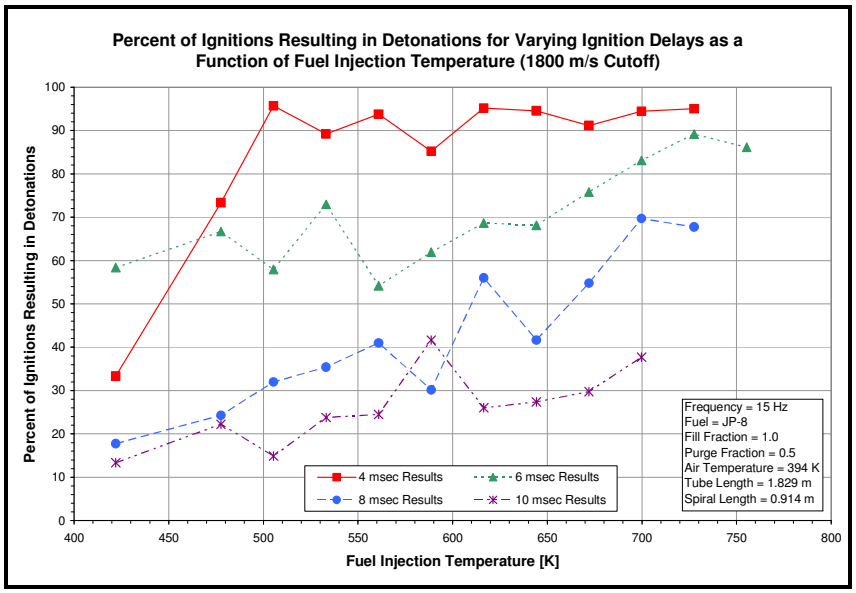

Figure 58. Detonation percentage as a function of fuel injection temperature for various ignition delays using a JP-8/air mixture with a frequency of 15 Hz

Frequency

The motivation to decrease ignition time and DDT time is to decrease the fire phase time, thus decreasing the PDE cycle time. If the cycle time is decreased then the PDE firing frequency can be increased, thereby increasing thrust. This rationale hinges on the assumption that increasing the frequency will not produce any adverse effects on PDE cycle performance. To demonstrate that increasing the frequency will not hinder PDE performance, a study was conducted with three frequencies. Frequencies of 10 Hz, 15 Hz, and 20 Hz were tested to determine the ignition time, DDT time, detonation distance. Frequencies above 20 Hz are not possible at this time due to limitations of the length of the fire cycle. A system operating at 25 Hz allows only 13.3 msec to be spent on the fire cycle; this time limit is too short for the detonation of a JP-8/air mixture. The 10 Hz frequency did not provide enough energy to the system to afford fuel injections temperatures above 644 K (700 ˚F). The inability to heat the fuel to adequate

temperatures using a frequency of 10 Hz prohibited proper comparison with other frequencies, therefore the 10 Hz results have been omitted.

Figure 59 is a plot of ignition time as a function of fuel injection temperature for a PDE operating at 15 Hz and 20 Hz. The frequencies show nearly identical ignition times for the entire temperature range. The difference between the results using the two frequencies is within the experimental error. The standard deviation of the ignition time is also consistent between the two frequencies.

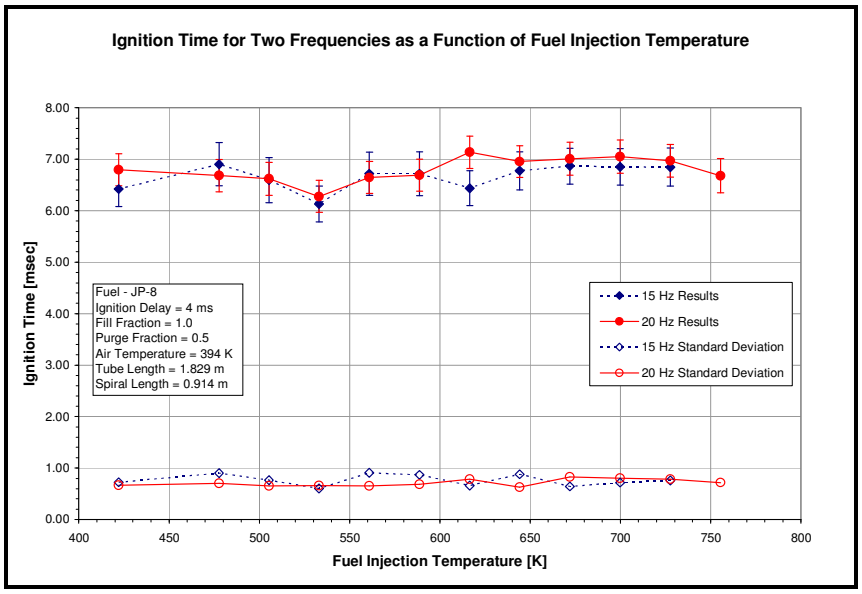

Figure 59. Comparison of ignition time for two frequencies as a function of fuel injection temperature with a JP-8/air mixture with an ignition delay of 4 msec

Figure 60 is a plot of DDT time as a function of fuel injection temperature for a PDE operating at 15 Hz and 20 Hz. The DDT time for the 20 Hz case is less than the DDT time for the 15 Hz case for the entire temperature range, especially at higher temperatures. The total time to detonation (sum of ignition time and DDT time) for the

20 Hz case is less than for the 15 Hz case. This demonstrates an improvement in performance with increasing frequency.

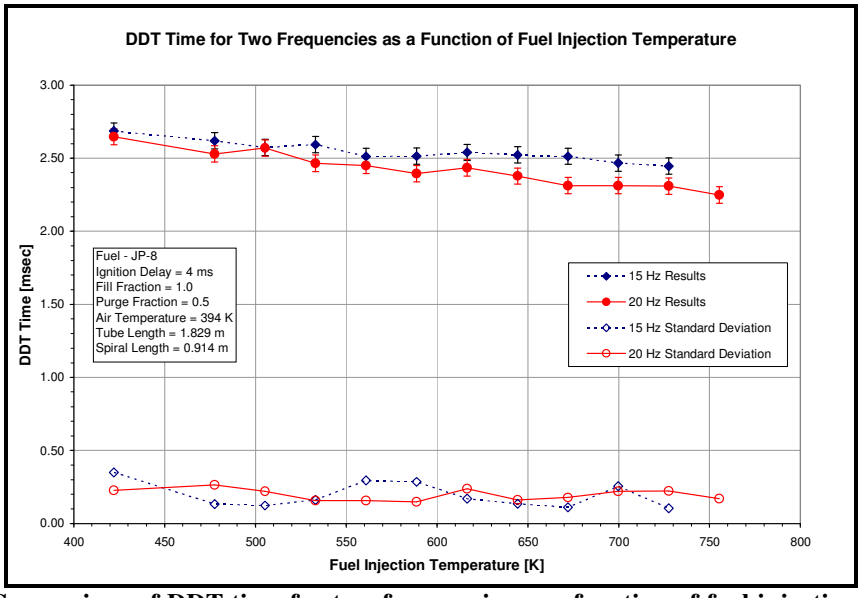

Figure 60. Comparison of DDT time for two frequencies as a function of fuel injection temperature with a JP-8/air mixture with an ignition delay of 4 msec

Figure 61 is a plot of the detonation distance as a function of fuel injection temperature with varying frequency. The difference between the detonation distance results of the 15 and 20 Hz tests are within the error for the entire temperature range. In addition, both frequencies result in detonations at the end of the internal spiral. Again, no degradation in performance is noticed when operating at 20 Hz as compared to at 15 Hz. Therefore, increasing the frequency was found to induce an increase in cycle performance.

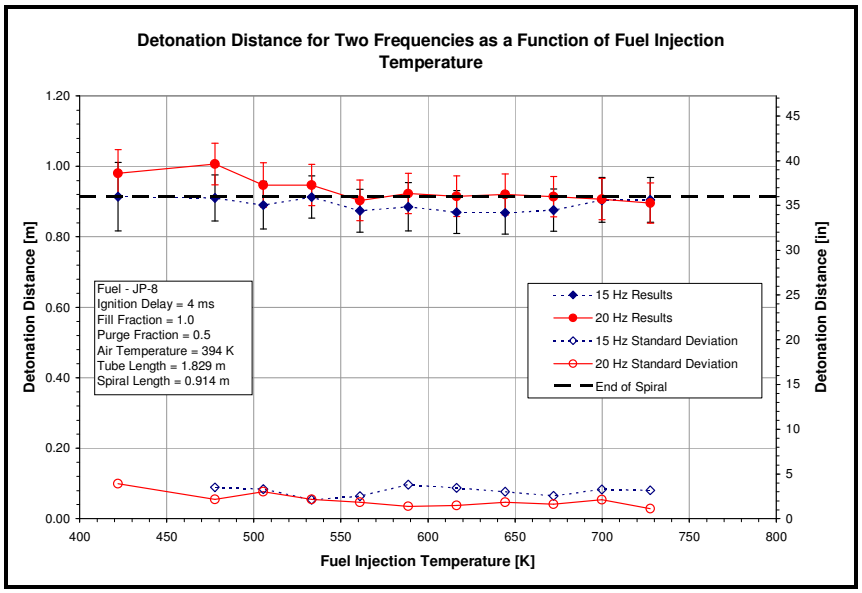

Figure 61. Comparison of detonation distance for two frequencies as a function of fuel injection temperature with a JP-8/air mixture with an ignition delay of 4 msec

Equivalence Ratio above Flash Vaporization Temperature

All previous JP-8 research with fuel injection temperatures below the flash vaporization point was performed with fuel rich mixtures with equivalence ratios of 1.05 or greater. Due to the presence of fuel droplets in the mixture, a globally rich mixture was necessary to provide a stoichiometric local equivalence ratio to the detonation tube. However, in a homogeneous mixture the local equivalence ratio is equal to the global equivalence ratio for fuel injection temperatures above the flash vaporization temperature. A test was performed to demonstrate that a flash vaporized JP-8/air mixture with an equivalence ratio of 1.00 would perform better than with an equivalence ratio of 1.05.

Figure 62 is a plot of the DDT time and ignition time as a function of fuel injection temperature (above the flash vaporization temperature) for a JP-8/air mixture with equivalence ratios of 1.05 and 1.00. The 1.00 equivalence ratio mixture produces lower ignition times and nearly equal DDT times as compared with the 1.05 equivalence

ratio mixture. The ignition time was expected to be lower for stoichiometric mixtures since ignition occurs easiest with stoichiometric mixtures. The decrease in ignition time and constant DDT time leads to a lower overall time to detonation.

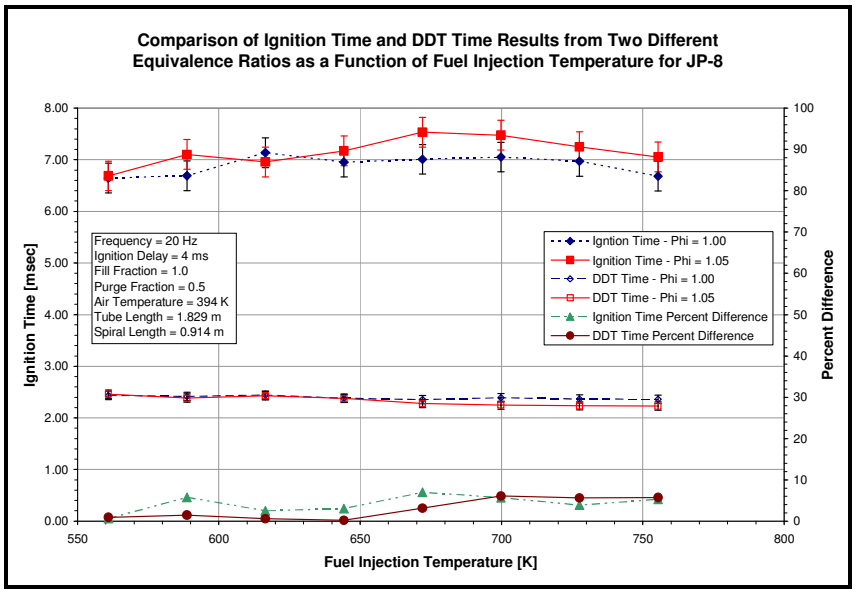

Figure 62. Comparison of ignition time and DDT time for two equivalence ratios as a function of fuel injection temperature for a JP-8/air mixture with a frequency of 20 Hz and an ignition delay of 4 msec

The detonation distances for a JP-8/air mixture with equivalence ratios of 1.00 and 1.05 are shown in as a function of fuel injection temperature (above the flash vaporization temperature). The detonation distances of the two equivalence ratios are nearly identical, with percent differences of less than 2% for the entire temperature range. Thus, with a lower time to detonation and identical detonation distance, an equivalence ratio of 1.00 performs better than 1.05. The stoichiometric mixture produces lower DDT times because the excess fuel in the 1.05 equivalence ratio mixture hinders detonation.

The main advantage of using a stoichiometric fuel/air mixture as opposed to an equivalence ratio of 1.05 is the reduction in fuel consumption.

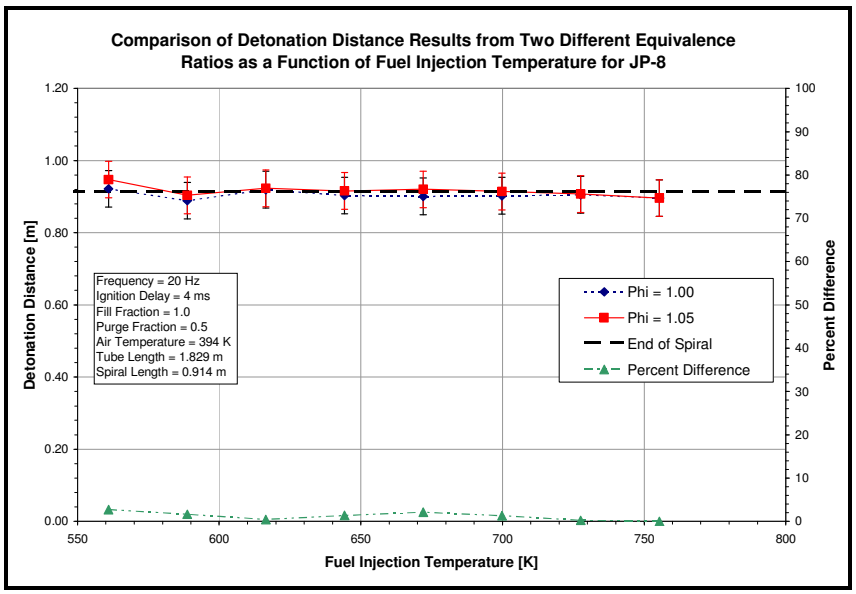

Figure 63. Comparison of detonation distance for two equivalence ratios as a function of fuel injection temperature for a JP-8/air mixture with a frequency of 20 Hz and an ignition delay of 4 msec

Heat Exchanger Fatigue Issues

The heat exchangers used in this research were designed and analyzed using simple solid mechanics, detailed in Appendix B. A *MATLAB* code was developed to analyze the final heat exchanger design (Appendix B). It was found that after several hours of testing, the heat exchangers would form cracks along the weld that attach the end plates to the inner tube. The cracks were the result of fatigue stresses in the weld material. Figure 64 contains photographs of the circumferential weld before testing as well as after the fatigue stresses caused failure in the weld. A 0.5 cm (0.197 in) gap formed between the two halves of the weld. Failure of this magnitude occurred three

times during the four months of testing performed for this research. Therefore, it will be necessary to investigate other heat exchanger designs if further research in this area is pursued.

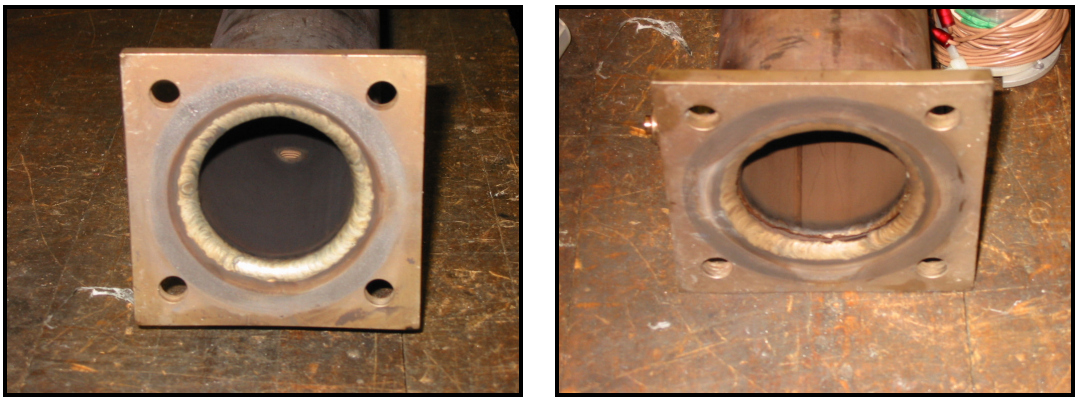

Figure 64. Photographs of the circumferential weld attaching the end plate to the inner tube on the heat exchanger before use (left) and after failure (right)

VI. Conclusions and Recommendations

Conclusions

This research marked the first analysis of the effect of increasing fuel injection temperature, up to 755 K (900 ˚F), on key pulse detonation engine performance parameters. This effort has identified certain limitations on detonation tube configuration, has provided an understanding of the pressure-temperature profile of the initial combustion event of the cycle, and for the first time has defined a measure of success rate for repetitive detonation cycles. In addition, a new constant fuel mass flow rate system was successfully developed and implemented.

Fuels Study

The effects of increasing fuel injection temperature on ignition time, DDT time, detonation distance, and detonation percentage for JP-8, JP-7, JP-10, JP-900, RP-1, and S-8 were determined. Ignition time was found to be virtually independent of fuel injection temperature for all fuels, except JP-8. JP-10 was found to produce undesirably low levels of detonations, compared to the other fuels. The DDT time of other five fuels demonstrated a nearly identical inverse relationship with fuel injection temperature; DDT time decreases linearly by approximately 15%. The detonation distance for all fuels, other than JP-10, linearly decreases with increasing fuel injection temperature. Above the flash vaporization temperature of the fuels, the detonation distance for all fuels is identical. The detonation percentage for all fuels increases considerably with increasing fuel injection temperature, with JP-7 and S-8 producing the most consistent detonations.

Based on this performance criteria; JP-8, JP-7, JP-900, RP-1, and S-8 can all be used efficiently to fuel a PDE with elevated fuel injection temperatures.

Ignition Delay

The ignition delay was found to have a small effect on all performance parameters for JP-8, although it was determined that operating the PDE with an ignition delay below 4 msec yields very poor performance. An ignition delay of 4 msec was found to be superior to the other ignition delays studied for JP-8, based on total time to detonation and detonation percentage. The global reaction theory was shown to provide reasonable approximations for the effect of head pressure on ignition time.

Spiral length, Purge Fraction, Frequency, and Equivalence Ratio

The spiral length, purge fraction, frequency, and equivalence ratio were examined for a JP-8/air mixture. The minimum spiral length that can be used in a JP-8 fueled PDE was found to be 0.91 m (36 in). The minimum purge fraction that can safely be used in a JP-8 fueled pulse detonation engine was found to be 0.3. Increasing frequency was found to have a positive effect on the performance of a PDE. DDT time is inversely related to frequency, while ignition time and detonation distance are relatively independent of frequency. Decreasing the equivalence ratio from 1.05 to 1.00 at fuel injection temperatures above the flash vaporization temperature produces a decrease in ignition time, with no impact on DDT time or detonation distance.

Fuel Heating System

The performance of fuel heating system was analyzed. The heat exchanger system was found to facilitate adequate transfer of detonation tube waste heat to increase the fuel injection temperature of low vapor pressure fuels enough to induce endothermic reactions. It was also determined that if flash vaporization of the fuel is the only objective for heat exchanger use, then only a single heat exchanger is necessary.

Recommendation for Future Work

The ignition and DDT times demonstrated during this research need to be decreased by an order of magnitude if higher frequency operation is to be reached. Heating the fuel to endothermic temperatures may be the solution to this problem. Research of endothermic fuel injection temperatures should be pursued based on the potential for substantial increases in performance. At the very least, JP-8 should be examined to determine the effect on the key PDE performance parameters of increasing the fuel injection temperature to 1000 K (1340 ˚F). All preparation work has been done for the endothermic research.

The variation of ignition time with respect to increasing fuel injection temperature for a JP-8/air mixture needs further analysis. The hypothesis given as an explanation for the trend, discussed in Chapter V, should be analyzed further. The portion of the trend, where ignition time increases with increasing fuel injection temperature is the most interesting. Merely stating that thermal degradation causes this increase in ignition time is not sufficient. A thorough understanding of how thermal degradation adversely affects the fuel/air ignition is needed.

The stainless steel heat exchanger design, while carefully analyzed, failed due to fatigue. The thermal stresses in the welded joints caused the welds to crack after several hours of testing. While this was not a major concern for this effort, if follow-on work is to be performed, either a new design or a modification of the current design should be pursued.

Appendix A: Individual Fuel Performance Analysis

Experimental results for individual fuel tests are presented. The results include ignition time, DDT time, detonation distance, 1400 m/s wavespeed percentage, and detonation percentage. As stated in Chapter V, the error bars shown in this Appendix are actually 95% confidence intervals. The test conditions for all tests were identical:

- Frequency – 20 Hz
- Ignition Delay – 4 msec
- Fill Fraction – 1.0
- Purge Fraction – 0.5
- Air Temperature – 394 K (250 ˚F)
- Tube Length – 1.829 m (72 in)
- Spiral Length – 0.914 m (36 in)
- 2 Tubes

JP-8

The primary fuel studied in this research was JP-8. It was given the most attention since it is the most likely end state fuel for use in operational pulse detonation engines. Figure 65 is a plot of the ignition time as a function of fuel injection temperature. An unexpected trend is identified in Figure 65. The ignition time appears to decrease initially with increasing fuel injection temperature. A minimum ignition time of 6.53 msec is noted at 533 K (500 ˚F). At approximately the flash vaporization temperature, the ignition time begins to increase with an increase in fuel injection temperature. A maximum ignition time of 7.24 msec is noted at 700 K (800 ˚F). Finally, at approximately the supercritical temperature, the ignition time begins to decrease again with increasing fuel injection temperature. While this trend only occurs over a span of 1

msec, it is still significant. This explanation for this trend was discussed in Chapter V. The standard deviation of ignition time is nearly independent of fuel injection temperature, with a value of approximately 0.7 msec for all temperatures.

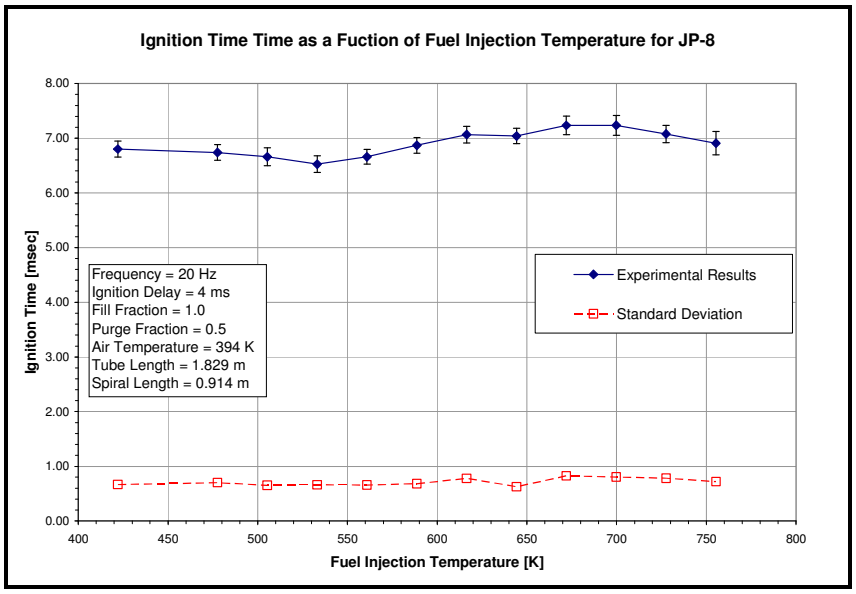

Figure 65. Ignition time as a function of fuel injection temperature for a JP-8/air mixture

The detonation to deflagration transition time as a function of fuel injection temperature is shown in Figure 66. The DDT time drops nearly linearly from 2.65 to 2.25 msec. That is a decrease of 17.8%, which is not huge, but is a strong trend. The standard deviation of DDT time fluctuates mildly, but remains fairly constant at 0.2 msec for all fuel injection temperatures.

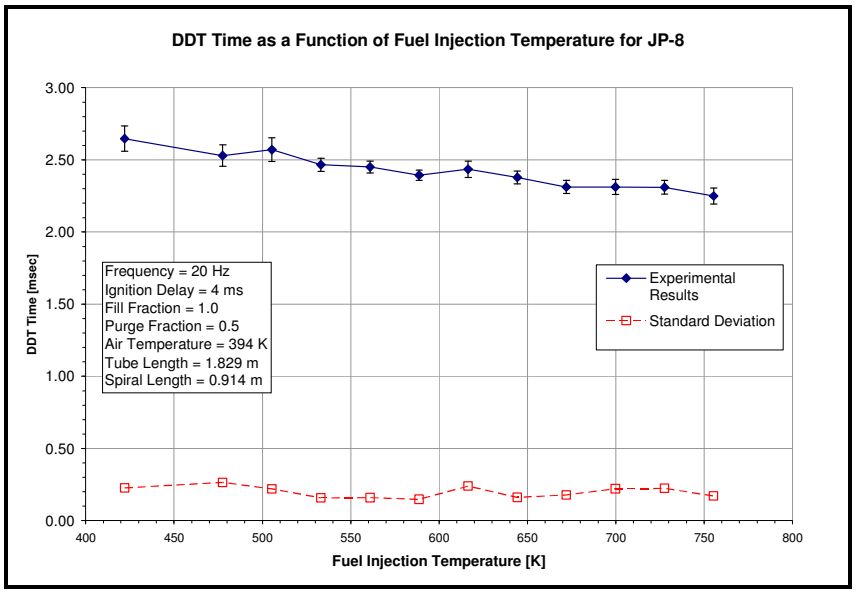

Figure 66. DDT time as a function of fuel injection temperature for a JP-8/air mixture

Figure 67 is a plot of detonation distance as a function of fuel injection temperature. The detonation distance shows a decrease of 11 cm (4.37 in) over the temperature range. This is very close to the change in detonation distance that was estimated by examining the wavespeeds, shown in Figure 45. The examination of wavespeeds estimated a decrease in detonation distance of 10 cm (3.94 in). The key difference between the detonation distance and the DDT time trends is that the detonation distance trend is not linear. The majority of the detonation distance reduction takes place as the fuel injection temperature is heated up to the flash vaporization temperature. After the flash vaporization temperature is reached, detonations occur very close to the end of spiral. The standard deviation of the detonation distance remains constant throughout the temperature range.

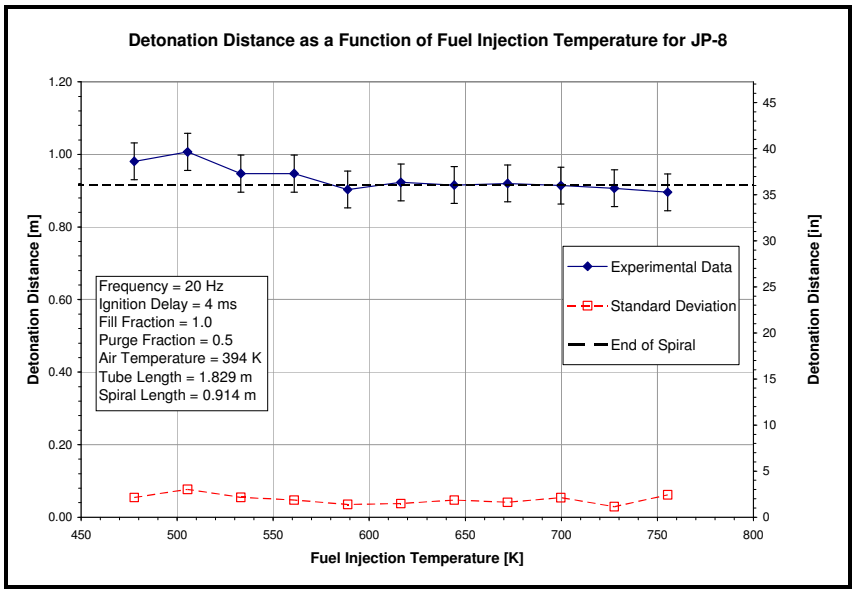

Figure 67. Detonation distance as a function of fuel injection temperature for a JP-8/air mixture

The final parameters examined were the detonation percentage and 1400 m/s wavespeed percentage. The detonation percentage and 1400 m/s wavespeed percentage as a function of fuel injection temperature are shown in Figure 68.

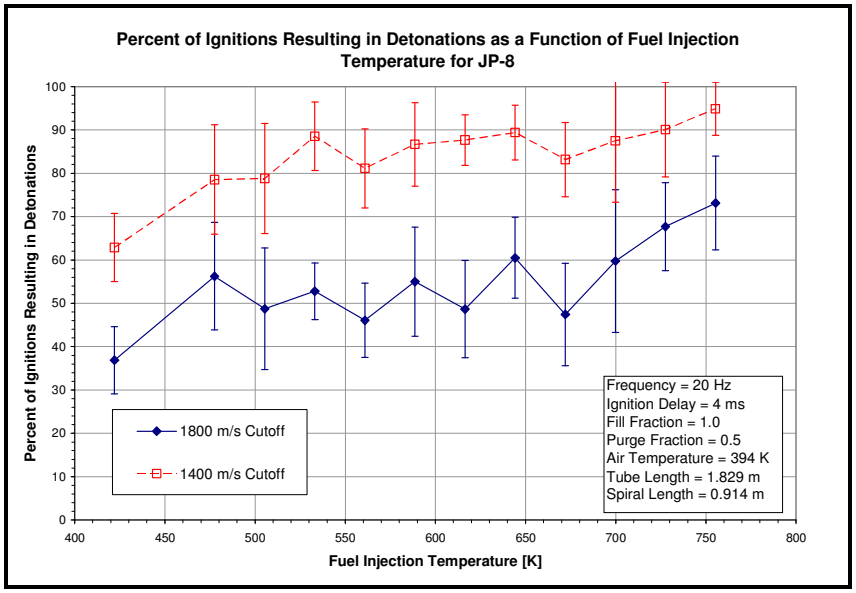

Figure 68. Detonation percentage and 1400 m/s wavespeed percentage as a function of fuel injection temperature for a JP-8/air mixture

The 1400 m/s wavespeed percentage increases from 62.9 to 94.9% over the temperature range. The detonation percentage increases from 36.9 to 73.1%. The majority of the performance gains, for both parameters, are seen between 422 and 533 K (300 and 500 ˚F) and then between 700 and 755 K (800 and 900 ˚F).

JP-7

The ignition time for JP-7 as a function of fuel injection temperature is shown in Figure 69. The ignition time trend demonstrated in JP-8 is also seen in JP-7, but at a much lower magnitude. In fact, the trend is so slight that the ignition time for JP-7 can be assumed independent of fuel injection temperature. The average ignition time for a JP-7/air mixture over the entire temperature range is 6.59 msec. The standard deviation of ignition time is also independent of fuel injection temperature with an average value of 0.68 msec.

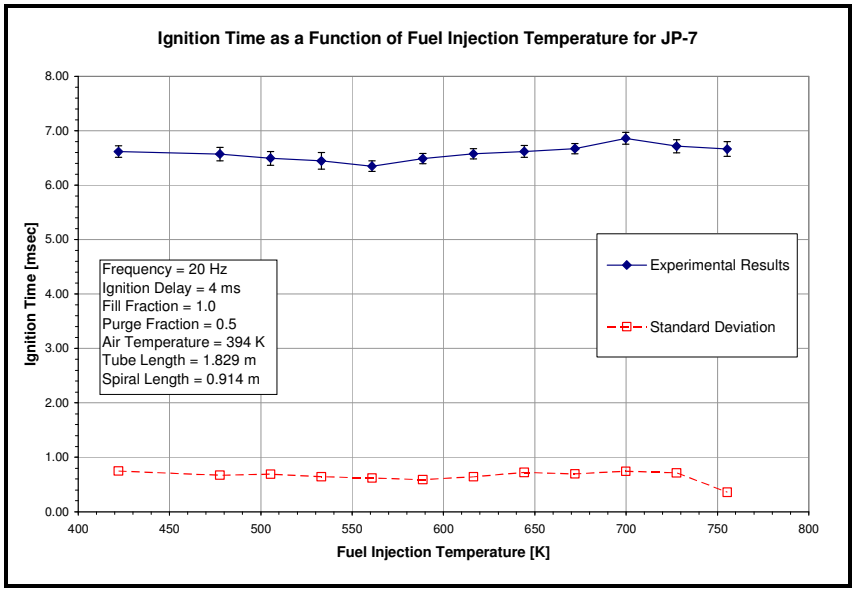

Figure 69. Ignition time as a function of fuel injection temperature for a JP-7/air mixture

Figure 70 is a plot of DDT time as a function of fuel injection temperature for JP-7. A obvious decline in DDT time is noted as the fuel injection temperature is increased. The trend is linear in nature, with DDT time decreasing from 2.59 to 2.31 msec. This is a 12% decrease in DDT time. The standard deviation of DDT time actually decreased from 0.186 to 0.126 msec, a 33% decrease. The reduction in standard deviation means that the scatter of the data is reduced as fuel injection temperature is increased.

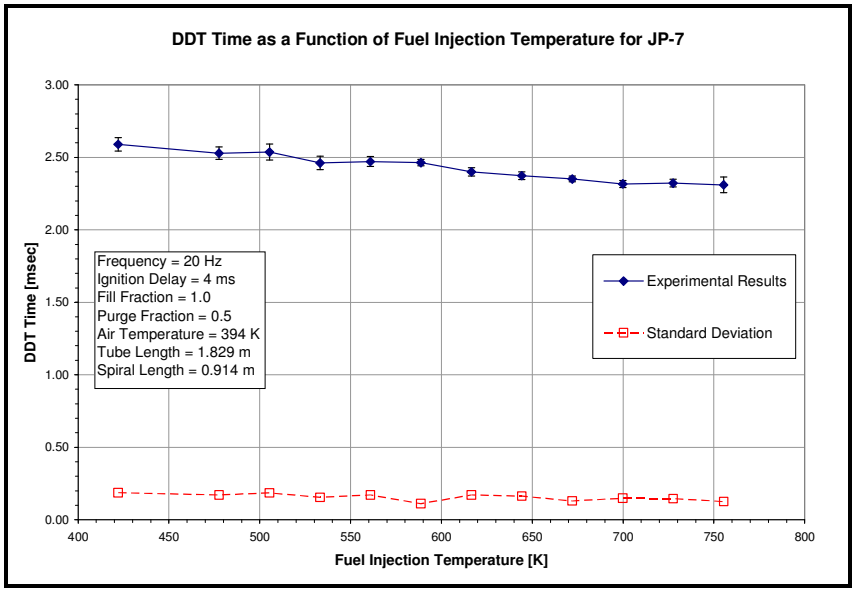

Figure 70. DDT time as a function of fuel injection temperature for a JP-7/air mixture

The detonation distance of a JP-7/air mixture as a function of fuel injection temperature is shown in Figure 71. The detonation distance decreases steadily from 1.14 to 0.89 m (44.9 to 35.0 in). This is a reduction of 25 cm (9.9 in), or 22%. The standard deviation of the detonation distance drops drastically as fuel injection temperature increases. The decline in standard deviation is a result of the detonation consistency increasing as fuel injection temperature is increased.

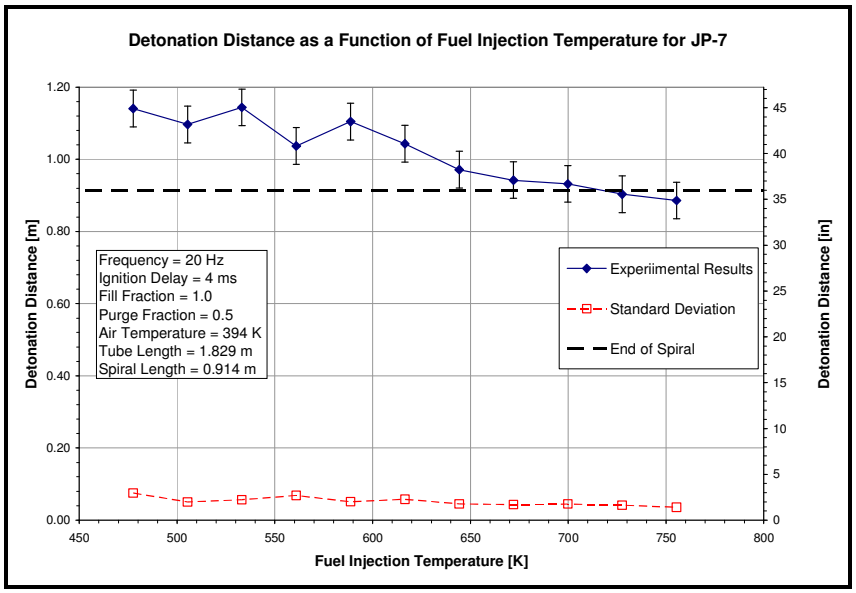

Figure 71. Detonation distance as a function of fuel injection temperature for a JP-7/air mixture

Figure 72 is a plot of the detonation percentage and 1400 m/s wavespeed percentage for JP-7 as a function of fuel injection temperature.

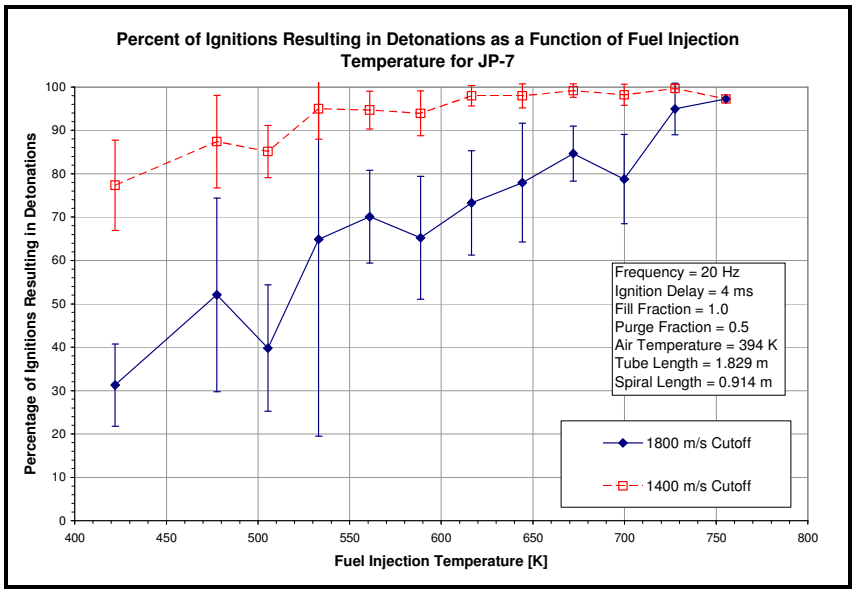

Figure 72. Detonation percentage and 1400 m/s wavespeed percentage as a function of fuel injection temperature for a JP-7/air mixture

Both parameters show an increase in detonation percentage as the fuel injection temperature increases. The 1400 m/s wavespeed percentage increases from 77.3 to 97.2% over the temperature range. The detonation percentage shows dramatically more impressive results with an increase from 31.3 to 97.2% as the fuel injection temperature increases from 422 to 755 K (300 to 900 ˚F).

JP-10

The ignition time as a function of fuel injection temperature for JP-10 is shown in Figure 73. JP-10 was only tested over a temperature range of 422 to 700 K (300 to 800 ˚F).

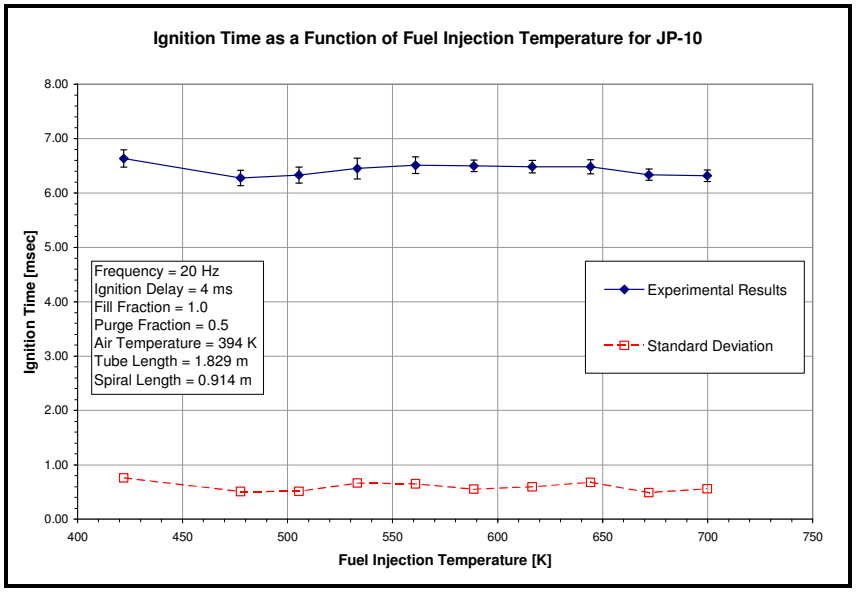

Figure 73. Ignition time as a function of fuel injection temperature for a JP-10/air mixture

The ignition time of a JP-10/air mixture demonstrates no notable relationship to the fuel injection temperature. An average ignition time of 6.43 msec is found along the

temperature range. The standard deviation of the ignition time is also independent of fuel injection temperature, with an average value of 0.60 msec.

The detonations of JP-10/air mixture were so infrequent that reliable detonation data could not be acquired. JP-10/air mixtures can be detonated, but not properly with the experimental setup used for this research. The poor detonation frequency is shown in Figure 74. Figure 74 is a plot of the detonation percentage and 1400 m/s wavespeed percentage as a function of fuel injection temperature for a JP-10/air.

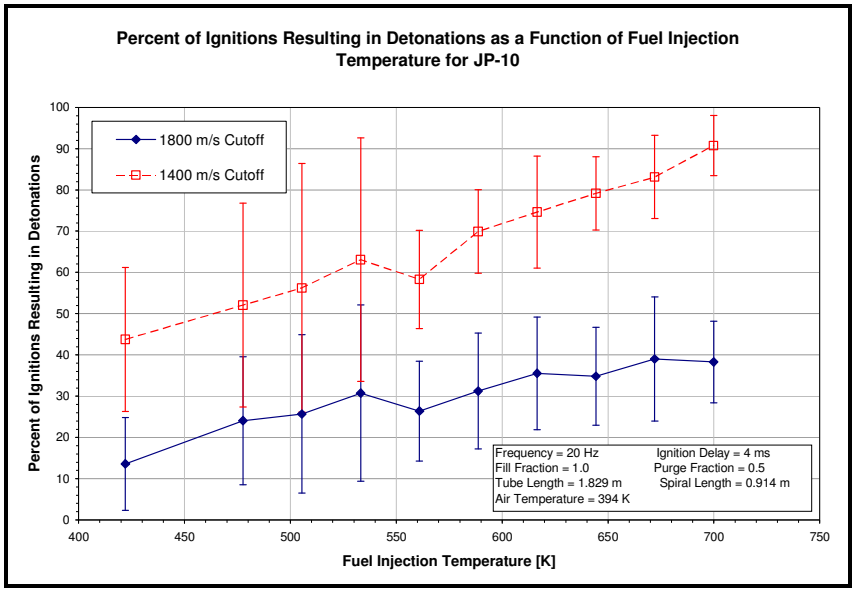

Figure 74. Detonation percentage and 1400 m/s wavespeed percentage as a function of fuel injection temperature for a JP-10/air mixture

The 1400 m/s wavespeed percentage shows a relatively good percentage at high temperatures, with a linear increase from 44 to 91%. The detonation percentage does not demonstrate nearly as high a dependence on fuel injection temperature, with only a slight increase from 14 to 38%. Even at very high temperatures, detonations occur less than

half of the time. This is the reason for the inconsistent detonation data that led to the inability to accurately determine DDT time and detonation distance.

JP-900

The ignition time for a JP-900/air mixture as a function of fuel injection temperature is shown in Figure 75. The ignition time is relatively constant as fuel injection temperature increases. An average ignition time of 6.66 msec for the entire temperature range was noted. The standard deviation of ignition time is also independent of fuel injection temperature, with an average value of 0.62 msec.

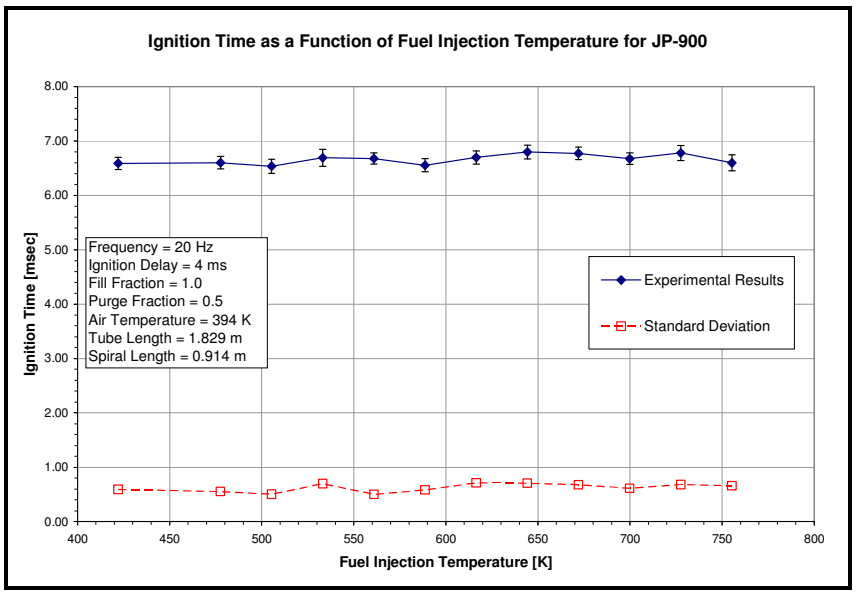

Figure 75. Ignition time as a function of fuel injection temperature for a JP-900/air mixture

Figure 76 is a plot of the DDT time as a function of fuel injection temperature for a JP-900/air mixture. The DDT time decreases nearly linearly from 2.65 to 2.35 msec,

which results in a 12.6% decrease. The standard deviation of DDT time does not demonstrate any consistent trend over thee temperature range.

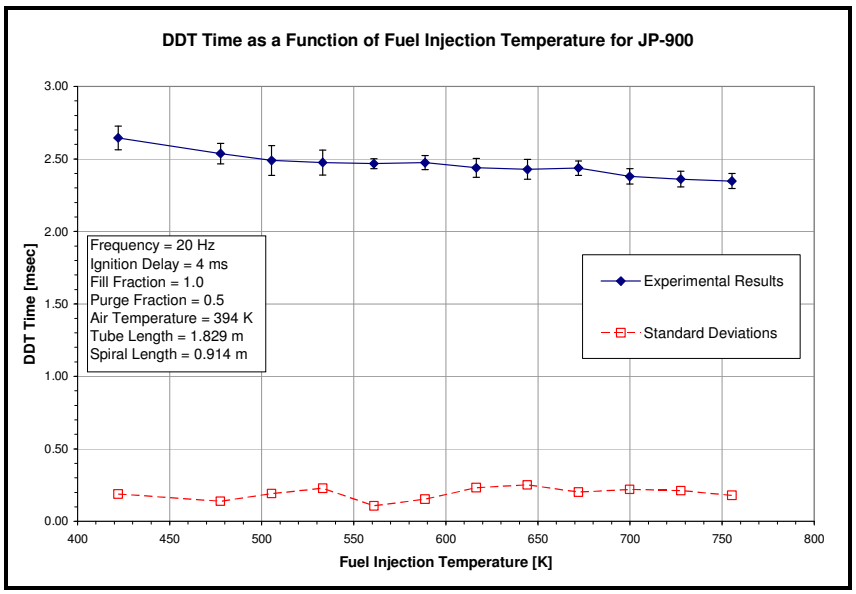

Figure 76. DDT time as a function of fuel injection temperature for a JP-900/air mixture

The detonation distance for a JP-900/air mixture as a function of fuel injection temperature is shown in Figure 77. The detonation distance decreases from 1.03 to 0.85 m (40.6 to 33.5 in). This results in a net reduction in detonation distance of 0.18 m (7.1 in). The detonation distance decreases fairly linearly over the temperature range. The standard deviation of detonation distance is constant, except for a sizable decrease in the upper temperatures. The standard deviation of detonation distance decreases from 0.11 to 0.06 m (4.33 to 2.36 in) the range of 644 to 755 K (700 to 900 ˚F). The decrease in standard deviation is a result of the increase in detonation consistency.

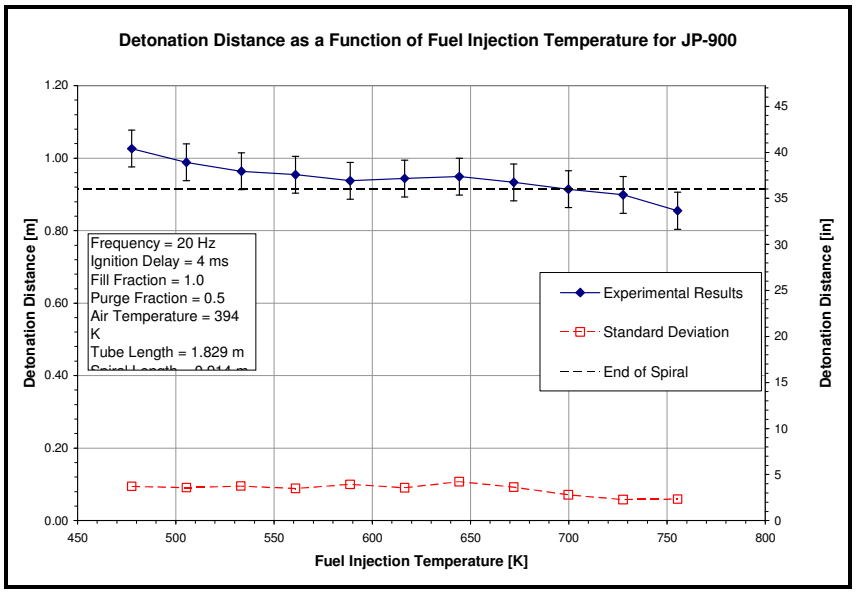

Figure 77. Detonation distance as a function of fuel injection temperature for a JP-900/air mixture

Figure 78 displays the detonation percentage and 1400 m/s wavespeed percentage as a function of fuel injection temperature for a JP-900/air mixture.

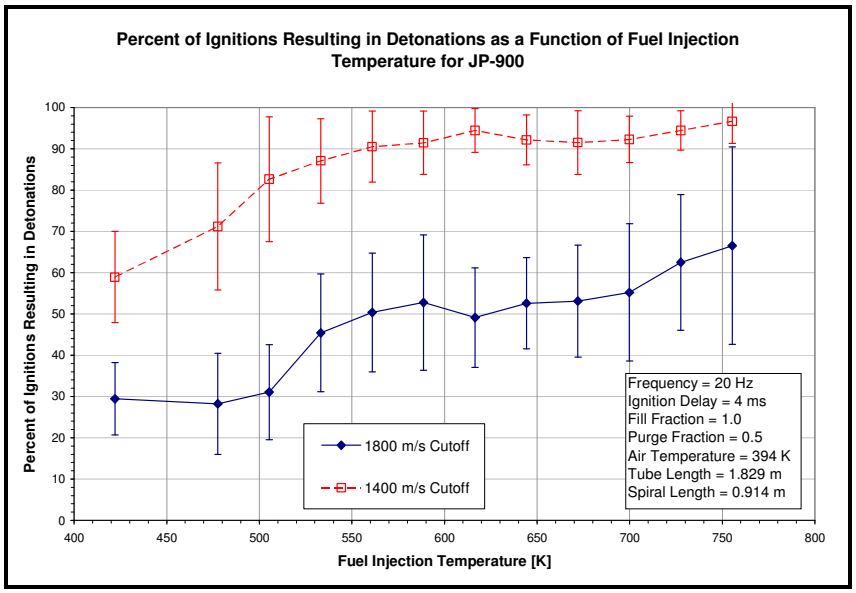

Figure 78. Detonation percentage and 1400 m/s percentage as a function of fuel injection temperature for a JP-900/air mixture

The 1400 m/s wavespeed percentage increases from 58.9 to 96.7%, while the detonation percentage increases from 29.5 to 66.5%. The major increase in 1400 m/s wavespeed percentage and detonation percentage occurred between 422 and 616 K (300 and 650 ˚F).

RP-1

The ignition time for an RP-1/air mixture as a function of fuel injection temperature is shown in Figure 79. Again, the ignition time appears relatively constant for the entire temperature range. There is similarity to the ignition time trend for JP-8, but it is on such a small magnitude compared to the standard deviation that it is, for all practical purposes, constant. The average ignition time over the temperature range is 6.62 msec. The standard deviation of the ignition time is independent of the fuel injection temperature. The average standard deviation over the entire temperature range is 0.63 msec.

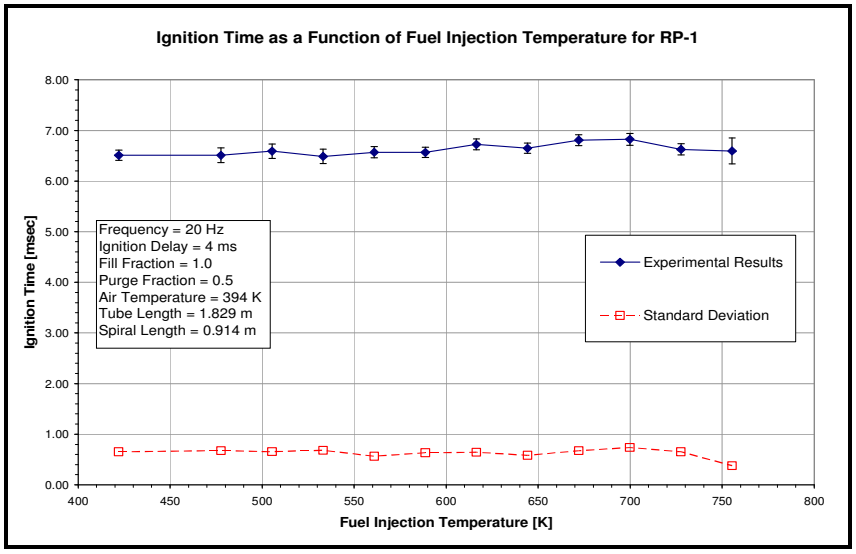

Figure 79. Ignition time as a function of fuel injection temperature for a RP-1/air mixture

Figure 80 presents the DDT time of a RP-1/air mixture as a function of fuel injection temperature. The DDT time is inversely related to the fuel injection temperature, and decreases linearly from 2.58 to 2.29 msec. That is a decrease of 12.7% decrease in DDT time. With exception of the point at 755 K (900 ˚F), the standard deviation of DDT time is kept constant at 0.15 msec.

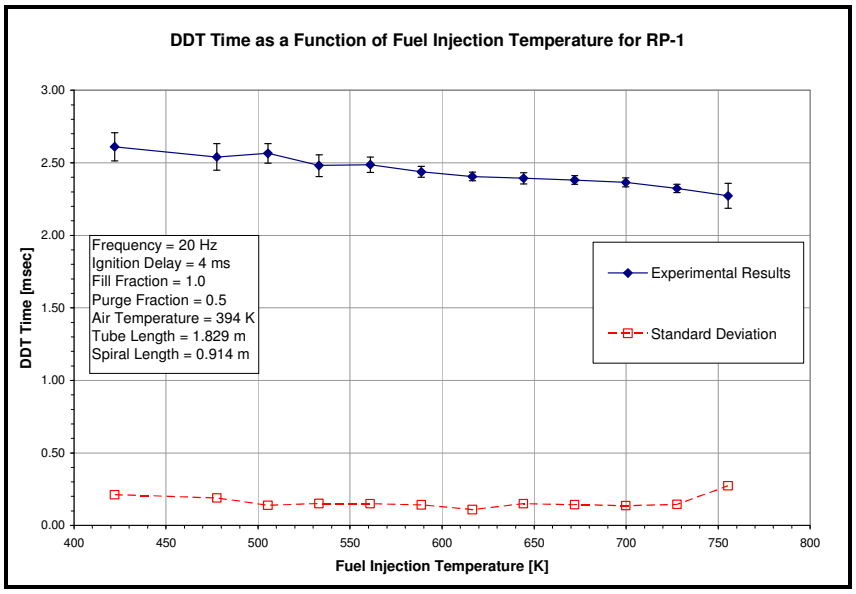

Figure 80. DDT time as a function of fuel injection temperature for a RP-1/air mixture

The detonation distance of a RP-1/air mixture is shown in Figure 81 as a function of fuel injection temperature. The detonation distance decreases, nearly linearly, from 1.02 to 0.89 m (40.2 to 35.0 in) over the temperature range. That is a 0.13 m (5.2 in) decrease in detonation distance. The standard deviation of the detonation distance is 10.1 cm (4 in) and below for all temperatures.

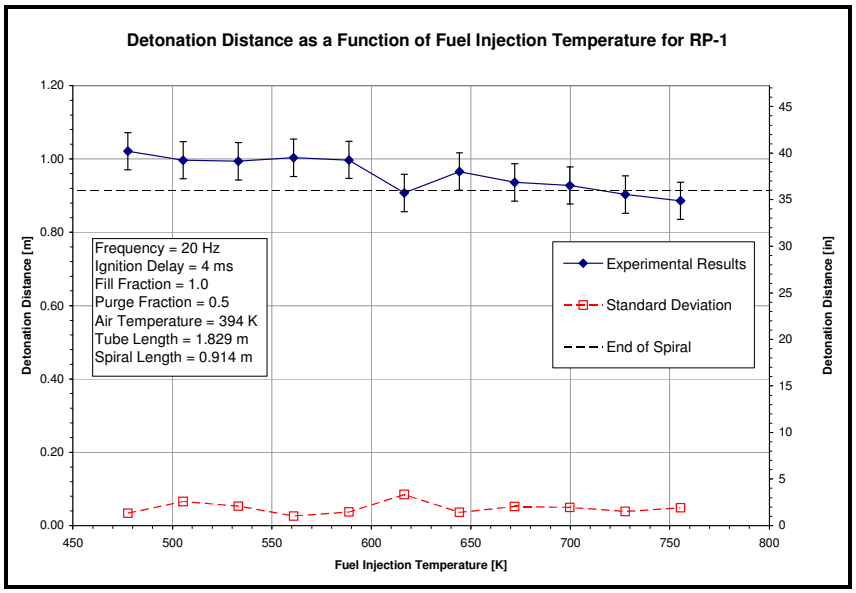

Figure 81. Detonation distance as a function of fuel injection temperature for a RP-1/air mixture

The detonation percentage and 1400 m/s wavespeed percentage of a RP-1/air mixture as a function of fuel injection temperature are displayed in Figure 82.

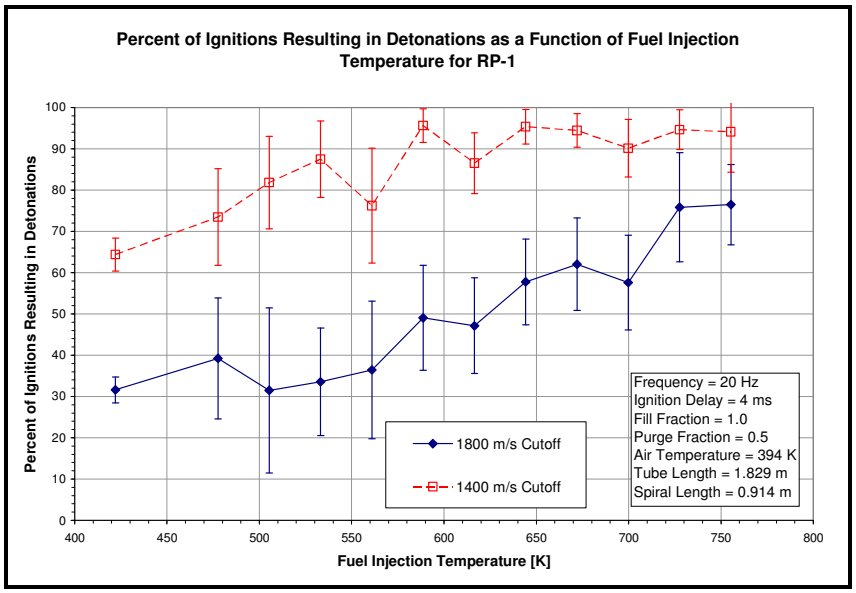

Figure 82. Detonation percentage and 1400 m/s wavespeed percentage as a function of fuel injection temperature for a RP-1/air mixture

The detonation percentage and the 1400 m/s wavespeed percentage increased significantly with increasing fuel injection temperature. The 1400 m/s wavespeed percentage demonstrated an increase from 64.4 to 94.1%, while the detonation percentage showed an increase from 32.6 to 76.5%.

S-8

Figure 83 is a plot of the ignition time for an S-8/air mixture as a function of fuel injection temperature. The ignition time remains constant at 6.25 msec for temperatures up to 616 K (650 ˚F). Above 616 K (650 ˚F), a hump is formed that is similar to the upper temperature trend of JP-8. This presents a maximum value of 6.64 msec at 700 K (800 ˚F), that is less than a half-millisecond different from the average value below 616 K (650 ˚F). The standard deviation of the ignition time is relatively constant, with the exception of the point at 755 K (900 ˚F), producing an average value of 0.646 msec.

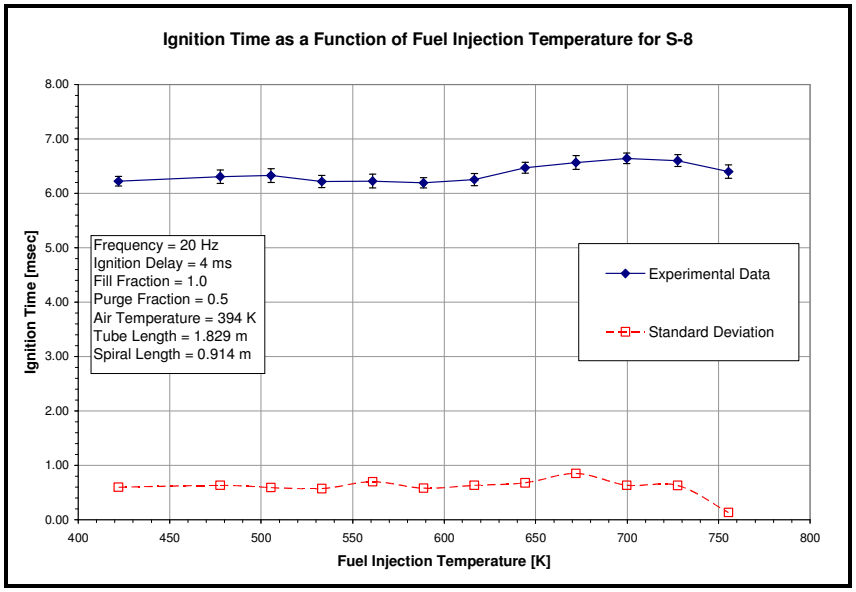

Figure 83. Ignition time as a function of fuel injection temperature for an S-8/air mixture

The DDT time of an S-8/air mixture is shown in Figure 84 as a function of fuel injection temperature. As with all of the fuels examined, the DDT time has an inverse linear relationship with the fuel injection temperature. The DDT time linearly decreases from 2.60 to 2.26 msec, a 15% decrease. The standard deviation of DDT time is constant at a value of 0.15 msec, with exception of the point at 755 K (900 ˚F). The 755 K (900 ˚F) point has a standard deviation larger then the other points, because less data was captured at that temperature.

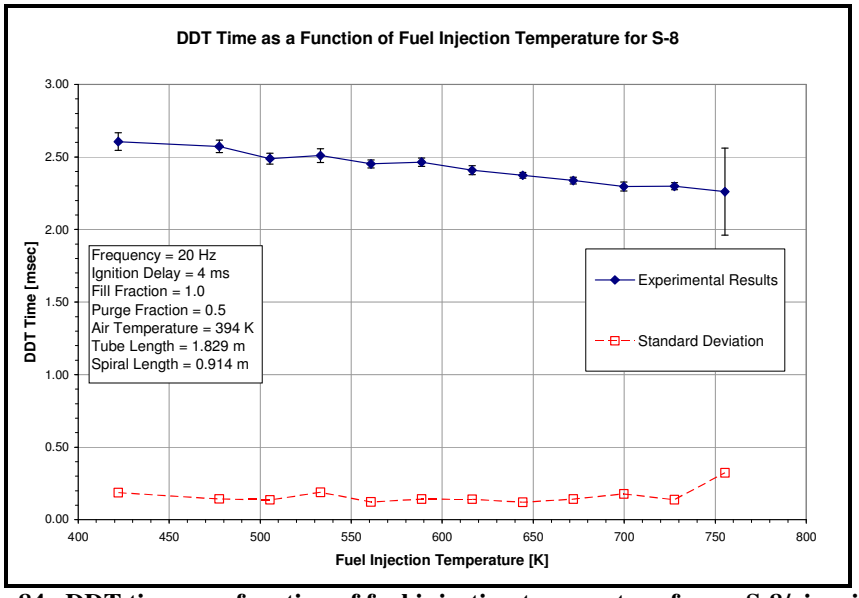

Figure 84. DDT time as a function of fuel injection temperature for an S-8/air mixture

The detonation distance of an S-8/air mixture is displayed as a function of fuel injection temperature in Figure 85. The detonation distance has an inverse relationship with the fuel injection temperature, with a decrease from 1.05 to 0.89 m (41.3 to 35.0 in). This is a decrease of 0.14 m (6.3 in), or 13%. The most interesting result of the S-8 detonation distance study is that it remains nearly constant up to 616 K (650 ˚F). A large

drop occurs between 616 and 644 K (650 and 700 ˚F), then only a small decrease in detonation distance occurs above 644 K (700 ˚F). The standard deviation is roughly constant at 5.6 cm (2.2 in) for the entire temperature range, except the 755 K (900 ˚F) point.

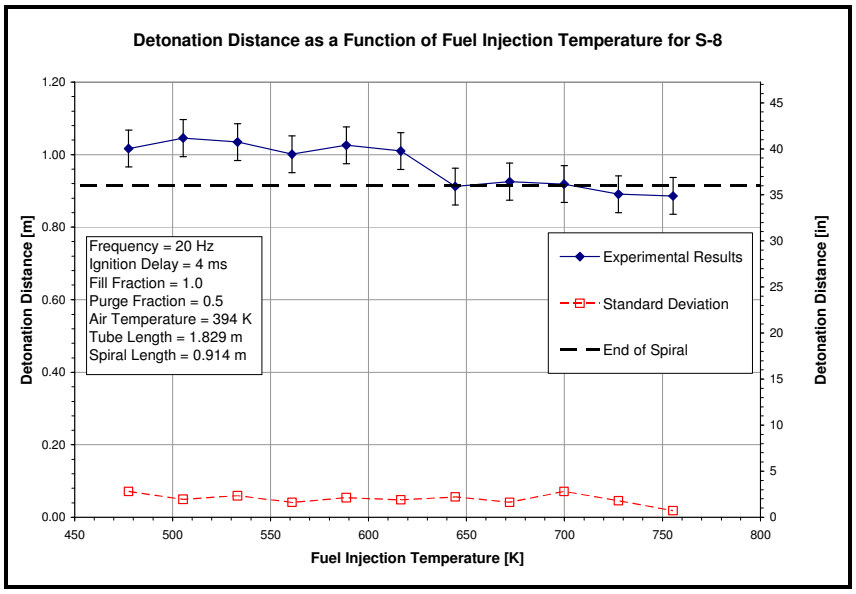

Figure 85. Detonation distance as a function of fuel injection temperature for an S-8/air mixture

The final parameters examined, the detonation percentage and 1400 m/s wavespeed percentage, are presented in Figure 86 as a function of fuel injection temperature. As noted in Chapter V, S-8 has the most consistent detonations. The 1400 m/s wavespeed percentage increases from 83.5 to 100%, with 100% detonations for all temperature above and including 672 K (750 ˚F). The detonation percentage is also impressive, with a nearly linear increase from 35.5 to 100% as fuel injection temperature increases.

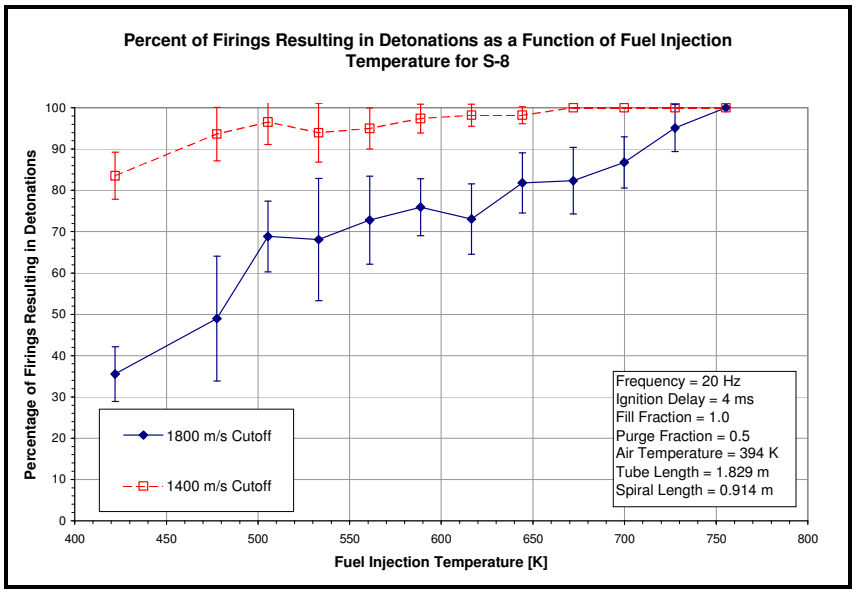

Figure 86. Detonation percentage and 1400 m/s wavespeed percentage as a function of fuel injection temperature for an S-8/air mixture

Appendix B: Analysis of Heat Exchangers

To ensure that all experimentation was conducted as safely as possible, a detailed analysis of the heat exchangers was performed. A *MATLAB* program was written to analyze the heat exchanger (including thermal stresses) and determine a factor of safety (FS) for each section of the heat exchanger. There were six key areas analyzed by the *MATLAB* program: Inner tube hoop stress, outer tube hoop stress, inner tube longitudinal stress, outer tube longitudinal stress, bending in the end plates, and the weld between the inner tube and the end plates.

Description of MATLAB Program

The program began with a short input section. The length of the heat exchangers was entered into the program, with 36 inches as the default. The ambient temperature could be varied, but was set at 70 ˚F as a default. The maximum temperature for both the inner and outer tubes was input into the program. The fuel pressure could also be varied. Finally, the material of the tubes and endplates was entered.

The program begins by assigning material properties and dimensions based on the inputs. The program was design for three different materials: Type 316 stainless steel, inconel 600, and inconel 625. Dimensions were assigned based on pipe schedule selection, 10 or 40. In addition, different thicknesses of end plates could be analyzed. The entire program was written in English units; therefore, within this Appendix S.I. units will be omitted.

The various sections of the heat exchangers are then analyzed using the methodology described below. The final output of the program is a value of stress in each section accompanied by a FS that is calculated using the yield strength of the material. A copy of the *MATLAB* code is not included in this document.

Material Properties

Before analysis of the particular sections could begin, four key structural parameters had to be found: Modulus of elasticity, coefficient of thermal expansion, yield tensile strength of the material, and the ultimate shear strength of the material. All material properties were acquired from MMPDS-01 (MMPDS, 2003). All four parameters vary significantly with temperature in the range analyzed.

Figure 87 is a plot of the modulus of elasticity for three metals as a function of temperature. A polynomial curve fit was applied to the data points for each of the metals, and is displayed in Figure 87. The lowest order polynomial curve, that accurately fit the data, was chosen. The equations of the curve fits were coded into the *MATLAB* program. In a similar fashion, polynomial curve fits were applied to the data sets for the other material properties. Figure 88, Figure 89, and Figure 90 display the data sets and polynomial curve fits for the coefficient of thermal expansion, yield tensile strength, and ultimate shear strength, respectively.

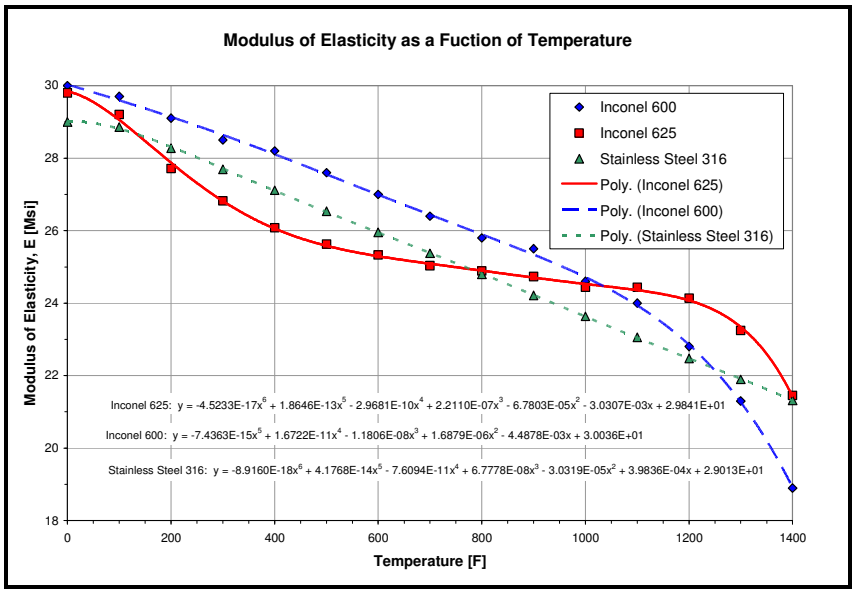

Figure 87. Modulus of elasticity for three metals as a function of temperature with polynomial curve fits to the data (data from MMPDS-01)

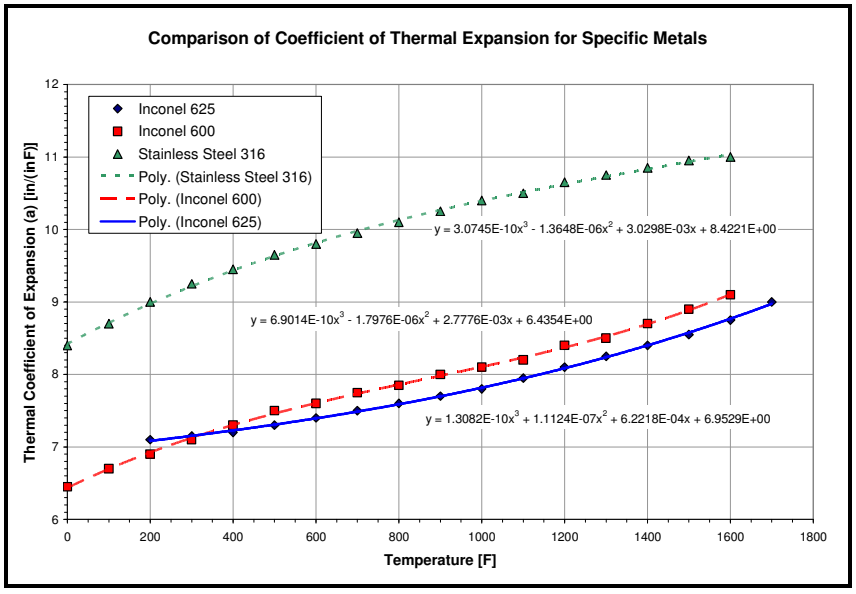

Figure 88. Coefficient of thermal expansion elasticity for three metals as a function of temperature with polynomial curve fits to the data (data from MMPDS-01)

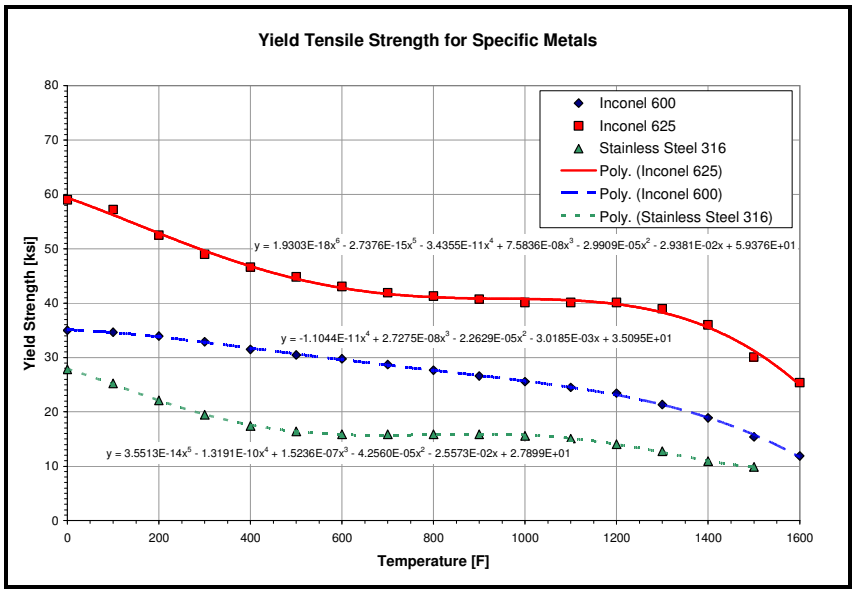

Figure 89. Yield tensile strength elasticity for three metals as a function of temperature with polynomial curve fits to the data (data from MMPDS-01)

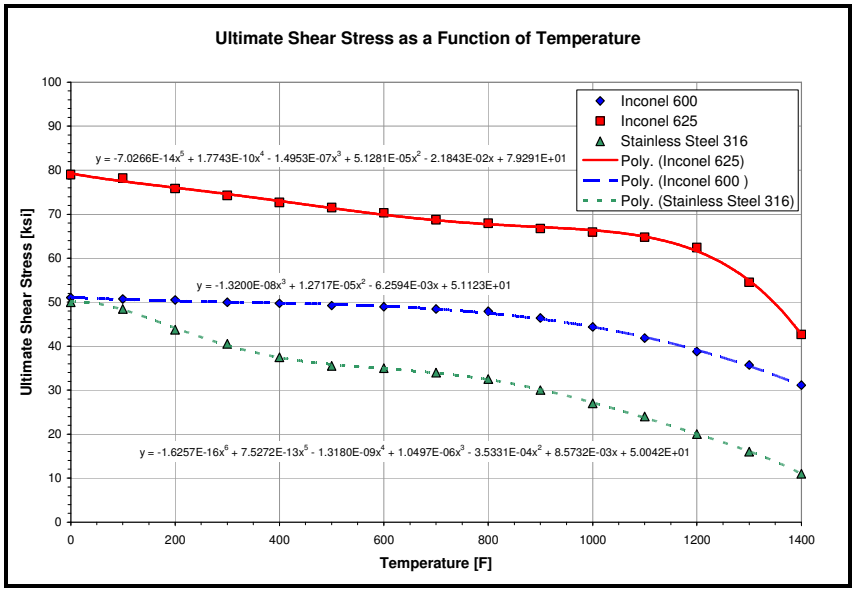

Figure 90. Ultimate shear stress for three metals as a function of temperature with polynomial curve fits to the data (data from MMPDS-01)

Analysis of Heat Exchanger Sections

The first two sections of the heat exchanger that were analyzed are the inner and outer tube hoop stress. The hoop stress, σ_{hoop}, for both the inner and outer tubes is given by Equation (24) (Beer, 2006:462):

$$\sigma_{hoop} = \frac{(P)(r)}{t} \tag{24}$$

where P is the *fuel pressure* in pounds per square inch, r is the *tube radius* in inches, and t is the *tube thickness* in inches.

The next sections examined were the inner and outer longitudinal stress, including the thermal stresses. First, the longitudinal stresses due to the fuel pressure for the inner and outer tubes were calculated using Equation (25) (Beer, 2005:462):

$$\sigma_{long} = \frac{(P)(r)}{2t} \tag{25}$$

where σ_{long} is the *longitudinal stress* due to the fuel pressure. Thermal stresses occur in the structure because the inner and outer tubes reach different temperatures; therefore, they expand at different rates. The difference in expansion rates causes the cooler tube (outer) to be loaded in tension, while the hotter tube (inner) is compressed. Next, the longitudinal stress due to thermal expansion was analyzed using the following assumptions:

- The load on the inner and outer tubes is equal and opposite
- The deflection of the two tubes is equal

The thermal stresses are then calculated by setting the deflections of the tubes equal to each other, as in Equation (26) (Popov, 1968:441-442):

$$\alpha_o(\Delta T_o)L_o + \frac{F_o L_o}{A_o E_o} = \alpha_i(\Delta T_i)L_i - \frac{F_i L_i}{A_i E_i} \tag{26}$$

where α is the *coefficient of thermal expansion* in inch per inch per degree Fahrenheit, ΔT is the *temperature difference* between the tube and ambient in degrees Fahrenheit, L is the *original length* in inches, F is the *load* in pounds, A is the *cross-sectional area* in square inches, E is the *modulus of elasticity* in pounds per square inch, and the subscripts o and i stand for *outer* and *inner*, respectively. If you rearrange Equation (26), set the inner and outer loads equal, and solve for the load, then Equation (27) arises:

$$F_{therm} = \frac{(\alpha_i(\Delta T_i)L_i - \alpha_o(\Delta T_o)L_o)}{\left(\frac{L_o}{A_o E_o} + \frac{L_i}{A_i E_i}\right)} \tag{27}$$

where F_{therm} is the *thermal load* in both tubes. The thermal stress is then equal to the load divided by the cross-sectional area. By combining the thermal stress and the longitudinal stress due to the fuel pressure, and recalling that the inner thermal stress is in compression, then Equations (28) and (29) can be solved to get the total stresses in the longitudinal direction for the inner and outer tubes, respectively:

$$\sigma_{long\_total\_i} = \sigma_{long\_i} - \frac{F_{therm}}{A_i} \tag{28}$$

$$\sigma_{long\_total\_o} = \sigma_{long\_o} + \frac{F_{therm}}{A_o} \tag{29}$$

where σ_{long_total} is the *total longitudinal stress*.

The fifth section to be examined is the bending load created on the end plates due to the thermal loads in the tubes. The plate is assumed to be a flat circulate plate, with the outside edge fixed and support, while the inside edge is guided, as shown in Figure 91.

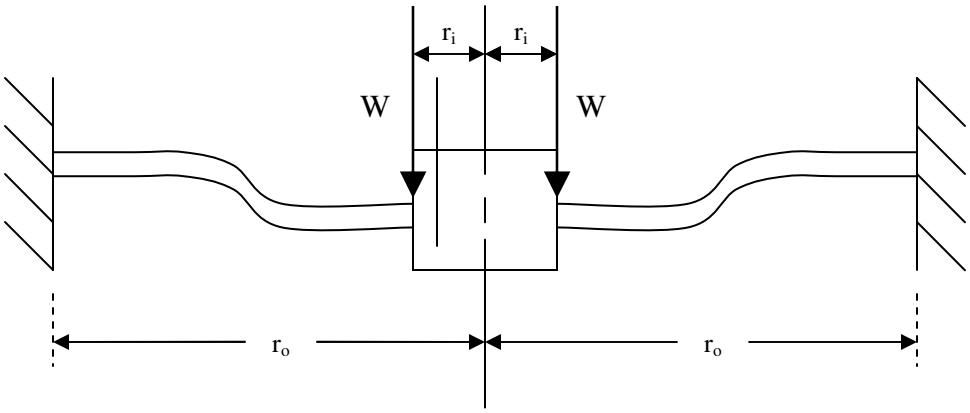

Figure 91. Schematic representation of the load applied to the end plates

The load is assumed to be applied along the inside edge. The shear load at the outer edge will be the highest load seen in this plate. The shear load at the outer edge is determined by Equation (30) and Equation (31) (Roark, 1989:402):

$$W = -\frac{F_{therm}}{r_i \pi} \tag{30}$$

$$\sigma_{bendshear} = \frac{-W r_i}{r_o} \tag{31}$$

where W is the *running load* along the inner edge in pounds per inch and $\sigma_{bendshear}$ is the *shear stress* along the outer edge due to bending in the plate.

The final section of the heat exchanger analyzed was the weld connecting the end plates to the inner tube. The shear stress in the weld is calculated using Equation (32) (Shigley, 1989:386-389):

$$\sigma_{weld} = \frac{1.414 F_{therm}}{t_{weld} L_{weld}} \tag{32}$$

where t_{weld} is the *weld thickness* in inches, L_{weld} is the *circumferential weld length* in inches, and σ_{weld} is the *weld shear stress*. This stress presented the largest problems.

As mentioned earlier, the factor of safety was found for each stress, based on the material properties. The factor of safety is defined by Equation (33):

$$FS = \frac{MaterialStrength}{AppliedStress} \tag{33}$$

The factors of safety for both the stainless steel heat exchangers and the inconel heat exchangers are shown in Table 11. The boundary conditions are also included in Table 11. The lowest factors of safety for both heat exchangers are found in the weld connecting the end plates to the inner tube. Overall, the inconel heat exchanger has far better factors of safety, which means less fatigue issues will arise with the inconel heat exchanger.

Table 11. Boundary conditions and resultant factors of safety for the six sections of both the stainless steel and inconel heat exchangers

	Stainless Steel Heat Exchanger	Inconel Heat Exchanger
Outer Tube Temp [F]	800	1000
Inner Tube Temp [F]	1000	1400
Fuel Pressure [psi]	1200	1500
Ambient Temp [F]	70	70
Initial Length [in]	36	36
Outer Tube Hoop Stress FS	2.597	3.067
Inner Tube Hoop Stress FS	2.235	2.657
Outer Tube Long. Stress FS	1.212	1.771
Inner Tube Long. Stress FS	1.190	2.191
End Plate Shear Stress FS	3.855	7.748
Weld Shear Stress FS	1.120	1.129

Appendix C: Critical Property Prediction Method

There are several correlations used to determine the critical properties of petroleum fuels. However, these correlations have been shown to be highly inaccurate for use on coal-based fuels. It is feasible to use the petroleum correlations to predict the critical properties of S-8, but not JP-900. A correlation has been developed to predict the critical properties of coal-based fuels, such as JP-900. Both the petroleum and coal-based fuel correlations only require the knowledge of two values for the fuel: Boiling point and specific gravity. The specific gravity of the two fuels is known, but the boiling point is not. The boiling point is found by averaging the 10% boiling fraction (BF), the 50% BF, and the 90% BF. Table 12 is summary of the boiling fractions and the resultant boiling points (T_b) for S-8 and JP-900. In addition, the other fuel properties used to determine the critical properties are included in Table 12.

Table 12. The boiling fractions and resultant boiling point along with the other fuel properties used to determine the critical properties for S-8 and JP-900

Fuel	10% BF [˚C]	50% BF [˚C]	90% BF [˚C]	Boiling Point [K]	Specific Gravity	API gravity
JP-900	192	204	243	486	0.78	49.91
S-8	169	201	249	479	0.87	31.14

where $APIgravity = 141.5/SG - 131.5$. The boiling point is given in units of Kelvin, since all correlations used to find the critical properties require the use of temperature in Kelvin. Once the boiling point is found, all of the necessary inputs for the correlations are known. The correlations used to determine the critical properties of S-8 and JP-900 are presented in the subsequent sections. (Yu, 1995:1)

S-8

Four methods were used to predict the critical properties of S-8. The average of the four methods was then used during this research. Unless otherwise noted, the determination of the critical properties for S-8 is taken from Riazi (Riazi, 2005:60-62). The first correlation use is referred to as the Cavett Method. Using the Cavett Method, the critical temperature and pressure are determined using Equations (34) and (35), respectively:

$$\begin{aligned} T_c = {} & 426.7062278 + \left(9.5187183\times10^{-1}\right)\left(1.8T_b - 459.67\right) \\ & - \left(6.01889\times10^{-4}\right)\left(1.8T_b - 459.67\right)^2 \\ & - \left(4.95625\times10^{-3}\right)\left(1.8T_b - 459.67\right)\left(API\right) \\ & + \left(2.160588\times10^{-7}\right)\left(1.8T_b - 459.67\right)^3 \\ & + \left(2.949718\times10^{-6}\right)\left(API\right)\left(1.8T_b - 459.67\right)^2 \\ & + \left(1.817311\times10^{-8}\right)\left(API\right)^2\left(1.8T_b - 459.67\right)^2 \end{aligned} \tag{34}$$

$$\begin{aligned} \log\left(P_c\right) = {} & 1.6675956 + \left(9.412011\times10^{-4}\right)\left(1.8T_b - 459.67\right) \\ & - \left(3.047475\times10^{-6}\right)\left(1.8T_b - 459.67\right)^2 \\ & - \left(2.087611\times10^{-5}\right)\left(1.8T_b - 459.67\right)\left(API\right) \\ & + \left(1.5184103\times10^{-9}\right)\left(1.8T_b - 459.67\right)^3 \\ & + \left(1.1047899\times10^{-8}\right)\left(API\right)\left(1.8T_b - 459.67\right)^2 \\ & - \left(4.8271599\times10^{-8}\right)\left(API\right)^2\left(1.8T_b - 459.67\right) \\ & + \left(1.3949619\times10^{-10}\right)\left(API\right)^2\left(1.8T_b - 459.67\right)^2 \end{aligned} \tag{35}$$

where T_c is the *critical temperature* in Kelvin, T_b is in Kelvin and P_c is the *critical pressure* in bar. The critical pressure was converted to atm for use in this research.

The second method used was developed by Kesler and Lee, known as the Lee-Kesler Method. The Lee-Kesler Method is used to determine the critical pressure and temperature, using Equations (36) and (37), respectively:

$$T_c = 189.8 + 450.6SG + \left(0.4244 + 0.1174SG\right)T_b + (0.1441 - 1.0069SG)\times 10^5 / T_b \quad (36)$$

$$\begin{aligned}\ln\left(P_c\right) = {} & 5.689 - 0.566/SG - \left(0.43639 + 4.1216/SG + 0.21343/SG^2\right)\times 10^{-3}T_b \\ & + \left(0.47579 + 1.182/SG + 0.15302/SG^2\right)\times 10^{-6}T_b^2 \\ & - \left(2.4505 + 9.9099/SG^2\right)\times 10^{-10}T_b^3\end{aligned} \quad (37)$$

where T_c and T_b are in Kelvin and P_c is in bar.

The third method used was developed by Riazi and Daubert, and is know as the Riazi-Daubert Method. There are actually three different correlations used in the Riazi-Daubert Method. Each correlation corresponds to a range of molecular weights. The correlation for molecular weights between 70 and 300 is used exclusively; and is defined by Equations (38) and (39):

$$T_c = 9.5233\left[\exp\left(-9.314\times 10^{-4}T_b - 0.544442SG + 6.4791\times 10^{-4}T_bSG\right)\right]T_b^{0.81067}SG^{0.53691} \quad (38)$$

$$P_c = 3.1958\times 10^5\left[\exp\left(-8.505\times 10^{-3}T_b - 4.8014SG + 5.749\times 10^{-3}T_bSG\right)\right]T_b^{-0.4844}SG^{4.0846} \quad (39)$$

where T_c and T_b are in Kelvin, and P_c is in bar.

The fourth method used is known as the Winn-Mobil Method. The Winn-Mobil Method uses Equations (40) and (41) to determine the critical temperature and pressure, respectively:

$$\ln\left(T_c\right) = -0.58779 + 4.2009 T_b^{0.08615} SG^{0.04614} \tag{40}$$

$$P_c = 6.148341 \times 10^7 T_b^{-2.3177} SG^{2.4853} \tag{41}$$

where T_c and T_b are in Kelvin and P_c is in bar.

The results of the four tests along with average values are displayed in Table 13. The four methods approximated the critical properties with a high level of similarity. The largest critical temperature difference was only 11 K, or 1.6%. The largest critical pressure difference was 2 atm, or 7.2%.

Table 13. Critical property results for S-8 using four correlation methods

Property	Cavett	Lee-Kesler	Riazi-Daubert	Winn-Mobil	Average
Critical Temperature [K]	682	681	687	676	**682**
Critical Pressure [atm]	27.74	26.97	25.74	26.33	**26.70**

JP-900

The correlations used for S-8 are not applicable for coal-based fuels, such as JP-900. Two methods of determining the critical properties for coal-based fuels are presented. The first method is known as the Tsonopoulos Method, and it predicts the critical temperature and pressure using Equations (42) and (43), respectively (Riazi, 2005:62):

$$\log_{10}(T_c) = 1.20016 + 0.61954\log_{10}(T_b) + 0.48262\log_{10}(SG) + 0.67365\left(\log_{10}(SG)\right)^2 \quad (42)$$

$$\log_{10}(P_c) = 7.37498 - 2.15833\log_{10}(T_b) + 3.35417\log_{10}(SG) + 5.64019\left(\log_{10}(SG)\right)^2 \quad (43)$$

where T_c and T_b are in Kelvin, and P_c is in bar.

The second method was determined by using the method of least squares. Only a correlation to determine the critical temperature is available in literature. The correlation used to determine the critical temperature is given in Equation (44) (Yu, 1995:408):

$$T_c = 138.98 + 2.1132\Delta - 1.4085\times10^{-3}\Delta^2 \quad (44)$$

where $\Delta = SG(T_b + 100)$, T_c is in degrees Fahrenheit, and T_b is in degrees Fahrenheit. Table 14 is summary of the results for the critical properties of JP-900. The critical temperature estimates for the two methods differ by 2.5%.

Table 14. Critical property results for JP-900 using two correlation methods

Property	Tsonopoulos Method	Method from Yu	Average
Critical Temperature [K]	661	678	**670**
Critical Pressure [atm]	25.60	N/A	**25.60**

Appendix D: Summary of Endothermic Heating System Development

The theoretical justification for heating low vapor pressure fuels to endothermic temperatures is presented. In addition, the experimental system developed to heat fuel to endothermic temperatures is presented. The endothermic fuel heating system presented has not been validated.

Background

As complex liquid hydrocarbons (such as JP-8) reach endothermic temperatures, they begin to break apart their molecular bonds (crack) and form smaller hydrocarbons and hydrogen molecules. Consequently, as complex hydrocarbons are cracked to produce simpler and smaller hydrocarbons the ignition and DDT times of the fuel/air mixture will decrease. Smaller, lighter hydrocarbon fuels have been shown to produce much shorter ignition and DDT times than the complex hydrocarbons studied in this research (Schauer, 2003:5-8). Hydrogen/air mixtures have been shown to have even lower ignition and DDT times than small hydrocarbon fuels (Schauer, 2001). The belief is that as the complex hydrocarbon chains within the low vapor pressure fuels break down and form smaller and lighter hydrocarbons, the ignition and DDT time will decrease. If this theory is taken to its limit, then all of the hydrocarbons will have broken down into hydrogen and carbon atoms. This leads to the hypothesis that if the endothermic reactions could continue until fruition, then the ignition and DDT times would ultimately decrease to that of a hydrogen/air mixture, as shown in Figure 92.

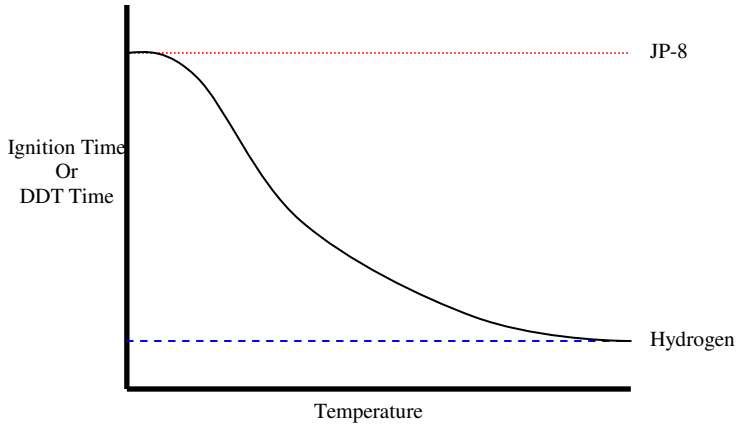

Figure 92. Generic diagram of theoretical effect of endothermic reactions upon the ignition and DDT time for a JP-8/air mixture

Non-PDE Endothermic Fuels Research

Significant research has gone into characterizing the performance of liquid hydrocarbon fuels undergoing endothermic reactions (Huang, 2004). Much of the endothermic fuel research was spawned because of the need for regenerative cooling in advanced engines, such as the scramjet (Huang, 2002). Dr. Huang's research provided exceptionally useful information regarding how liquid hydrocarbons, particularly JP-8+100, JP-7, and RP-1, perform when they reach endothermic temperatures. Once a liquid hydrocarbon has reached endothermic temperatures, the total energy in the fuel comes from two sources, physical heating (addition of energy) of the fuel and the energy absorbing (endothermic) chemical reaction.

One of the main issues with fuels that are heated to endothermic temperatures is the tendency for carbon deposits (coking) to form on the structure enclosing the fuel. Dr. Huang's research provided valuable insight into methods for coke mitigation. Testing

was performed to determine the effect of surface treatments on the magnitude of coke formation at high temperatures for JP-7. Three surface types were examined; zeolite catalyst/sol-gel coated, sol-gel coated, and uncoated stainless steel. There were no significant differences in the endothermic characteristics of the JP-7 due to application of the coatings; but there was an impressive reduction in coke formation with the coatings, especially the catalyst coating. In fact, the zeolite catalyst/sol-gel coating allowed endothermic reactions to occur four times as long as uncoated stainless steel, before coking began to degrade performance.

Experimental Setup

In preparation for future tests, two identical inconel heat exchangers were built. A photograph of the inconel heat exchangers is not included, because they are identical in appearance to the stainless steel heat exchangers (shown in Figure 29). The design of the inconel heat exchangers is identical to the stainless steel heat exchanger with one exception: The inner tubes was fabricated from 2" inconel alloy 625 schedule 10 pipe and outer tubes were fabricated from 2-½" inconel alloy 600 schedule 40 pipe. The inconel heat exchangers are equipped with the same instrumentation ports and fuel line connections as the stainless steel heat exchangers. The inconel heat exchangers utilize the same endplate construction and connecting extensions used in the long heat exchanger. The technical drawings of the inconel heat exchangers are shown in Appendix E.

The inconel heat exchangers were hydrostatically pressure tested in accordance with ASME B31.3, paragraph 345.4. The rated working temperature and pressure for the inconel heat exchangers are 1033.2 K (1400 ºF) and 102.07 atm (1500 psi), respectively.

As mentioned earlier, coking is a major problem when running liquid hydrocarbon fuels in the endothermic temperature regime. The large amounts of coke formed by the cracking of the fuel cause the orifices within the fuel supply system to clog with coke deposits. This is detrimental to testing and poses serious safety concerns. To alleviate the coking during future testing, a zeolite catalyst in a ceramic-like binder was used to coat all surfaces that will contact the endothermically reacting fuel. The benefits of this coating were discussed earlier. A contractor at their facility, using a proprietary process, applied the coating.

For testing that will occur in the endothermic temperature range, the spray bar and nozzle arrangement (shown in Figure 25) is not feasible due to coking issues. Coke forms on hot surfaces, but adheres to cooler surfaces. Since the spray bar is in the flow path of the cool fill air, coke will readily deposit on the nozzles. To alleviate this issue, a ½" male Swagelok fitting was welded to the fill air manifold to attach a single nozzle adaptor (see Figure 93). The adaptor, shown in Figure 93, was built by welding a nut to one end of a 10.16 cm (4 in) length of ½" stainless steel tubing. The nut is threaded to allow the insertion of a single Delevan nozzle. Swagelok fittings were added to the adaptor to allow for attachment to the Swagelok fittings on the fill air manifold and fuel line. This setup allows the nozzle to be placed outside of the cool air stream and be insulated during testing, greatly reducing coke build-up.

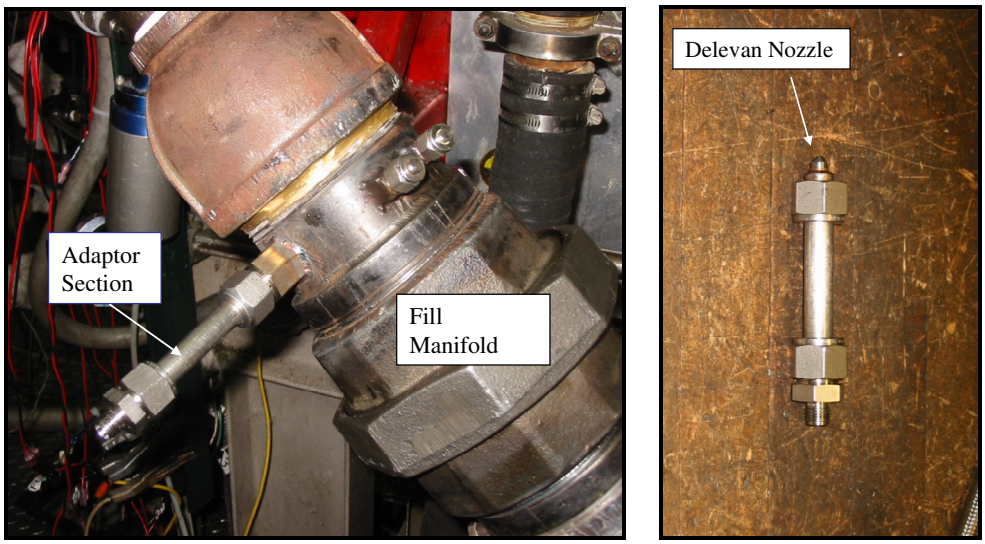

Figure 93. Photograph of the fuel injection setup (left) and Delevan nozzle adaptor (right) for use during endothermic testing

The complete endothermic fuel heating system consists of the nitrogen purge system, two inconel heat exchangers, instrumentation, and the associated tubing and fittings necessary to connect the critical components. All components of the endothermic fuel heating system are connected by ¼" stainless steel tubing and various stainless steel Swagelok fittings. The PDE is setup with two detonation tubes, each with an inconel heat exchanger.

An experimental setup has been designed for the endothermic testing. The fuel enters the test stand through a ball valve where the flow is then lead into the heat exchanger on tube four. After the fuel heat exchanger on tube four, it flows to the entrance of the heat exchanger on tube one. Upon exiting the heat exchanger on tube one, the fuel travels to the fill air manifold. The fuel is pushed through the offset Delevan flow nozzle and is injected perpendicular to the air stream. The flow path and the instrumentation are shown in schematic form in Figure 94.

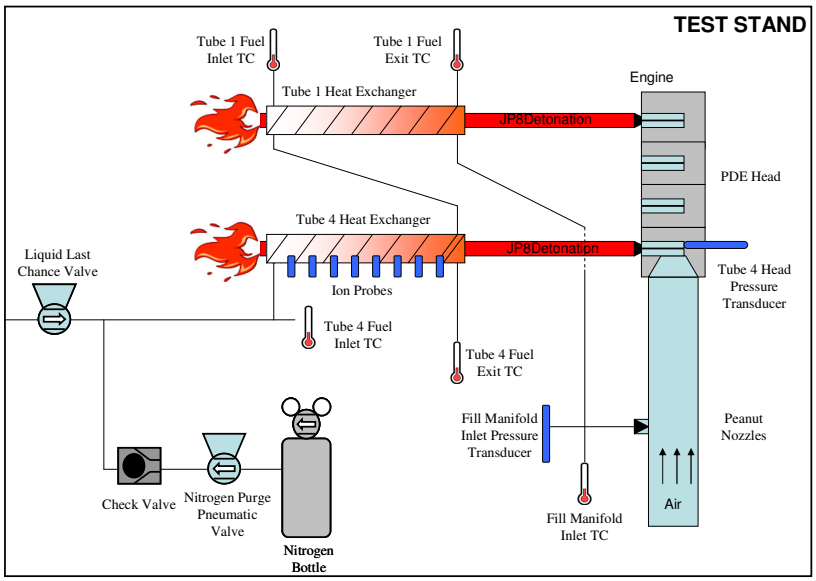

Figure 94. Diagram of PDE engine with endothermic fuel heating system and instrumentation

Appendix E: Heat Exchanger Technical Drawings

Stainless Steel Heat Exchanger

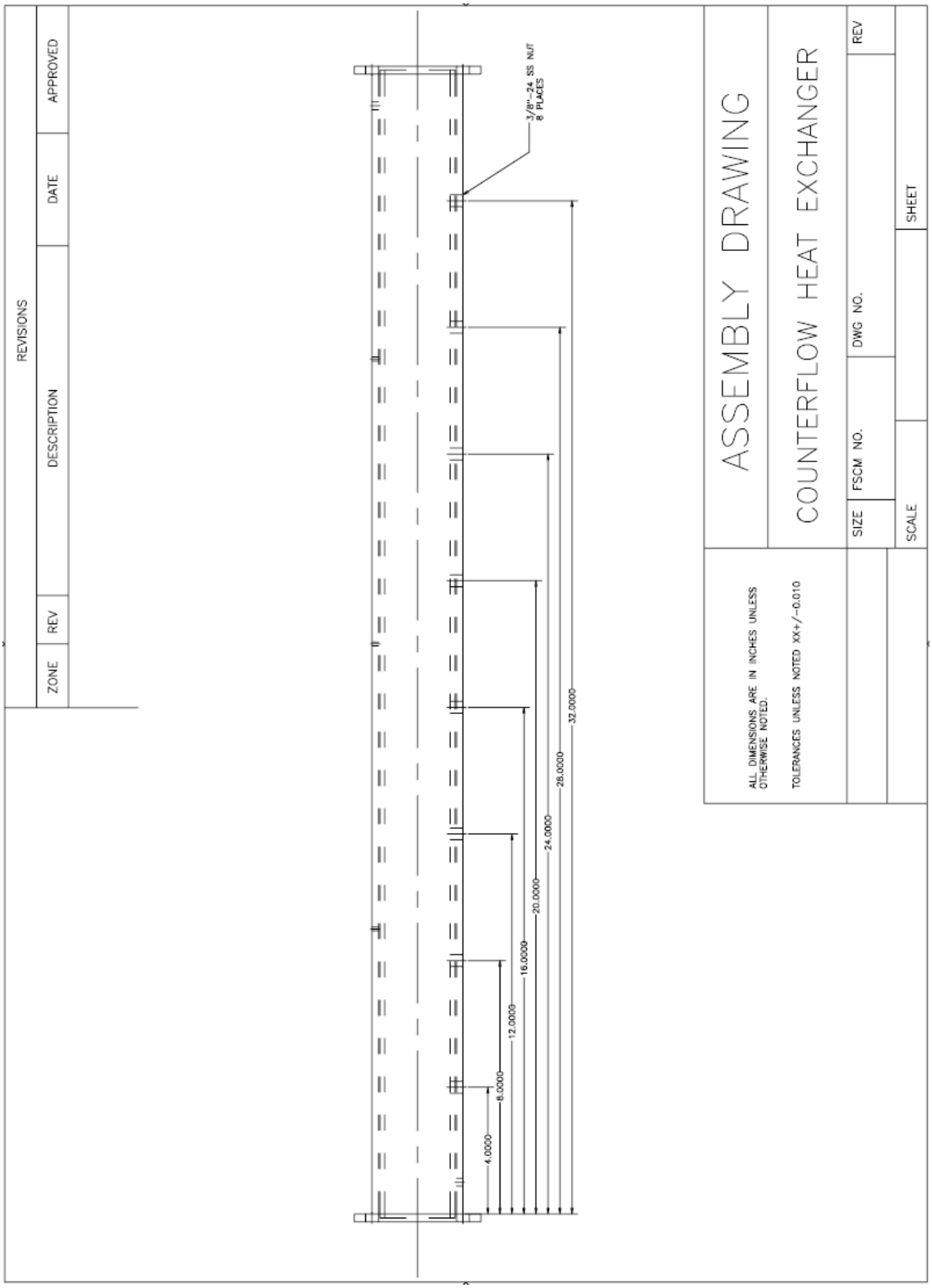

REVISIONS				
ZONE	REV	DESCRIPTION	DATE	APPROVED

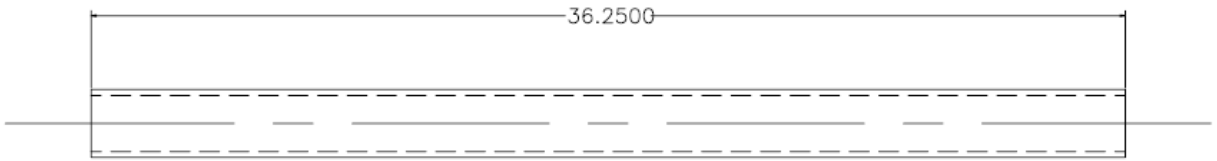

All dimenstions are in inches unless otherwise noted.

Tolerances unless noted XX+/-.010

316 STAINLESS STEEL
2'' SCHEDULE 40 PIPE
COUNTERFLOW HEAT EXCHANGER
INNER TUBE (2 REQ)

SIZE	FSCM NO.	DWG NO.	REV

SCALE		SHEET

REVISIONS				
ZONE	REV	DESCRIPTION	DATE	APPROVED

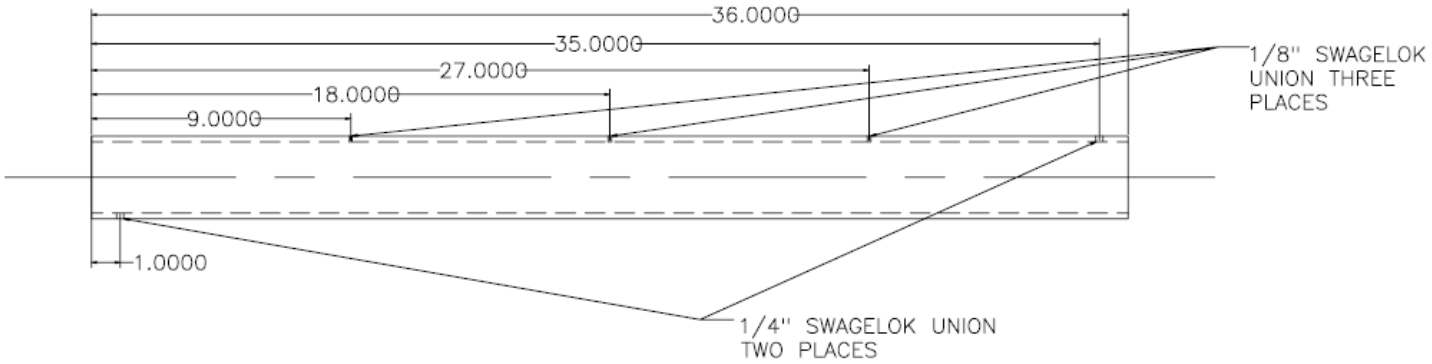

All dimenstions are in inches unless otherwise noted.

Tolerances unless noted XX+/-.010

316 STAINLESS STEEL
2-1/2" SCHEDULE 40 PIPE
COUNTERFLOW HEAT EXCHANGER
OUTER TUBE (2 REQ)

SIZE	FSCM NO.	DWG NO.	REV
SCALE		SHEET	

REVISIONS				
ZONE	REV	DESCRIPTION	DATE	APPROVED

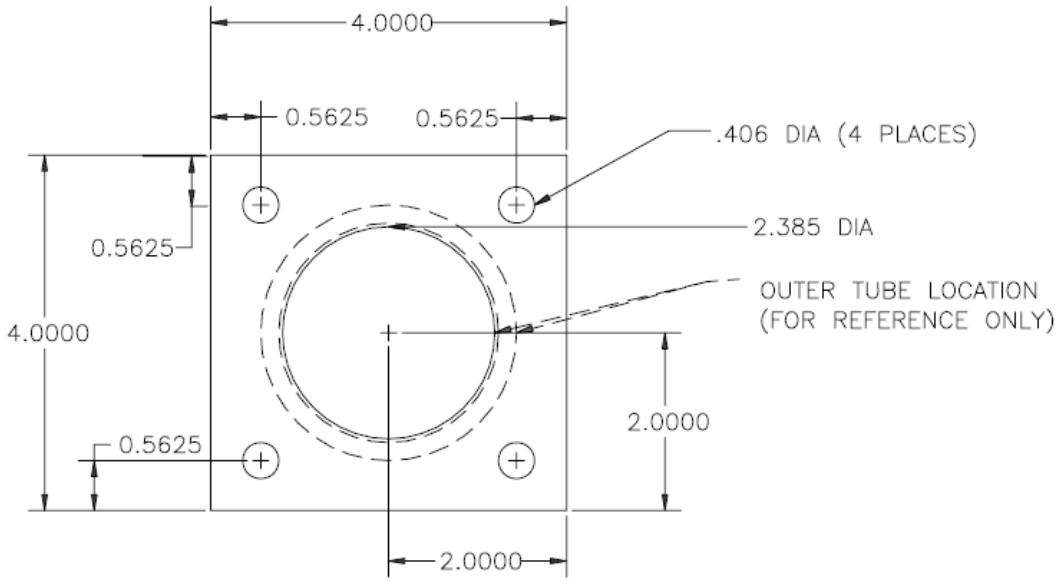

All DIMENSTIONS ARE IN INCHES UNLESS OTHERWISE NOTED.

TOLERANCES UNLESS NOTED XX+/-.010

304 STAINLESS STEEL
1/4" PLATE

COUNTERFLOW HEAT EXCHANGER
ATTACH PLATE (4 REQ)

SIZE	FSCM NO.	DWG NO.	REV
SCALE		SHEET	

REVISIONS				
ZONE	REV	DESCRIPTION	DATE	APPROVED

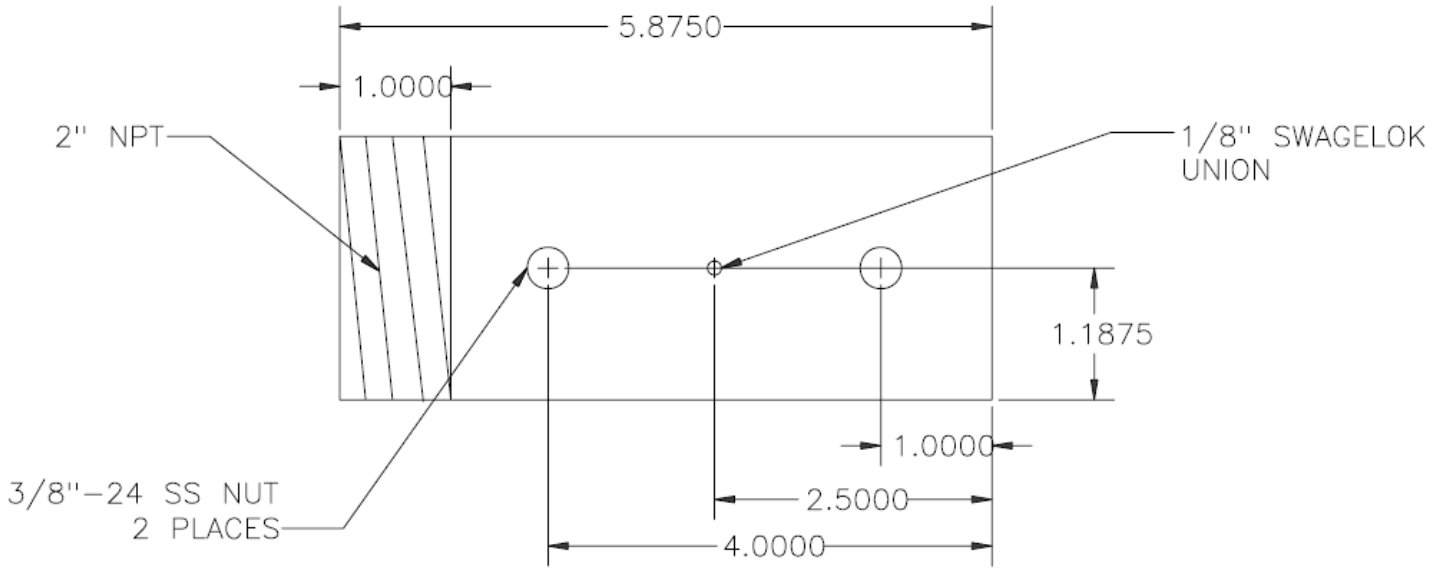

All dimenstions are in inches unless otherwise noted.

Tolerances unless noted XX+/-.010

316 STAINLESS STEEL
2" SCHEDULE 40 PIPE
COUNTERFLOW HEAT EXCHANGER
TUBE EXTENSION (4 REQ)

SIZE	FSCM NO.	DWG NO.	REV
SCALE		SHEET	

Inconel Heat Exchanger

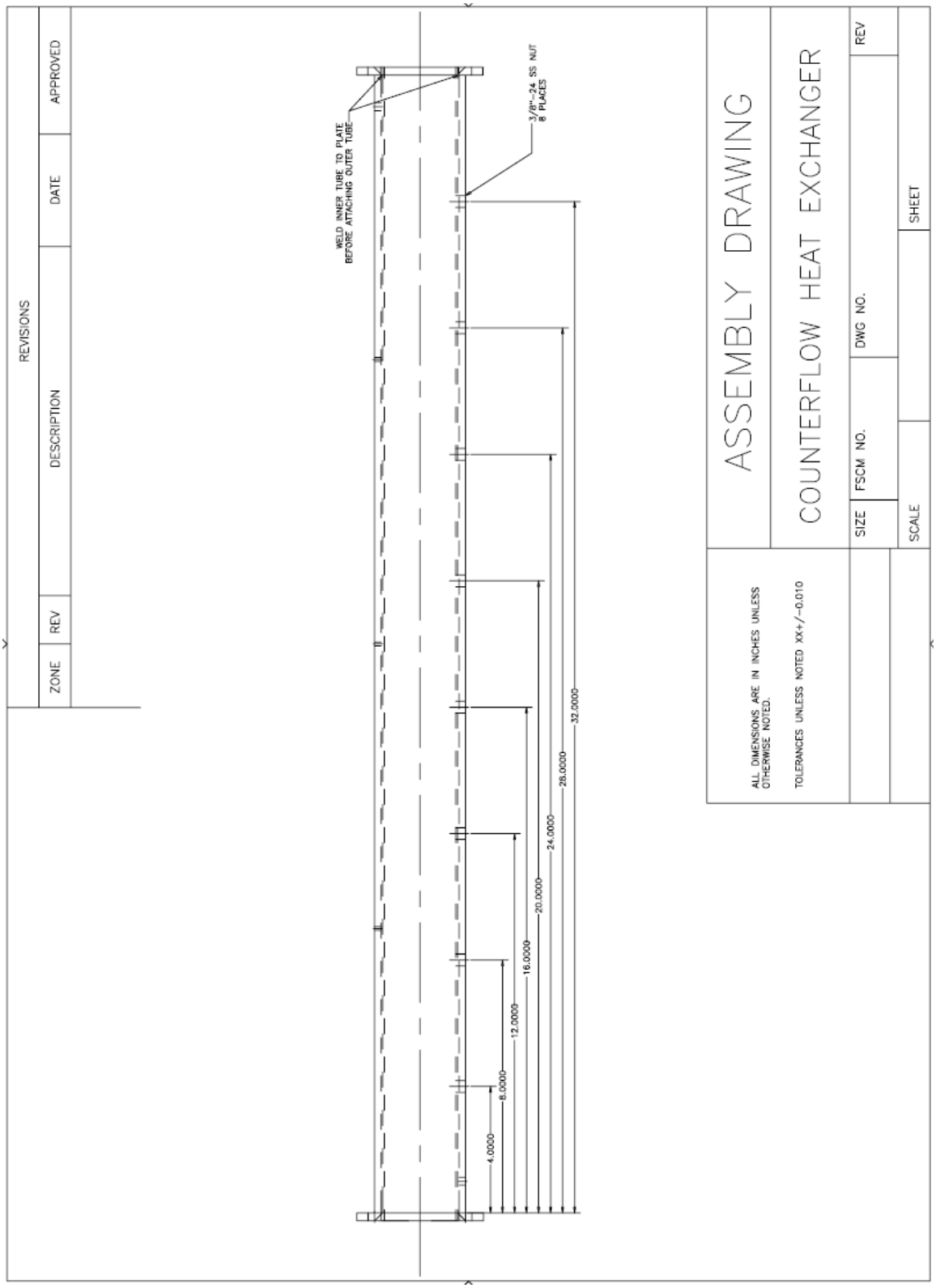

REVISIONS				
ZONE	REV	DESCRIPTION	DATE	APPROVED

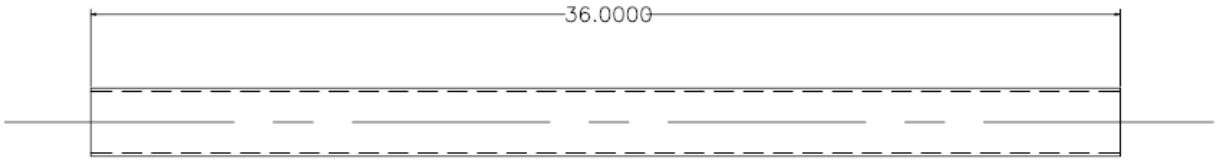

ALL DIMENSTIONS ARE IN INCHES UNLESS OTHERWISE NOTED. TOLERANCES UNLESS NOTED XX+/-.010	INCONEL 625 2" SCHEDULE 10 PIPE COUNTERFLOW HEAT EXCHANGER INNER TUBE (2 REQ)
	SIZE / FSCM NO. / DWG NO. / REV
	SCALE / SHEET

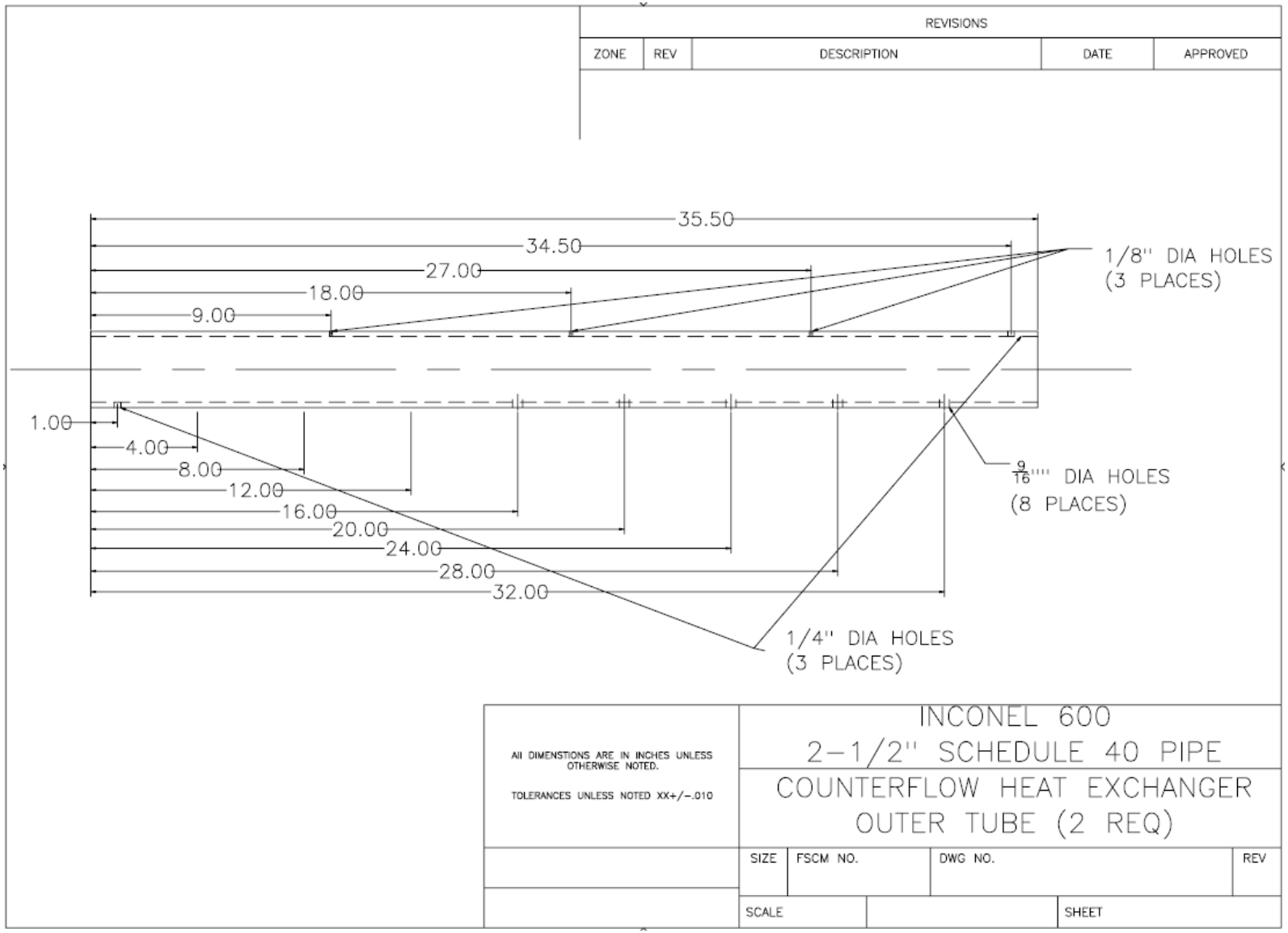
REVISIONS
ZONE
REV
DESCRIPTION
DATE
APPROVED
35.50
34.50
27.00
18.00
9.00
1/8" DIA HOLES
(3 PLACES)
1.00
4.00
8.00
12.00
16.00
20.00
24.00
28.00
32.00
9/16" DIA HOLES
(8 PLACES)
1/4" DIA HOLES
(3 PLACES)
ALL DIMENSTIONS ARE IN INCHES UNLESS OTHERWISE NOTED.
TOLERANCES UNLESS NOTED XX+/-.010
INCONEL 600
2-1/2" SCHEDULE 40 PIPE
COUNTERFLOW HEAT EXCHANGER
OUTER TUBE (2 REQ)
SIZE
FSCM NO.
DWG NO.
REV
SCALE
SHEET

REVISIONS				
ZONE	REV	DESCRIPTION	DATE	APPROVED

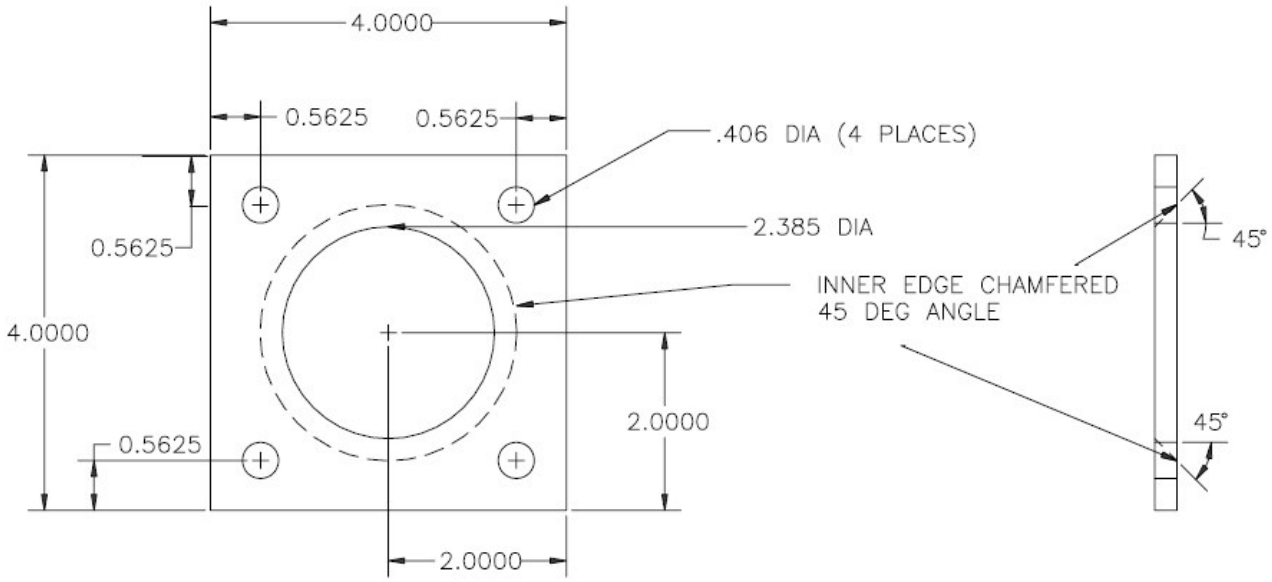

All DIMENSTIONS ARE IN INCHES UNLESS OTHERWISE NOTED. TOLERANCES UNLESS NOTED XX+/-.010	INCONEL 625 1/4" PLATE COUNTERFLOW HEAT EXCHANGER ATTACH PLATE (4 REQ)

SIZE	FSCM NO.	DWG NO.	REV
SCALE		SHEET	

Bibliography

Bartok, William and Sarofim, Adel F. *Fossil Fuel Combustion – A Source Book*. New York City NY: John Wiley and Sons Incorporated, 1991.

Beer, Ferdinand P., Johnston, E. Russell, Jr., and DeWolf, John T. *Mechanics of Materials (4th Edition)*. New York NY: McGraw-Hill Company, 2003.

Coleman, Hugh W. and Steele, W. Glenn, Jr. *Experimentation and Uncertainty Analysis for Engineers*. New York NY: John Wiley and Sons Incorporated, 1989.

Coordinating Research Council (CRC) Incorporated. *Handbook of Aviation Fuel Properties (3rd Edition)*. CRC Report No. 635, 2004.

Edwards, Tim and Maurice, Lourdes, Q. "Surrogate Mixtures to Represent Complex Aviation and Rocket Fuels," *Journal of Propulsion and Power*, Vol. 17: 2, (March – April 2001).

Edwards, Tim. ""Kerosene" Fuels for Aerospace Propulsion – Composition and Properties," *38th AIAA/ASME/SAE/ASEE Joint Propulsion Conference and Exhibit*. Indianapolis IN: AIAA 2002-3874, 7-10 July 2002.

Edwards, Tim. Senior Research Engineer, Air Force Research Laboratory, Propulsion Directorate, Turbine Engine Division, Fuels Branch, WPAFB OH. Personal Correspondence. 1 July 2005 – 1 February 2006.

Eidelman, S., Grossman, W., and Lottati I. "Review of Propulsion Applications and Numerical Simulations of the Pulse Detonation Engine Concept," *Journal of Propulsion and Power*, Vol. 7: 6, (November - December 1991).

Fickett, Wildon and Davis, William C. *Detonation: Theory and Experiment*. New York NY: Dover Publications Incorporated, 1979.

Glassman, Irvin. *Combustion (3rd Edition)*. San Diego CA: Academic Press, 1996.

Hoke, John L., Bradley, Royce P., and Schauer, Frederick R. "Impact of DDT Mechanism, Combustion Wavespeed, Temperature, and Charge Quality on Pulse-Detonation-Engine Performance," *43rd AIAA Aerospace Sciences Meeting*. Reno NV: AIAA 2005-1342, 10-13 January 2005.

Hoke, John L., Bradley, Royce P., Gallia, Jason R., and Schauer, Frederick R. "The Impact of Detonation Initiation Techniques on Thrust in a Pulse Detonation Engine," *44th AIAA Aerospace Sciences Meeting and Exhibit*. Reno NV: AIAA-2006-1023, 9 - 12 January 2006.

Huang, H., Sobel, D., and Spadaccini, L. "Endothermic Heat-Sink of Hydrocarbon Fuels for Scramjet Cooling," *38th AIAA/AMSE/SAE/ASEE Joint Propulsion Conference and Exhibit.* Indianapolis IN: AIAA 2002-3871, 7-10 July 2002.

Huang, He. and Sobel, David R. *Endothermic Heat Sink of Jet Fuels*. AFRL-PR-EP-TR-2002-2094, Air Force Research Laboratory, Propulsion Directorate, Wright-Patterson AFB OH, April 2002.

Incropera, Frank P. and DeWitt, David P. *Fundamentals of Heat and Mass Transfer (5th Edition).* Hoboken NJ: John Wiley and Sons Incorporated, 2002.

Kailasanath, K. "Recent Developments in the Research on Pulse Detonation Engines," *AIAA Journal*. Vol. 41: 2 (February 2003).

Kaneshige, M. and Shepherd, John E. *Detonation database*. Technical Report FM97-8, GALCIT, July 1997.

Katta, V. R., Chin, L.P. and Schauer, F.R. "Numerical Studies on Cellular Detonation Wave Subjected to Sudden Expansion," *Proceedings of the 17th International Colloquium on the Dynamics of Explosions and Reactive Systems*. Heidelberg, Germany, (1999).

Kuo, Kenneth K. *Principles of Combustion (2nd Edition).* Hoboken NJ: John Wiley and Sons Incorporated, 2005.

Lefebvre, A., Freeman, W., and Cowell, L. *Spontaneous Ignition Delay Characteristics of Hydrocarbon Fuel/Air Mixtures*. NASA CR 175064, February 1986.

Metallic Materials Properties Development and Standardization (MMPDS) *MMPDS-01.* USDOT/FAA//AR-MMPDS, 2003. (Replacement for MIL-HDBK-5)

Milton, J. Susan and Arnold, Jesse C. *Introduction to Probability and Statistics: Principles and Applications for Engineering and the Computing Sciences*. New York NY: McGraw-Hill Higher Education, 2003.

Miser, Christen L., King, Paul I., and Schauer, Frederick R. "PDE Flash Vaporization System for Hydrocarbon Fuel Using Thrust Tube Waste Heat," *41st AIAA/ASME/SAE/ASEE Joint Propulsion Conference and Exhibit,* Tucson AZ: AIAA 2005-3511, 10-13 July 2005.

Miser, Christen L., Helfrich, Timothy M., Schauer, Frederick R., and Phelps Donald K. "Supercritical Fuel Density from Experimental Pulse Detonation Engine," *44th AIAA Aerospace Sciences Meeting*. Reno NV: AIAA 2006-1025. 9-12 January 2006.

National Institute of Standards and Technology. *NIST Thermophysical Properties of Hydrocarbon Mixtures Database (SUPERTRAPP) Users Guide* (Version 3.1). February 2003.

Panzenhagen, Kristin L. *Detonation Branching in a PDE with Liquid Hydrocarbon Fuel*. MS thesis, AFIT/GAE/ENY/04-M13. Graduate School of Engineering and Management, Air Force Institute of Technology (AU), Wright-Patterson AFB OH, March, 2004.

Parker, Jason and Schauer, Frederick R. "Data Analysis and Compression Techniques for Megabyte-Data PDE Experiments," *41st AIAA Aerospace Sciences Meeting*. Reno NV: AIAA 2003-0892, January 2003.

PCB Piezotronics. "Introduction to Piezoelectric Pressure Sensors." http://www.pcb.com/tech_pres.html. March 2003.

Popov, Egor P. *Introduction to Mechanics of Solids*. Englewood Cliffs NJ: Prentice-Hall Incorporated, 1968.

Riazi, M. R. *Characterization and Properties of Petroleum Fractions.* Philadelphia PA: ASTM, 2005.

Schauer, Frederick R., Stutrud, Jeffery, and Bradley, Royce P. "Detonation Initiation Studies and Performance Results for Pulse Detonation Engine Applications," *39th AIAA Aerospace Sciences Meeting and Exhibit.* Reno NV: AIAA 2001-129, 8 - 11 January 2001.

Schauer, Frederick R., Miser, Christen L., Tucker, Kelly C., Bradley, Royce P., and Hoke, John L. "Detonation Initiation of Hydrocarbon-Air Mixtures in a Pulse Detonation Engine*," 43rd AIAA Aerospace Sciences Meeting*. Reno NV: AIAA 2005-1343, 10 – 13 January 2005.

Schobert, Harold H., Badger, Mark W., and Santoro, Robert J. *Progress Toward Coal-Based JP-900.* The Energy Institute. The Pennsylvania State University. C211 Coal Utilization Lab, University Park PN, 2002.

Schelkin, K.L. *Soviet Journal of Technical Physics*. Vol. 10: 823-827 (1940).

Shigley, Joseph E. and Mischke, Charles R. *Mechanical Engineering Design.* New York NY: McGraw-Hill Book Company, 1989.

Tucker, K. Colin., King, Paul I., Schauer, Frederick R., and Hoke, John L. "Branched Detonation in a Multi-Tube PDE," *16th International Symposium on Air Breathing Engines*. Cleveland OH: ISABE 2003-1218, September 2003.

Tucker, K. Colin, King, Paul I., Bradley, Royce P., and Schauer, Frederick R. "The Use of a Flash Vaporization System with Liquid Hydrocarbon Fuels in a Pulse Detonation Engine," *42nd AIAA Aerospace Sciences Meeting and Exhibit.* Reno NV: AIAA 2004-0868, 5 - 8 January 2004.

Tucker, K. Colin. *A Flash Vaporization System for Detonation of Hydrocarbon Fuels in a Pulse Detonation Engine*. Air Force Institute of Technology (AU), Wright-Patterson AFB OH. June 2005.

Young, Warren C. *Roark's Formulas for Stress and Strain (6th Edition).* New York NY: McGraw-Hill Incorporated, 1989.

Yu, Jian. and Eser, Semih. "Determination of Critical Properties (T_c, P_c) of Some Jet Fuels*," Ind. Eng. Chem. Res.* Vol. 34: 404-409 (1995).

Zdenek, J. S. and Anthenien, R. A. "Ion Based Pressure Sensor for Pulse Detonation Engines," *42nd AIAA Aerospace Sciences Meeting and Exhibit.* Reno NV: AIAA 2004-470, 5 - 8 January 2004.

Vita

First Lieutenant Timothy Michael Helfrich was born in Indianapolis, Indiana, where he graduated from Warren Central High School. In August 1998, he entered the undergraduate engineering program at Purdue University, where he was awarded a Bachelor of Science in Aeronautical and Astronautical Engineering. Upon graduation in May 2002, he was commissioned through the Detachment 220 AFROTC at Purdue University.

His first assignment was in the Mature and Proven Aircraft Directorate (MAPA) of the Ogden Air Logistics Center at Hill AFB, UT. While assigned to MAPA, Lieutenant Helfrich performed duties as an A-10 Systems Engineer. In September of 2004, he entered the Air Force Institute of Technology Graduate School of Engineering and Management. Upon graduation, he will be assigned to the Propulsion Directorate of the Air Force Research Laboratory until December of 2006, whereupon he will enter the United States Test Pilot School, class 07A.

REPORT DOCUMENTATION PAGE

Form Approved
OMB No. 074-0188

PLEASE DO NOT RETURN YOUR FORM TO THE ABOVE ADDRESS.

1. REPORT DATE *(DD-MM-YYYY)*	**2. REPORT TYPE**	**3. DATES COVERED** *(From – To)*
23-03-2006	Master's Thesis	August 2004 – March 2005

4. TITLE AND SUBTITLE

Cycle Performance of a Pulse Detonation Engine with Supercritical Fuel Injection

5a. CONTRACT NUMBER

5b. GRANT NUMBER

5c. PROGRAM ELEMENT NUMBER

6. AUTHOR(S)

Helfrich Timothy M., First Lieutenant, USAF

5d. PROJECT NUMBER

5e. TASK NUMBER

5f. WORK UNIT NUMBER

7. PERFORMING ORGANIZATION NAMES(S) AND ADDRESS(S)

Air Force Institute of Technology
Graduate School of Engineering and Management (AFIT/EN)
2950 Hobson Way, Building 640
WPAFB OH 45433-7765

8. PERFORMING ORGANIZATION REPORT NUMBER

AFIT/GAE/ENY/06-M14

9. SPONSORING/MONITORING AGENCY NAME(S) AND ADDRESS(ES)

AFRL/PRTC
ATTN: Dr. Frederick R. Schauer
Bldg. 71A, D-Bay, 7th Street
Wright-Patterson AFB, OH 45433 DSN:785-6462

10. SPONSOR/MONITOR'S ACRONYM(S)

11. SPONSOR/MONITOR'S REPORT NUMBER(S)

12. DISTRIBUTION/AVAILABILITY STATEMENT

APPROVED FOR PUBLIC RELEASE; DISTRIBUTION UNLIMITED.

13. SUPPLEMENTARY NOTES

14. ABSTRACT

Pulse detonation engines (PDE) rely on rapid ignition and formation of detonation waves. Because hydrocarbon fuels are composed typically of long carbon chains that must be reduced in the combustion process, it would be beneficial to create such reduction prior to injection of fuel into the engine. This study focused on PDE operation enhancements using dual detonation tube, concentric-counter-flow heat exchangers to elevate the fuel temperature up to supercritical temperatures. Variation of several operating parameters included fuel type (JP-8, JP-7, JP-10, RP-1, JP-900, and S-8), ignition delay, frequency, internal spiral length, and purge fraction. To quantify the performance, four key parameters examined were ignition time, deflagration to detonation transition time, detonation distance, and the percent of ignitions resulting in a detonation. In general, for all fuels except JP-10, increasing the fuel injection temperature decreased deflagration to detonation transition time and detonation distance, increased the percent of ignitions resulting in detonations (detonation percentage), and had no impact on ignition time. JP-10 was difficult to detonate, resulting in extremely poor performance. A minimum spiral length of 0.915 m (36 in) and a minimum purge fraction of 0.3 were determined. An increase in cycle frequency resulted in a decrease in deflagration to detonation transition time, but had little effect on ignition time and detonation distance. Analysis of ignition delay showed that 4 msec is the best ignition delay at high fuel injection temperatures, based on fire phase time and detonation percentage.

15. SUBJECT TERMS

Supercritical, pulse detonation engine, heat exchanger, JP-8, JP8, JP-7, JP7, JP-10, JP10, JP900, JP-900, RP-1, RP1, Fischer-Tropsch, liquid hydrocarbon, endothermic, fuel injection, flash vaporization

16. SECURITY CLASSIFICATION OF:			**17. LIMITATION OF ABSTRACT**	**18. NUMBER OF PAGES**	**19a. NAME OF RESPONSIBLE PERSON**
a. REPORT	**b. ABSTRACT**	**c. THIS PAGE**			Dr. Paul I. King
U	**U**	**U**	**UU**	188	**19b. TELEPHONE NUMBER** *(Include area code)* (937) 255-3636, ext 4628 e-mail: paul.king@afit.edu

Standard Form 298 (Rev. 8-98)
Prescribed by ANSI Std. Z39-18